TOWARDS FLUORESCENCE MICROSCOPY WITH AN STM

by

Philip Grant

B.Sc., Physics, University of British Columbia, 1999

B.Ed., Secondary, University of British Columbia, 2000

THESIS SUBMITTED IN PARTIAL FULFILLMENT

OF THE REQUIREMENTS FOR THE DEGREE OF

MASTER OF SCIENCE

IN THE DEPARTMENT

OF

PHYSICS

SIMON FRASER UNIVERSITY
2007

APPROVAL

Name:	Philip Grant
Degree:	Master of Science
Title of Thesis:	Towards fluorescence microscopy with an STM
Examining Committee:	Dr. David Broun (Chair)
	Dr. John Bechhoefer (Senior Supervisor)
	Dr. Karen Kavanagh (Supervisor)
	Dr. George Kirczenow (Supervisor)
	Dr. Eldon Emberly (Examiner)
Date Approved:	July 26, 2007

SFU SIMON FRASER UNIVERSITY
LIBRARY

Declaration of Partial Copyright Licence

The author, whose copyright is declared on the title page of this work, has granted to Simon Fraser University the right to lend this thesis, project or extended essay to users of the Simon Fraser University Library, and to make partial or single copies only for such users or in response to a request from the library of any other university, or other educational institution, on its own behalf or for one of its users.

The author has further granted permission to Simon Fraser University to keep or make a digital copy for use in its circulating collection (currently available to the public at the "Institutional Repository" link of the SFU Library website <www.lib.sfu.ca> at: <http://ir.lib.sfu.ca/handle/1892/112>) and, without changing the content, to translate the thesis/project or extended essays, if technically possible, to any medium or format for the purpose of preservation of the digital work.

The author has further agreed that permission for multiple copying of this work for scholarly purposes may be granted by either the author or the Dean of Graduate Studies.

It is understood that copying or publication of this work for financial gain shall not be allowed without the author's written permission.

Permission for public performance, or limited permission for private scholarly use, of any multimedia materials forming part of this work, may have been granted by the author. This information may be found on the separately catalogued multimedia material and in the signed Partial Copyright Licence.

While licensing SFU to permit the above uses, the author retains copyright in the thesis, project or extended essays, including the right to change the work for subsequent purposes, including editing and publishing the work in whole or in part, and licensing other parties, as the author may desire.

The original Partial Copyright Licence attesting to these terms, and signed by this author, may be found in the original bound copy of this work, retained in the Simon Fraser University Archive.

Simon Fraser University Library
Burnaby, BC, Canada

Revised: Summer 2007

Abstract

Fluorescence spectroscopy has advanced our understanding of biological processes and structures through the development of probes that may be attached to specific points of interest. Though a powerful tool, fluorescence spectroscopy has always been limited by resolution. In an attempt to increase resolution, we have built a scanning tunneling microscope that can capture light emitted while scanning, and we tested our apparatus by examining light emission from surface plasmons excited by tunneling electrons from the STM tip. We then used our STM to observe DNA attached to a gold substrate and found that DNA quenches plasmon emission. We also found that both non-labeled and fluorescent-labeled DNA have light emission images that change when repeatedly scanned. We argue that these changes are due to DNA damage by low energy (≤ 3 eV) tunneling electrons.

Keywords: STM; DNA; fluorescence; low-energy-electron damage.

I dedicate this work to God,
who is a continuous source of strength for me.

Acknowledgments

I would like to thank my supervisor Dr. John Bechhoefer for his help and guidance throughout this entire process. His broad knowledge of physics, math, and writing has helped me go from a theoretical idea to experiment and finally to communicating the results. I would also like to thank my supervisory committee members, Dr. George Kirczenow and Dr. Karen Kavanagh for their assistance in my research and their guidance through this project. A special thanks to Dr. Patricia Mooney for allowing me to use her AFM and to Dr. Gary Leach for allowing me to use his spectrometer.

During my time working in our lab, I met several people that I would like to thank for their help. I want to thank Dr. Peter Williams, Dr. Yuekan Jiao and Dr. Connie Roth for many useful conversations and instructions on using various equipment. I want to thank Shun Lu for his help in creating our initial gold samples and Otto Verhage for working with me to characterize the STM's light collection. I also want to thank Dr. Suzana Glavas for her help in fluorescence microscopy and Dr. Hogan Yu for his help in our initial sample preparation. Also, thanks to all the SFU physics community for making this an enjoyable time.

To my friends and family, thank you for the support you gave me during this project, it helped keep me upbeat even in the tough times. Finally, I would like to thank my wife, Tina, for her love and support throughout my work.

Contents

List of Figures

Chapter 1

Introduction

Fluorescence spectroscopy has led to great discoveries in science over the past few decades by advancing our understanding of biological processes and structures [1–7]. Though fluorescence spectroscopy is a powerful tool, it has always been limited by resolution. Resolution for a conventional fluorescence microscope is limited by the light used to excite the fluorophores. This light is subject to diffraction, giving a minimum distance, $x_{min} \approx 200$ nm at which two fluorophores could be resolved using an oil objective. Unfortunately, this is far larger than many biological molecules of interest. For example, double-stranded DNA (dsDNA) is only 2 nm wide and extends 3.4 nm per 10 base pair sequence.

To further increase our understanding, we need to find techniques to overcome this resolution limit. Some techniques such as stimulated emission depletion (STED) microscopy have improved on the limit using far-field techniques but are still limited to a resolution of 40 nm [8]. Other techniques such as scanning near-field optical microscopy (SNOM) have used near-field optics, where diffraction limitations do not apply, to achieve a resolution of 10 nm [9]. Even these scales are too large to resolve many biological molecules of interest.

Because of the localization (to ≈ 1 nm) of its tunneling current, the scanning tunneling microscope (STM) can, in principle, produce the needed resolution by exciting a fluorophore and capturing the emitted light as it scans over a surface. In this project, we make progress towards the goal of using an STM to scan fluorescent marked biological specimen, resolving sub-nanometer structure and discover some difficulties in using tunneling electrons to probe DNA.

In this thesis, I begin with a chapter to review the relevant theory that led us to try this experiment. In the third chapter, I go over the set up of our scanning tunneling microscope and how it can make the measurements necessary to test our hypothesis, including measurements to characterize the equipment. In the fourth chapter, I go over our procedures for sample preparation and how we optimized our samples for our measurements. In the fifth chapter, I go over the results of our experiment, including a section on testing our light-emission collection, imaging DNA topographically and via light emission, and studying the changes to DNA caused by a scanning tunneling microscope. In the sixth chapter, I discuss different theories that can explain the results and go over how they relate to our findings. In the seventh chapter, I conclude by reviewing the major findings and look to future work in this area.

Chapter 2

Background

In this chapter, I discuss some relevant background related to our project. I begin with a brief review of microscopy techniques for imaging, discussing the advantages and limitations of those techniques. I then describe the scanning tunneling microscopy technique we are pursuing. Finally, I discuss some of the various complications that must be overcome during our project.

2.1 Fluorescence microscopy

Fluorescence microscopy is a widely used tool to identify and study molecules of interest, but conventional implementations are limited in resolution to spatial scales at or exceeding the wavelength of light. Over the last few years, there have been many approaches taken to increase the resolution of imaged specimens. In this section, I first discuss fluorescence microscopy and its resolution limitations. Then, I review more recent techniques used to enhance resolution.

2.1.1 Fluorescence spectroscopy

In fluorescence processes, energy is rapidly released in the form of light from an electronically excited state [10]. This process has been widely adopted to study biological specimens using fluorescent probes created to localize in a specimen and emit light when excited by photons having a specific range of energies.

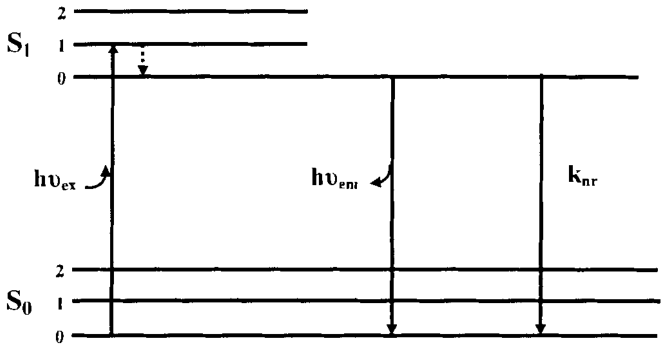

Figure 2.1: Simplified Jabłoński diagram showing an excitation from the ground state to the second vibrational level of the first singlet state. Internal conversion is represented by the dashed arrow that represents processes that bring the molecule into the lowest vibrational level of the first singlet state. Then the molecule can return to the ground state by two different paths. Either it emits a photon of light, $h\nu_{em}$, or it follows a nonradiative path, k_{nr}.

A fluorescent probe, or fluorophore, is a molecule able to emit light when excited. A fluorophore can exist in many different electronic states depending on its internal energy. These include the ground state, which a fluorophore is most commonly found in at room temperature, and the first and the second electronic states. The Jabłoński diagram of Fig. 2.1 shows two of the states and their vibrational energy levels. When energy is absorbed by a fluorophore, it is excited into one of the vibrational levels of a higher energy state. Within a short period of time ($\approx 10^{-12}$ s), the fluorophore relaxes into the lowest vibrational level of the first electronic state by conformational changes and reactions with its environment. This relaxation process can quench the emission if the reactions with the environment dissipate enough energy to return the fluorophore to its ground state by a nonradiative path, k_{nr}. If the excitation has not been quenched, the fluorophore will return to the ground state after (typically) several nanoseconds by the release of energy as an emitted photon, $h\nu_{em}$. It is this photon that is detected and used in fluorescence spectroscopy.

The properties of different fluorophores can be used to probe different processes in a system. For example, probes that attach to specific molecules of interest in a biological specimen allow one to monitor position, orientation, concentration and other details of the molecule. In this way, fluorescence spectroscopy has allowed scientists to better understand many microscopic processes.

2.1.2 Resolution limit

Although fluorescence microscopy is a widely used tool for understanding biological specimens, it has limitations that prevent its use in some areas of research. The most significant limitation is the resolution of the microscope used to detect the emitted photon.

A fluorescence microscope is equipped with lens that have a limited numerical aperture, $NA = n \sin\theta$, with n the index of refraction of the medium between the specimen and lens and θ the half angle of the cone of light captured by the lens. A specimen being imaged scatters light by diffraction. The many orders of diffraction leave the specimen at angles ϕ_m, given by

$$\sin\phi_m = \frac{m\lambda}{x}, \tag{2.1}$$

with m the order of diffraction, λ the wavelength of light and x the distance between two features being resolved. For a fluorescence microscope, it is possible to capture the diffracted light only if the NA of the lens being used is greater than $\sin\phi_m$. Since no lens can capture all the diffracted light, some of the diffraction orders must be lost, leading to a limited lateral resolution given by [11]

$$x_{min} = \frac{0.61\lambda}{NA}, \tag{2.2}$$

where x_{min} is the minimum distance between two objects that can be resolved. With $\lambda =$ 400 nm and $NA = 1.4$, Eq. 2.2 gives a "best case" lateral resolution for a far-field optical microscope of 174 nm. Under more typical observational conditions, it is $\approx$ 250 nm.

The axial resolution is slightly worse and is given by [11]

$$z_{min} = \frac{2\lambda\eta}{(NA)^2}, \tag{2.3}$$

with η the refractive index of the object medium and z_{min} corresponds to the distance that the objective must be raised to find the first intensity minimum of the axial diffraction pattern. Typical values for axial resolution are $\approx$ 700 nm

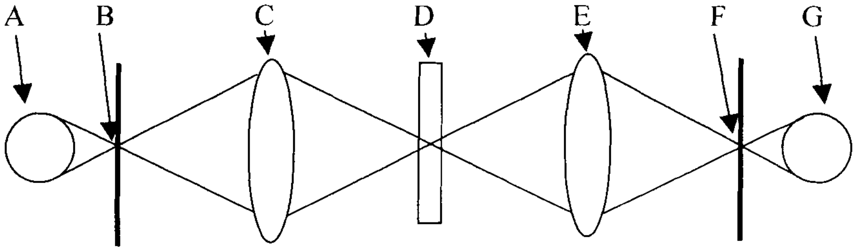

Figure 2.2: Setup for a confocal system, in transmission mode. Light source (A) is limited by the first pinhole (B). The Condenser lens (C) focuses the pinhole illumination on the specimen (D). The objective lens (E) focuses the sample image onto the second pinhole (F) which limits the light hitting the detection equipment to that from the focused spot in the specimen [11].

The resolution of conventional microscopy is good for viewing many cell structures, but many interesting processes in cell biology take place at scales of 50 nm or less. Because of this, there is a need for techniques that can improve on the resolution limits stated above. There have been three different approaches to overcoming the resolution limit to date. First, using far-field microscopes, there have been several techniques based on nonlinear processes. Second, using statistical analysis, there has been progress towards image processing to reduce the limit. Third, using near-field optical processes, there has been progress towards limiting the resolution to the size of the probe instead of wavelength.

2.1.3 Far-field resolution improvements

There have been improvements to the resolution of fluorescence microscopes using special techniques that employ nonlinear processes. These techniques involve improving the lateral or axial resolution of an image. Most of these improvements use a confocal microscopy system, which I introduce below. Then, I discuss some of the techniques and their contributions, beginning with axial improvements and ending with lateral improvements.

Confocal microscopy involves using a pinhole to regulate the light that hits the specimen and a second pinhole to regulate the observed light. In simple confocal setups, the optics, including the pinholes, is kept fixed, while the sample is scanned to form an image. Commercial confocal microscopes generally scan the focused beam while keeping the sample fixed. Although more complicated, the optical scanning method is faster. In the simple-scanning setup (Fig 2.2), the light used for illumination is restricted by a pinhole placed in front of it, and a condenser lens focuses an image of the illuminated pinhole to a spot on the specimen for illumination. The field of view is limited in the same way by a second pinhole between the objective lens and the light-detection device. By doing this, only the light from the illuminated spot focused by the objective lens (identical to the condenser lens) onto the second pinhole is observed. With this setup, one should theoretically have twice the resolution and light that is not from the focal point being observed is rejected by the optics helping to reduce blurring and improving the signal-to-noise ratio. In many setups, dichroic mirrors are used to simplify the optics, so that only one high-NA objective and one pinhole are needed.

Multiphoton (MP) microscopy uses the simultaneous absorption of more then one photon to excite a fluorophore and produce emission. One does this by using a laser with a fraction of the wavelength necessary to excite a fluorophore and focusing the laser on a point that is to be imaged. It is necessary to have a high intensity of light for multiphoton excitation and this ensures that fluorophore excitation and emission is produced only from the focal point of the laser. Because excitation depends on more than one event, the probability for a fluorescent molecule to be in the excited state is proportional to the n^{th} power of the incident intensity ($P \propto I^n$), with n the number of photon absorptions per emission. This also means that the emitted light intensity is proportional to I^n. R Heintzmann *et al.* showed that the highest exponent present in a polynomial expansion of the nonlinear dependence between excitation and emission defines the resolution, increasing the theoretical resolution by a factor of n [12]. However, the expected factor of n increase in resolution is mostly lost by using longer wavelength light, giving an average axial resolution of ≈ 400 nm [13]. Three other advantages of MP microscopy are removing out-of-focus background in the axial plane, reducing out-of-focus photobleaching by only exciting fluorescence at the focal point, and increasing the penetration depth by using long wavelength excitation light. Disadvantages of the method include heating of the sample by high intensity near-IR light and photodamage caused by the high intensity of light at the focal point. Still, the photodamage is often less than that produced by regular confocal microscopy because of the limited focal volume.

Total-internal-reflection (TIRF) microscopy uses evanescent light, created when the excitation light is incident on the specimen at angles greater then the critical angle, to excite fluorophores. Using evanescent light prevents light from entering the bulk of the specimen and restricts excitation of fluorophores in an aqueous or cellular environment to a few hundred nanometers from the sample interface. The limited excitation region is caused by the exponential decay of the evanescent intensity, $I = I_0^{-z/z_0}$, with $z_0 \approx \frac{\lambda}{4\pi}$ [14], which leads to a penetration depth dependent on the wavelength of light used, λ. Although this limits TIRF microscopy to imaging fluorophores that are close to and often attached to the sample interface, it also removes much of the background signal created by exciting fluorescence outside of the image plane. TIRF microscopy also increases axial resolution based on the exponential decay of the light intensity because fluorophores are excited in a region smaller than the diffraction limited resolution. This gives an axial resolution of $\approx$ 100 nm. This makes the limited axial imaging length both an advantage and a disadvantage. Other disadvantages of this technique include the need for very high NA (> 1.4) lenses, special coverslips and the use of volatile, high-refractive-index immersion oil that leaves a crystalline residue, which are all expensive.

Another approach, 4-Pi microscopy, involves using two opposing lenses to excite and image a sample. In doing this, the two opposing spherical wavefronts constructively interfere leading to a narrowed main focal maximum in the axial direction. This narrowing can produce up to a 7-fold increase in axial resolution, for resolution of around 100 nm [15], with little or no decrease in lateral resolution when used in a confocal system. Some disadvantages of this system include the need to align two high-NA objectives and to index match the specimen (e.g., glycerin solutions for oil-immersion objectives) which has been a barrier to imaging live cells with oil-immersion objectives. Using two water-immersion objectives for 4-Pi microscopy, Bahlmann *et al.* imaged live cells with axial resolution approximately four times better than regular confocal resolution [16].

Perhaps the most promising non-linear technique is stimulated emission depletion (STED), a technique that increases the lateral resolution limit. STED involves exciting fluorophores with a laser pulse and then depleting the excited fluorophores using another red-shifted pulse superimposed over the first. The photon detector is gated to not count (ignore) these first photons. The resolution is increased because the depletion pulse is produced with a dark spot at the centre, forming a ring of light. After the depletion pulse, emission is observable only from a small region at the centre of the dark spot because the rest of the excited fluorophores are quenched. This changes the theoretical lateral resolution from Eq. 2.2 to [17]

$$x_{min} = \frac{0.45\lambda}{NA\sqrt{1+I/I_{sat}}}, \tag{2.4}$$

with I_{sat} the light intensity necessary to transition half the population of fluorophores into an excited state and I the light intensity of the beam used. The small emitting region is then scanned over the sample, creating subdiffraction lateral resolution of 40 nm [8] and possibly lower in the future. This technique has the advantage of being a far-field technique that only needs a confocal setup. Some disadvantages include the need for expensive and sophisticated laser sources to produce femtosecond pulses separated by picoseconds and fast gated-detector electronics.

2.1.4 Statistical resolution improvements

Using statistics on the collected light from fluorophores can also lead to improved resolutions. These statistical methods depend on the amount of light that one can collect from a fluorophore before photobleaching.

For localizing a single fluorophore, Thompson *et al.* [18] showed that the centre of the fluorophore can be located with increasing accuracy depending on the amount of photons detected from the fluorophore. By fitting a fluorophore light distribution with a gaussian distribution, they could locate the centre of the fluorophore with uncertainty [18]

$$\sigma_i = \sqrt{\frac{s_i^2}{N} + \frac{a^2/12}{N} + \frac{8\pi s_i^3 b^2}{a^2 N^2}}, \tag{2.5}$$

with s_i the standard deviation of the collected photons in direction i (x or y), a the pixel size of the detector, b the standard deviation of the background, and N the number of photons emitted from the fluorophore. The first term in Eq. 2.5 is the photon noise, the second term is the effect of finite detector pixels and the third term is the effect of background counts b. For high photon numbers, Eq. 2.5 can be approximated by $\sigma_i \sim \sigma_0 1/\sqrt{N}$, with $\sigma_0 \sim \lambda/NA$ the standard resolution, while for low photon numbers, the background dominates. Since one collects typically ≈ 10000 photons from a single fluorophore before it bleaches, one expects $\sigma \sim \lambda/\sqrt{N} \sim 1.5$ nm. Experimentally, Thompson et al. fit a gaussian distribution to the measured photons of a single fluorophore and extracted a centre position that had an uncertainty of $\sigma \approx 4$ nm [18]. Also using this method, Yildiz *et al.* [19] were able to locate the centre of an immobile CY3 dye with 1.24 nm uncertainty by collecting 14, 200 photons per dye molecule.

The above method fails when more than one fluorophore is within the point-spread function of the optics. Strategies that have been tried in such cases include looking for sequential photobleaching [20] and fitting to superpositions of gaussians [21]. In another strategy similar to the photobleaching method, one can use fluorophores capable of being switched from an emitting state to a non-emitting state to separate fluorophores and allow one to fit each with a gaussian [22]. By combining the ideas of photobleaching and switching fluorophores on and off, Sharonov *et al.* used fluorophores that only emit when attached to a molecule of interest and either unattach or photobleach over time, giving the observer a spike of emission with each attaching event [23]. By collecting several emission spikes, they were able to reconstruct the position of the molecules of interest. This technique allows one to control the number of photons captured by replenishing the non-bleached dye concentration and continuing to capture photons, but it is limited by the necessity for a stationary molecule of interest.

2.1.5 Near-field resolution improvements

In Sec. 2.1.1, we noted that the fundamental limit to resolution arose because high-orders of diffraction lead to evanescent waves that are ordinarily not captured. Scanning near-field optical microscopy (SNOM) is a technique that uses these highly localized evanescent waves to excite fluorophores by scanning an optical excited probe of subwavelength size over a sample. The resolution is then mainly limited by the probe size. In this section, I discuss this technique and the resolution possible with it.

The most common method of imaging using near-field techniques is to excite fluorophores using an optical probe with an aperture smaller than a wavelength of light, $d \ll \lambda$, and very close to the sample, $d \approx l$, with l the separation distance between the sample and aperture. In this setup, the spot size of the light used to excite fluorophores is limited by the aperture size. To image a sample, one scans the small excitation spot over the surface with light collected from a fluorophore corresponding to the tip position. Often this is done using a sharpened optical fibre, with its sides coated in metal, held close to the surface in the same way as an atomic force microscope. A further gain in resolution has been reported with a sharp metal tip positioned over the aperture, called tip on aperture (TOA) [9]. With TOA, the light from the aperture is used to excite surface plasmons on the metallic tip. These surface plasmons travel down the tip to the apex and are reflected back, creating standing waves. Theoretically, the plasmons are thought to concentrate at the apex of the tip to produce strong electromagnetic fields to excite fluorophores. This limits the fluorophore emissions to approximately the size of the tip apex and has been used to resolve details as small as 10nm [9].

Another increase in resolution has been produced using an apertureless probe to locally excite fluorophores. This method is similar to the TOA method in that a tip excited by light is used to excite fluorophores as it scans over a surface; the difference being that the light used to excite the tip is coming from a far-field laser focused on the tip location. One problem with apertureless SNOM is the production of fluorescence from both the far-field laser used to excite the tip and the near-field excited tip. By using a tapping mode AFM for the excited tip and separating the two signals with a phase filter referenced to the vibrations of the tapping-mode AFM, Ma *et al.* have used this technique to achieve a lateral resolution of 8.2 nm [24].

Although SNOM techniques produce great resolution, it is limited to imaging specimens that are located on a surface and very close to the imaging tip. By being limited to surfaces, only certain samples can be imaged. Also, since the tip is close to the excited specimen, the tip interacts with the local electromagnetic field and changes the emission, making interpretation of the images challenging [13].

2.2 Fluorescence excitation using an STM

Better resolution techniques are still necessary for imaging many biological molecules of interest. We are attempting to produce this resolution using an STM tip scanning the surface with electrons to locally excite emission from a fluorophore. With this technique, it would be possible to probe fluorescent specimen with sub-nanometer resolution. In this section, I discuss the background that leads us to believe that an STM is capable of doing this.

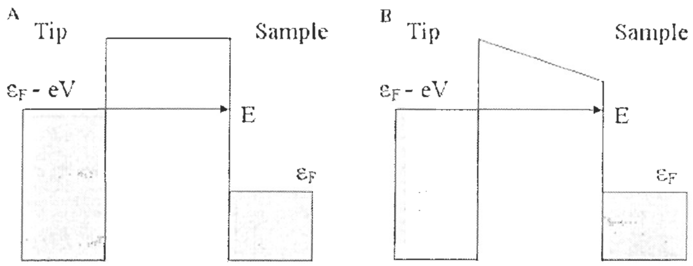

Figure 2.3: Tunneling barrier for a metal-insulator-metal system. (A) Model used for the calculations in the theory section. (B) More realistic model for an STM, showing the effect of an applied bias voltage on the tunneling barrier.

2.2.1 STM resolution

A scanning tunneling microscope (STM) has sub-nanometer resolution due to the tunneling process it uses. This makes it a good candidate for furthering the resolution of fluorescent microscopy if, when scanning a surface, tunneling electrons could excite fluorophore emission and the light collected be used to create an image corresponding to the tip position. By applying the basic principles of quantum mechanics to electron tunneling, I estimate the effect a change in tunneling distance has on the current from a scanning tunneling microscope (STM). I then use this result to give insight into the resolution of an STM.

Applying quantum mechanics to a metal-insulator-metal system gives the probability for an electron to be found in the insulator, a classically forbidden region. This tunneling between two separated conductors is the basis for scanning tunneling microscopy. In Fig. 2.3b, we see a model of an STM system, comprised of a vacuum between a negatively biased tip and a conducting sample. To simplify the calculation of tunneling current, I ignore the bias voltage and work with tunneling between a tip and substrate of the same material, represented by a rectangular barrier (Fig. 2.3a). A rectangular potential barrier of height, V_o, and width, a, gives us a potential-energy topography of

$$V_x = \begin{cases} 0 & \text{for } x > 0, \\ V_o & \text{for } 0 < x < a, \\ 0 & \text{for } x > a. \end{cases} \tag{2.6}$$

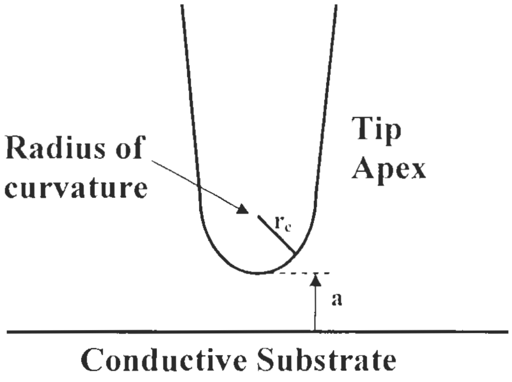

Figure 2.4: Diagram of an STM tip, used to model the resolution, with a tunneling distance, a, and radius of curvature, r_c.

with V_o greater than zero. If we use the time-independent Schröedinger equation

$$\frac{-\hbar}{2m}\frac{d^2\Psi}{dx^2} + V\Psi = E\Psi, \tag{2.7}$$

with a tunneling electron, $0 < E < V_o$, we end up with three different general solutions for the three different regions:

$$\Psi = \begin{cases} Ae^{ikx} + Be^{-ikx} & \text{for } x > 0, \\ Ce^{ik_bx} + De^{-ik_bx} & \text{for } 0 < x < a, \\ Fe^{ikx} & \text{for } x > a \end{cases} \tag{2.8}$$

For these solutions, the important parameters are

$$k^2 = \frac{2mE}{\hbar^2} \tag{2.9}$$

$$k_b^2 = \frac{2m(E - V_0)}{\hbar^2}, \tag{2.10}$$

which represent the different energies for each area of the barrier potential. These general solutions represent waves traveling in the different directions for each area, except the last area, where it is assumed that no electrons are traveling back toward the barrier.

The continuity equation, at both sides of the potential barrier, for Ψ and its first derivative gives four equations. Using these four equations, one can calculate the transmission coefficient for the tunneling process:

$$T = \left|\frac{F}{A}\right|^2 = \left[1 + \frac{V_o^2 \sinh^2(k_b a)}{4E(V_o - E)}\right]^{-1}. \tag{2.11}$$

For a tunneling electron, where the de Broglie wavelength is much smaller than the vacuum barrier, a, we can approximate the transmission using $ka \gg 1$. In this approximation, the transmission becomes

$$T \approx \frac{16E(V_o - E)}{V_o^2} e^{-2k_b a}. \tag{2.12}$$

showing that the flow of electrons decays exponentially with the distance, a, between the tip and the conducting sample. This allows for extremely sensitive topographical measurements because an axial decrease in tip-sample separation of one angstrom would produce an increase in current close to an order of magnitude. The vertical resolution is then much less than 0.1 nm.

The axial resolution of an STM is based on the above result, Eq. 2.12, and the shape of the tip used for tunneling. The tip apex has a finite radius of curvature, r_c, as seen in Fig. 2.4. The curvature produces an increase in tip-sample separation, $a = x^2/2r_c$, a distance x from the apex. This increase in tip-sample separation limits the tunneling current to a small region at the apex because of Eq. 2.12, which leads to a change in current

$$I(\Delta x) = I_o e^{-k\frac{x^2}{r_c}}, \tag{2.13}$$

with I_o the current at the spot of closest approach, x a change in distance laterally away from the tip apex, and r_c the radius of curvature. One concludes that the resolution of 0.2 nm needed to resolve atoms is produced by small protrusions from the tip, making an effective diameter for the tip of ≤ 1 nm [25].

2.2.2 Fluorophore excitation by inelastic tunneling

Our technique to improve fluorescence microscopy resolution involves using the localized STM tunneling current to excite fluorophores. As explained above, the lateral resolution of STM images is often found to be ≤ 1 nm. Using this resolution to locally excite fluorophores would allow one to image many biological processes that have thus far been

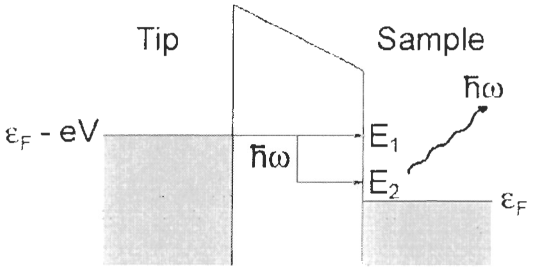

Figure 2.5: Inelastic tunneling through a tunneling barrier.

unresolvable. We hypothesize that an STM can be used to excite fluorophores through inelastic tunneling. In this section, I discuss inelastic tunneling and a model produced by V. Fourmond [26] to estimate the probability of exciting a fluorophore by inelastic tunneling.

In inelastic tunneling, part of an electron's energy is lost while tunneling, a result of interactions with the environment in the tunneling gap. This interaction occurs because of electric fields found in the tunneling gap and leads to a transfer of energy from the tunneling electron to other atoms. Tunneling electrons use this interaction as another path for tunneling, resulting in an increased conductivity for a sample and an excitation of the electromagnetic field they couple to. If tunneling electrons have enough energy, inelastic tunneling can lead to photon emission as an STM tip passes over a fluorophore (Fig. 2.5). With the excitation of a fluorophore limited to the dimensions of the tunneling current beam, one could measure very precisely fluorophore location by collecting the emission as a function of tip position.

Following the report by V. Fourmond [26], we can approximate a fluorophore in the tunneling gap of an STM as a two-state dipole in that gap with a zero'th-order Hamiltonian $\hat{H}_0$,

$$\hat{H}_0 = \begin{pmatrix} 0 & 0 \\ 0 & E_0 \end{pmatrix}. \tag{2.14}$$

where $E_0 = \hbar\omega_0$ the transition energy. This gives a Schröedinger equation for the dipole of

$$i\hbar\frac{\partial\left|\psi\right\rangle}{\partial t} = \hat{H}_0\left|\psi\right\rangle + \vec{E}(t)\cdot\vec{D}\left|\psi\right\rangle, \tag{2.15}$$

with $\vec{D}$ the dipole operator.

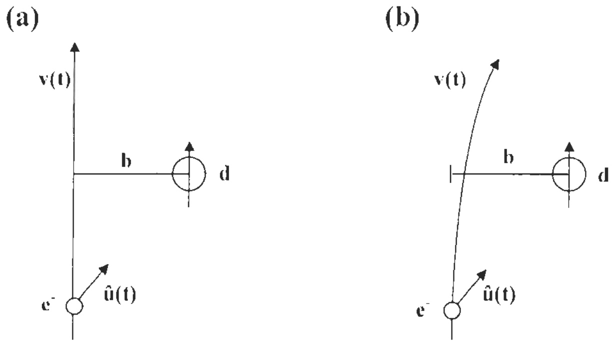

Figure 2.6: Model of an tunneling electron exciting a fluorophore. (a) First model, electron travels in a straight path by the dipole. (b) Second model, including the dipole's effect on the electron.

An electron tunneling from the tip to the substrate can couple to the dipole moment of the fluorophore and excite the molecule. V. Fourmond first modeled the system by assuming the electron travels in a straight path by the dipole (Fig. 2.6 (a)). This moving electron would produce a changing electric field at the dipole of

$$\vec{E}(t) = -\frac{e}{4\pi\epsilon_0}\frac{\hat{u}_e(t)}{b^2 + v_e^2 t^2}, \tag{2.16}$$

with $\hat{u}_e(t)$ the unit vector pointing from the electron to the dipole, b the impact parameter, and v_e the speed of the electron.

The tunneling electrons electric field leads to a wave equation for the dipole of [26]

$$|\psi(t)\rangle = c_0(t)\,|\psi_0\rangle + c_1(t)e^{-i\omega_0 t}\,|\psi_1\rangle, \tag{2.17}$$

where

$$\dot{c}_0 = \vec{E}\cdot\vec{d}_{00}c_0 + \vec{E}\cdot\vec{d}_{01}e^{i\omega_0 t}c_1 \tag{2.18}$$

$$\dot{c}_1 = \vec{E}\cdot\vec{d}_{10}e^{-i\omega_0 t}c_0 + \vec{E}\cdot\vec{d}_{11}c_1, \tag{2.19}$$

and $\vec{d}_{ij}$ is the dipole matrix element between state i and j and $\omega_0 = E_t/h$, with E_t the transition energy for the dipole.

First-order perturbation theory, with $c_0 = 1$ and $c_1 = 0$ at $t = -\infty$ and $c_1(t) \ll 1$, leads to the probability of the dipole making a transition from state 0 to 1 [26],

$$P_{trans} = |c_1(t=\infty)|^2 = \left|\int_{-\infty}^{+\infty} \mathrm{d}t\vec{E}(t)\cdot\vec{d}_{10}e^{i\omega_0 t}\right|^2. \tag{2.20}$$

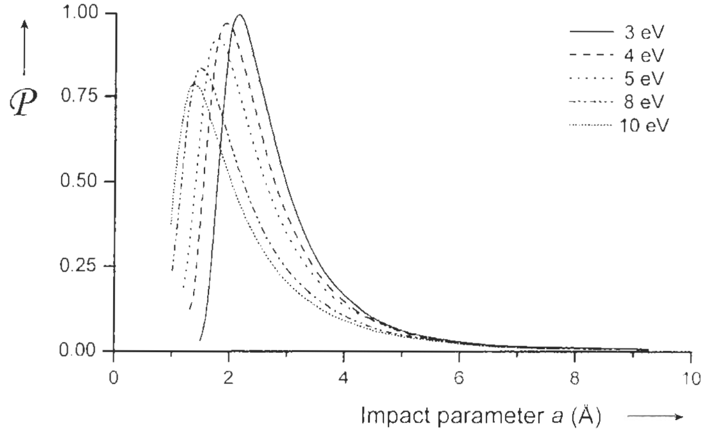

Figure 2.7: Predicted probability of a tunneling electron exciting a fluorophore using Fourmond's second model [26].

After integration, this leads to a transition probability [26],

$$P_{trans} \propto e^{-\frac{b}{b_0}}, \tag{2.21}$$

with $b_0 = \frac{v_e}{\omega_0}$. This first-order approximation gives a good estimate of resolution and a general idea of the probability of a transition, but it also shows the probability is large enough that we should not be using a first order approximation.

Fourmond then proposed a second model that takes into account the dipole's effect on the electron's motion (Fig. 2.6 (b)) [26]. By including this effect, two extra terms are included to the model,

$$\frac{\mathrm{d}\vec{u_e}}{\mathrm{d}t} = \vec{v_e} \tag{2.22}$$

$$\frac{\mathrm{d}\vec{v_e}}{\mathrm{d}t} = \frac{e\vec{E_d}}{m_e} \tag{2.23}$$

with $\vec{u_e}$ the position of the electron with respect to the dipole, $\vec{v_e}$ the electron velocity, m_e the electron mass, and $\vec{E_d}$ the field created by the dipole. The field created by the dipole was estimated using a classical dipole [26],

$$\vec{E_d} = \frac{1}{4\pi\epsilon_0 r^3}\left[3\left(\vec{D}_{class} \cdot \vec{u_e}\right)\vec{u_e} - \vec{D}_{class}\right]. \tag{2.24}$$

This model was solved using numerical integration by steps in t, with each step outputting a new set of $c_0(t)$, $c_1(t)$, $\vec{u_e}(t)$ and $\vec{v_e}(t)$. The probability could then be found using Eq. 2.20, with the output of $c_1(t)$ at large t. The model works well with distances ≥ 0.15 nm and for electron kinetic energies above the dipole transition energies. The result shows an increase in probability as the kinetic energy of the electron decreases: slower electrons spend more time near the dipole and therefore transmit more energy to the dipole (Fig.2.7). It also gives a high probability that a tunneling electron with energy above the dipole transition energy, will excite a fluorophore in the tunneling gap.

Experimentally, Uehara et al. demonstrated that fluorescence could be excited by an STM tunneling current [27]. Their experiment was done in UHV at 80 K, but they attribute their success to attaching the fluorescent probe to highly oriented pyrolytic graphite (HOPG), which has no STM-induced plasmon emission in the visible range (Sec. 2.3.3). HOPG is also conductive and atomically flat. We chose not to use HOPG because it can mimic DNA (Sec. 2.3.1).

2.3 Some complications

We chose to attempt to implement our fluorescence STM imaging technique using labeled DNA deposited on gold. With this setup, there are many barriers that must be overcome to make it possible to image a fluorophore. First, depositing DNA on a conductive surface has been done with limited success and often leads to surface contamination that makes imaging difficult. Second, imaging DNA with an STM leads to images that can be hard to interpret because of changing tunneling conditions. Third, gold imaged with an STM at bias voltages capable of exciting a fluorophore also excite surface plasmons leading to a large background optical signal. Fourth, fluorophores excited near a conductive surface may not emit light because the emission can be quenched by electromagnetic effects. I discuss these complications in this section.

2.3.1 DNA deposition

To properly image DNA using a scanning tunneling microscope, one must strongly attach it to a flat, conductive surface. It is necessary to attach the DNA strongly because forces exerted by the tip contacting the DNA and strong electric fields directly under the tip can move or detach the molecule [28,29]. Flatness is required because the STM identifies DNA as small changes in the topography image due to tip effects, as the electrons tunnel through the DNA. On average, these tip effects create a change in height of 1 nm or less when an STM tip scans over the DNA, which is comparable to the roughness of a few atomic steps. Conductivity is required for tunneling. In addition, in our optical setup (Sec. 3.2), the substrate must be semi-transparent, which further restricts our sample preparation (Sec. 4.1).

Gold is often used to image DNA in an STM because it can be made atomically flat through evaporation onto mica [30, 31] and because it can be easily modified using thiol bonds. Attempts to image DNA with an STM were also made using graphite as a conductive, flat, surface [32], but it is not commonly used now, since graphite itself was later seen to have surface features that can mimic DNA [33, 34].

There have been many different techniques used to immobilize DNA onto gold including electrochemistry [35–37], covalent linking [32, 38], covalent tethering [29, 39, 40], trapping [41, 42], pulse injection [43–50], and electrostatic deposition [51, 52]. In these methods, one attaches DNA strongly to the substrate to prevent the tip of the STM removing the DNA, but the methods differ in the amount of contamination and convenience. Electrochemistry bonds well but leads to contamination problems and is imaged in solution [37]. Both covalent linking and tethering require complicated chemistry, and pulse injection needs to be done in vacuum. Electrostatic deposition is less complicated and creates little contamination.

Electrostatic deposition uses electrostatic charges to attach DNA to a conductive surface. By applying a positive voltage to a surface and grounding a drop of liquid containing DNA on the surface, one creates an electric field in the DNA drop. Placing a large resistor in the circuit minimizes the current, but the positive charge remains on the surface. The positively charged substrate attracts the negatively charged backbone of the DNA, depositing DNA on to the conductive substrate. We chose this technique in our work (Sec. 4.3).

2.3.2 Interpreting DNA images

The images of DNA are not always simple to interpret, as changing tunneling conditions can alter the visibility, contrast, and height of DNA in a topographic image [29]. In attempts to improve image quality, DNA has been scanned with varying voltages (0.1 V to 2.8 V) and varying currents (20 pA to 1 nA). The two problems of image interpretation for an STM imaging DNA are image contrast switching and height variations, which I discuss below.

Contrast inversion is one effect that is seen while scanning DNA with an STM. Depending on the settings of the STM while scanning, the image of DNA can have positive or negative contrast, though contrast inversion also happens spontaneously for the same settings [51]. It is not well understood what causes contrast changes. There are many theories, including buffer solution absorbates left after rinsing [44, 51], poor conductivity of DNA and STM flexibility [39], and tip geometry [53, 54]. When I reviewed the articles imaging DNA on gold, I found that DNA contrast was not a simple function of bias voltage but there was an overall trend. For scanning in air, which limits the bias to ≤ 2.1 V to prevent damage of the substrate [55], most DNA topographic images were negative contrast images. When done in UHV, where it is possible to use a bias above 2.1 V, most DNA topographic images were positive-contrast images. Still, some papers have images that go against this trend [29, 51]

As the varying theories show, the actual images depend on a variety of factors. Shapir *et al.* [51] showed that it was possible to reversibly change the contrast of imaged DNA by a change in the set point current. Kanno *et al.* [44] showed a change from positive to negative contrast when the salt concentration was increased in the DNA buffer solution, leading the authors to conclude that the better conducting buffer species are topographically higher than the DNA in an STM image, producing negative contrast. To date, these seem to be the only two papers that show a reproducible change in contrast with a single variable change, though many papers show a spontaneous change in DNA contrast without any change in variables [29, 40, 51].

The height of DNA displayed on a topographic STM image also depends on the both the bias voltage and current set point, as well as tunneling conditions. Shapir *et al.* [51] showed that bias voltage affects the measured DNA height on images, with an increase in bias voltage causing an increase in image height. In another study by Shapir *et al.* [52], we see that measured topographic DNA height varies from 0.5 nm to 1.2 nm on like DNA molecules without a change in bias voltage or current set point, likely due to changing tunneling conditions. In a more drastic height change, Allison *et al.* report that DNA can appear spontaneously in an imaged area that showed no DNA in previous scans. Because

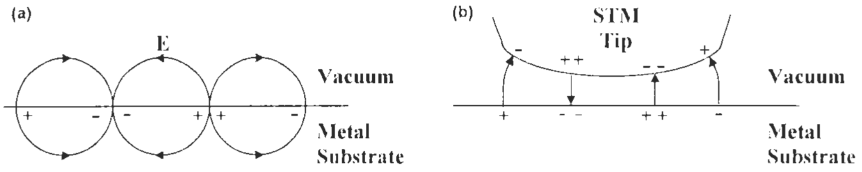

Figure 2.8: Diagram of surface plasmon modes. (a) Mode for a metal-vacuum interface. (b) Mode leading to localized surface plasmons between the STM tip and a metal substrate. [56]

of changes in visibility and in characteristics, one is challenged to interpret physical details from topographical images of DNA that are acquired by STM. For these reasons, AFM is a much more commonly used imaging technique for DNA.

2.3.3 Surface-plasmon-induced light emission

The study of surface-plasmon-induced light emission has increased in the last few decades after it was found that it could be studied in a controlled manner using a scanning tunneling microscope. The STM has a unique ability to excite surface plasmons and greatly enhance the light emission from them. In this section, I describe the physics behind this phenomenon, which could potentially overpower the light emission from the fluorophores we are trying to image.

Surface plasmons are electromagnetic waves that propagate along the interface of a metal and a dielectric. The waves propagate by producing dipole polarization charges as seen in Fig. 2.8a. Surface plasmons propagating in the x-direction produce electric fields [56],

$$E = (E_{xd}\hat{x} + E_{zd}\hat{z})e^{i(k_x x - \omega t)}e^{k_{zd} z} \text{ in the dielectric} \quad (2.25)$$

$$E = (E_{xm}\hat{x} + E_{zm}\hat{z})e^{i(k_x x - \omega t)}e^{-k_{zm} z} \text{ in the metal} \quad (2.26)$$

with k_x the wave vector in the x-direction, k_{zn} the wave vector in the z-direction in material n, and ω the frequency of the surface plasmon wave.

To derive the major features of a surface plasmon wave, one can use the regular boundary conditions ($D_{1\perp} = D_{2\perp}$ and $E_{1||} = E_{2||}$) and Maxwell's equations to show [57],

$$\begin{aligned} k_{zd}^2 &= k_x^2 - \epsilon_d \mu_0 \omega^2 && (2.27) \\ k_{zm}^2 &= k_x^2 - \epsilon_m(\omega) \mu_0 \omega^2 && (2.28) \\ E_{zd} k_{zd} &= -E_{zm} k_{zm} && (2.29) \\ \epsilon_d E_{zd} &= \epsilon_m(\omega) E_{zm}, && (2.30) \end{aligned}$$

with ϵ_n permittivity of material n. For a surface plasmon, the wavelength is small compared to the wavelength of a photon with the same energy, implying that $ck \gg \omega$ [119]. With this requirement, Eqs. 2.27 and 2.28 imply that k_{zn} is real and positive, leading to exponential decay in the z-direction. With a positive and real k_{zn}, Eqs. 2.29 and 2.30 require that the two materials have permittivity of opposite sign. The easiest way to achieve this is to use a metal-dielectric interface. One can also combine Eqs. 2.27–2.30 to derive the dispersion relationship for a surface plasmon [57],

$$k_x = \frac{\omega_s}{c} \sqrt{\frac{\varepsilon_m(\omega_s)\varepsilon_d}{\varepsilon_m(\omega_s) + \varepsilon_d}}, \tag{2.31}$$

with ω_s the surface plasmon frequency, ε_d the dielectric constant of the dielectric material interfaced with the metal, and $\varepsilon_m(\omega_s)$ the dielectric function of the metal. To have a surface plasmon that propagates along the metal-air interface, k_x must have a real part. This fact, combined with the result that the permittivity of the metal and dielectric must be opposite in sign, requires that $|\varepsilon_m| \geq |\varepsilon_d|$. For a Drude metal with $\omega_s \gg 1$, the dielectric function is $\varepsilon_m(\omega_s) \approx 1 - \omega_p^2/\omega_s^2$, which is typically negative at optical frequencies [119]. Solving the dielectric function for ω_s and using the result $|\varepsilon_m| \geq |\varepsilon_d|$, gives an estimate of the maximum surface plasmon frequency at the interface,

$$(\omega_s)_{max} = \frac{\omega_p}{\sqrt{\varepsilon_d + 1}}, \tag{2.32}$$

with ω_p the plasma frequency for the metal. For a metal-vacuum interface, similar to our air-metal interface, Eq. 2.32 leads to the Stern-Ferell result, $\omega_s^2 = \omega_p^2/2$, for the frequency of a surface plasmon oscillation [58].

When two conducting surfaces are brought within angstroms of each other and separated by a dielectric material, it is possible for surface plasmons of two conductors to couple together, creating new properties and enhancing the plasmon oscillations. One example of this, relevant to our work, occurs when a conducting tip is brought within tunneling distance to a conducting substrate. The evanescent electromagnetic waves from the surface plasmons in both the tip and the substrate will then couple and polarize each other in a small region located under the tip ($\approx$ 10 nm), as seen in Fig. 2.8b [59]. This leads to a strong enhancement ($\approx$ 100 X) of the electromagnetic field of the surface plasmons localized under the tip [61, 62]. To estimate the resonance frequencies of the localized surface plasmons (LSP), one can use [63]

$$\omega_r = \omega_p \sqrt{qd/2}, \tag{2.33}$$

with ω_p the plasmon frequency of the substrate, d the tip-sample distance, and q the wavenumber of the resonance mode. For a tip-sample distance, d, sufficiently smaller than the radius of the tip, R, the wavenumber can be estimated using $q_1 \approx (2Rd)^{-1/2}$, with $q_n = nq_1$. This leads to a spectrum of LSP frequencies given by

$$\omega_n = \sqrt{n}\omega_p \left(\frac{d}{8R}\right)^{1/4}. \tag{2.34}$$

For an STM producing an LSP, electrons that tunnel between the tip and the substrate with wave vectors parallel to the enhanced LSP can couple to the electromagnetic field and excite the LSP through inelastic tunneling [64,65]. The probability that a tunneling electron excites an LSP is [65]

$$P_{inel} \approx \frac{e^2\omega_n d^2 m}{4W\hbar R}\left(1 - \frac{h\omega_n}{eV}\right), \tag{2.35}$$

with ω_n the LSP resonant frequency, d the tunneling distance, m the mass of the tunneling electron, W the barrier height, R the tip radius and V the tip-sample bias. Normally, an excited surface plasmon cannot emit light because of conservation of momentum: For a surface plasmon to exist, the metal must have a permittivity that is negative and larger than the permittivity of the dielectric causing the momentum of a surface plasmon (Eq. 2.31) to always be greater than that of a plane wave ($k_{p\omega} = (\omega/c)\sqrt{\varepsilon_d}$) traveling parallel to the surface. It is possible though for an excited surface plasmon to decay into a photon if there is a loss in translational invariance on the surface [66]. The enhanced LSP created under the tip gives the needed invariance loss and allows light to be emitted from the tunneling junction [66]. This process produces light-emission rates of $\approx 10^{-4}$ photons per tunneling electron [66, 67].

An image created by recording plasmon emission has certain features because of the way emission is created. The resolution of a plasmon emission image is expected to be determined by the area under the tip that creates a localized surface plasmon ($\approx$ 10 nm). Berndt et al. found that contrast in plasmon emission is actually better than this ($\approx$ 2 nm) [68]. This small-scale resolution is explained by considering the LSP to be a dipole, whose emission is greatest when the dipole moment of the LSP and the tunneling current vector are parallel. When the tip approaches a defect the tunneling current at the defect is no longer parallel to the dipole moment causing a drop in emission that is dependent on the tunneling current width and not the lateral extent of the LSP. The plasmon emission is estimated to be $\propto \cos^2\theta$, with θ the angle between the tunneling vector and the surface normal [69]. As regards our imaging method, we expect plasmon photon emission to be significant; however, as long as the wavelengths of the plasmon and fluorescence emission differ, the two effects can be separated.

2.3.4 Quenching

When a fluorophore is close to a conductive substrate, there is an additional pathway for the fluorophore to decay from an excited state to the ground state. This pathway involves the transfer of energy from the excited fluorophore to the conductive substrate. When this pathway is available, fluorophore emission will decrease. In our experiment, this is the case, as both the gold substrate and the Pt-Ir STM tip are $\approx$ 1 nm away from the fluorophore.

In our experiment, we model the dye molecule as an oscillating dipole close to the conducting substrate. With this setup, the conducting substrate produces a field equivalent to that of an image dipole inside itself of equal and opposite moment. The image dipole then oscillates (nearly) out of phase with the dye molecule and produces a reflected field at the dipole of [70]

$$E_R(\omega) = \left(\frac{\epsilon_m(\omega) - \epsilon_d}{\epsilon_m(\omega) + \epsilon_d}\right) E_R^{ideal}(\omega), \tag{2.36}$$

with $\epsilon_m(\omega)$ and ϵ_d the dielectric function of the metal and the material the dipole is in respectively, and E_R^{ideal} the electric field from a perfect image dipole in the metal [70].

$$E_R^{ideal}(\omega) = \mu \frac{k_1^3}{n_1^2} e^{i2d} \left[(2d)^{-3} - i(2d)^{-2} - (2d)^{-1}\right], \tag{2.37}$$

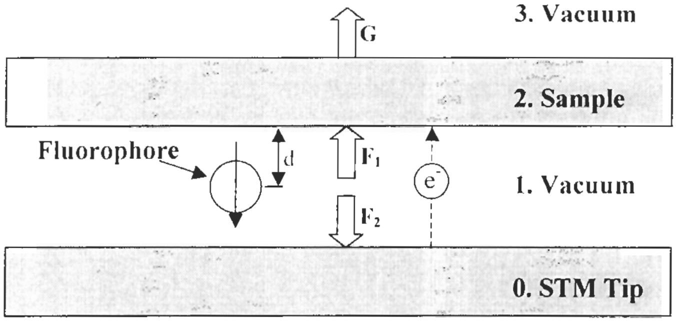

Figure 2.9: Model used to calculate emission efficiency for a fluorophore in a tunneling gap. Medium 3 is the location of our light collection optics.

with d the distance between the fluorophore and substrate, μ the dipole moment, k_1 the propagation constant ($k_1 = \omega n_1/c$), and n_1 the refractive index of the material surrounding the "real" dipole.

The image dipole has two effects on emission: the dipole in the metal will oscillate almost completely out of phase, canceling out part of the signal of the fluorophore: and the oscillation in the metal creates phonons that transfer energy of the excited fluorophore into heating the gold. Both effects are not fundamental problems because they reduces emission rates by creating new pathways for the excited fluorophore to relax into its ground state without emitting a photon. This allows these effects to be overcome by increasing the rate at which one excites the fluorophore [71]. Together, at small d, these effects lead to an energy transfer decay-rate constant of [70]

$$\hat{b}_{ET} = \beta d^{-3}, \tag{2.38}$$

with β the energy transfer rate parameter, which is a constant for an absorbing film thickness greater than d [70]. The quantum efficiency for a fluorophore is

$$QE = \frac{\hat{b}_r}{\hat{b}_r + \hat{b}_{ET} + \hat{b}_{nr}}. \tag{2.39}$$

with $\hat{b}_r$ the radiative decay-rate constant and $\hat{b}_{nr}$ is the non-radiative decay rate constant from processes other than energy transfer to the absorbing film. From Eq. 2.39, we expect that a conductive metal substrate, with substrate thickness greater than d, will reduce emission for a fluorophore by an inverse cubic dependence in d.

Values for Estimation of Emission Efficiency			
Material	refractive index	absorption coefficient	distance to fluorophore
Gold	0.6	2.1	1 nm
Platinum	2	3.5	1 nm

Table 2.1: Values for estimation of emission efficiency

Theoretically, quenching has been modeled for our system [26] assuming a four-layer system (Fig. 2.9) to find the efficiency of light emission from a fluorophore per tunneling electron. This was done by computing the ratio of the total energy flux through a plane in medium 3, where light collection occurs, to the total energy flux emitted from the radiating dipole. For this model, the efficiency is [26]

$$\varepsilon = \frac{G}{F_1 + F_2}, \tag{2.40}$$

with F_1 and F_2 the energy flux into the sample and the tip, respectively, in medium 1 and G the energy flux in medium 3. When the different fields and fluxes are included in the model, the emission efficiency, ε, is [26]

$$\varepsilon = \frac{2\hat{d}^3 e^{-2\kappa_2 \ell} \left| \frac{2\widetilde{n_0}}{\widetilde{n_0}+1} \right|}{3\mathrm{Im}\left[\frac{\epsilon_0 - 1}{\epsilon_0 + 1} + \frac{\epsilon_2 - 1}{\epsilon_2 + 1} \right]}, \tag{2.41}$$

with $\widetilde{n}_j = n_j + ik_j \approx \sqrt{\epsilon_j}$ the complex index of medium j, $\hat{d} = k_1 d$ ($k_1 = \frac{2\pi}{\lambda}$ the wave vector in medium 1 and d the distance between the dipole and the substrate) and $\ell = -k_1 z$ (z the thickness of the substrate). This model reproduces the cubic distance dependence on emission and was used for our system, with gold as the substrate, platinum as the metal tip, and YOYO-1 as the dye ($\lambda = 510$ nm), to estimate an efficiency of photon emission by a dipole of $\approx 10^{-5}/e^-$ [72] using values from Table 2.1.

The above model assumes a perfectly flat substrate and tip; but in our experiment, both of these are not flat. Zhang *et al.*, showed that a rough metal surface in close proximity to a fluorophore can enhance fluorescence [73]. In this study, they used a rough gold surface, with a silica spacer between the fluorophore and gold film, to enhance emission by up to 6 times. With the rough Pt-Ir STM tips and irregularities in our atomically flat gold films, it is possible that emission intensity is enhanced, leading to an increase in the above efficiency of photon emission per electron.

In our experiment, we are trying to excite single fluorophores making the total number of photons emitted per fluorophore an important parameter. We expect that a fluorophore is able to emit $\approx 10^5$ photons before photobleaching [74–76]. The efficiency of our detector optics, 0.007 (Sec. 5.1.1-APD case), allow us to capture ≈ 700 photons per fluorophore before photobleaching. For an STM, if one uses a tunneling current of 1 nA ($\approx 10^{10}$ electrons/s) to excite a fluorophore, the estimated efficiency of photon emission ($10^{-5}/e^-$) combined with the quantum yield of the dye we used, TOTO-3 (0.06) [77], gives a rate of 6 x 10^3 photons per second. This tunneling current gives us a photobleaching rate of ≈ 16 second and allows us to record 42 photons per second. We have measured the dark count (14.5 counts/s) and read noise (2 count) for our APD (Sec. 3.2.3) which allows us to compare the fluorophore signal to our noise. Using a signal to noise ratio,

$$S/N = \frac{Pt}{\sqrt{Pt + D_c t + {R_n}^2}}. \tag{2.42}$$

with the P the signal rate (counts/s), D_c the dark-count rate, R_n the read noise, and t the time of integration, we need to collect light from a fluorophore excited by 1 nA of current for 70 ms to get a signal to noise ratio of one.

Chapter 3

Instrumentation

We have developed a home-built scanning tunneling microscope (STM) that can collect light from the tunneling region. Our STM was home-built in order to integrate an efficient light collection system in the instrument design. With this light-collection system, our STM can record simultaneous topographical and light-intensity images of a scanned surface. In this chapter, we discuss the STM mechanics and optics that contribute to our topographical and light-emission imaging. For further details concerning the STM, see the report of Verhage [72].

3.1 STM mechanics

Our STM has many mechanical components that work together to produce good-quality images. In this section, we discuss those components, beginning with the approach and scanning mechanisms. Next, we discuss the different tips used in our experiments. Finally, our method of vibration isolation is discussed.

3.1.1 Z control

In this section, we discuss the design of the Z-motion components of the STM. By convention, the sample sits in the XY plane, so that Z-motion is perpendicular to the sample plane. The Z-motion system needs to produce and control motion over many orders of magnitude, from millimeters to angstroms. The required Z-motion of the STM can be classified into

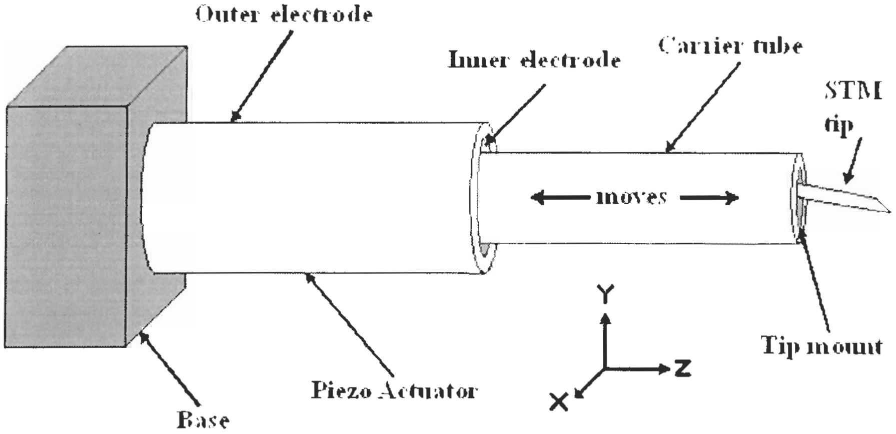

Figure 3.1: Schematic diagram of the Nanomotor [78] used for approaching the sample using a stick-slip operation and for creating topographic images while scanning in a fine position mode

three different types: coarse approach, fine approach, and scanning. While most of our STM is home built, we use a commercial component, the "Nanomotor" [78] to create all three types of motion in the Z direction with a single piezo actuator, as seen in Fig. 3.1. The tip is placed in a carrier tube held by friction inside a piezo actuator. The tip itself is also held by friction inside the carrier tube.

Moving the tip from several millimeters to within an angstrom of the sample surface involves two steps. First, a coarse approach is used to manually bring the tip close ($\approx 1\mu$m) to the surface of the sample. To aid in this, a miniature video camera [79] is placed a short distance from the tip and sample. The coarse approach is achieved using a stick-slip motion created by applying a sawtooth waveform (Fig. 3.2a) to the piezo actuator. During the ramp section of the sawtooth, the piezo actuator expands, moving the carrier tube holding the tip towards the substrate surface. At the end of the sawtooth ramp, the voltage drops steeply and the actuator rapidly retracts, overcoming the friction between the actuator and the carrier tube, leaving the carrier tube stationary. The process is repeated, moving the carrier tube and tip 280 nm closer to the substrate surface with each cycle. This gives the tip a coarse-motion range of 5.7 mm and can be set to work from 1 Hz to 1500 Hz. A 1000-Hz step rate then corresponds to a coarse velocity of 280 μm/s. Second, a fine

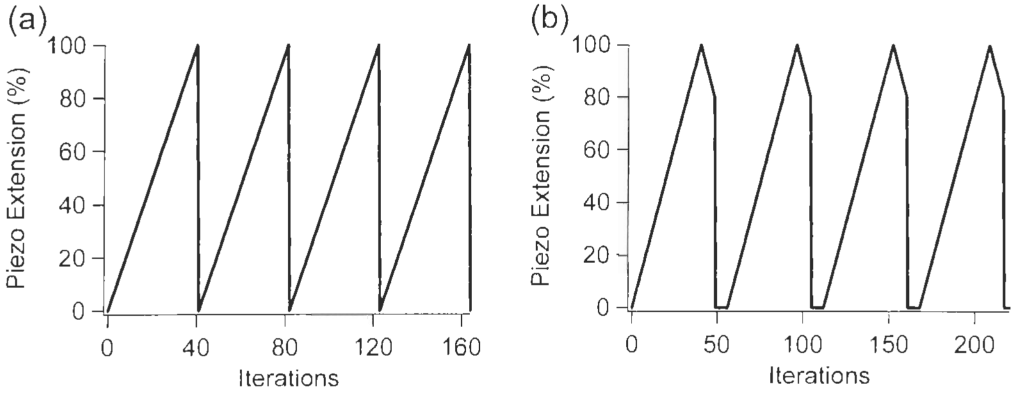

Figure 3.2: Waveform for producing stick-slip motion. (a) Sawtooth waveform. This waveform led to erratic displacement of the carrier tube. (b) Modified sawtooth waveform producing regular carrier motion. Retracting from full extension before the slip motion prevents any erratic motion from damaging the tip when close to the substrate. The resting period after the slip motion allows for any erratic motion to die out before the next cycle begins.

approach is programmed into the software that brings the tip into tunneling distances of the sample. In the fine-approach program, I set the sawtooth frequency to 5 Hz and measure the tunneling current after each voltage increment on the sawtooth ramp, until a set current level is reached. Once the set current is reached, the STM goes into feedback mode and is ready for scanning.

A basic sawtooth waveform turned out to be a poor choice for the fine approach because it produced many false feedbacks and crashed tips. Both of these effects are caused by large erratic movements of the piezo after the slip motion, probably because shock waves reflect and cause delayed, unintended motion of the carrier. False feedbacks are produced when the unintended motion creates a current that is misinterpreted as electron tunneling from the tip to the surface. The origin of this current lies in a change in capacitance created between the tip and sample by the approach [80]. From the charge relation of a capacitor, $Q = CV$, one has, for constant applied voltage,

$$I = V\dot{C}. \tag{3.1}$$

The capacitance depends on the tip-sample distance, d, leading to a change in capacitance

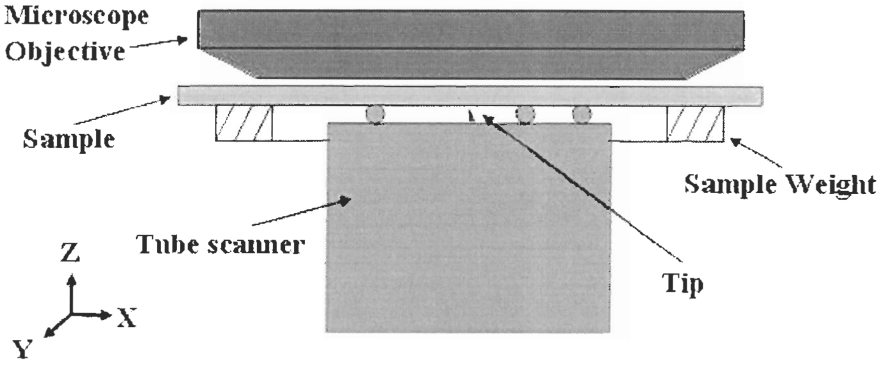

Figure 3.3: Sample location in our STM. The sample rest on the tube scanner used for X and Y motion.

when the tip approaches the surface,

$$\dot{C} = -\frac{\epsilon_0 A \dot{d}}{d^2} = -C\frac{\dot{d}}{d}, \tag{3.2}$$

where A is an effective area of the end of the STM tip. This change becomes large when the tip is very close to the substrate ($d \rightarrow 0$). I eliminated most false feedbacks by introducing a rest period after the slip motion and not checking the current during the slip motion or rest period. The crashed tips are caused by the erratic motion moving the tip when it is already very close to the sample; this was prevented by slowly retracting the tip from its fully extended position before going through the slip process. Reducing false feedbacks and crashed tips resulted in the approach waveform shown in Fig. 3.2b.

After feedback has been established, the piezo follows the surface profile as the outer tube scanner moves the sample horizontally (Sec. 3.1.2). While the STM is scanning, a voltage is applied to change the length of the piezo actuator, using feedback to keep the tunneling current at the set point. The change in length of the actuator moves the carrier tube and tip, keeping the tip a constant distance from the surface. The piezo actuator has a total fine-position range of $\approx 1\ \mu$m.

3.1.2 X and Y control

To create a scan, we must move the tip horizontally with respect to the sample. For our setup, the sample is placed on top of a tube scanner (Fig. 3.3). The tube scanner gives the

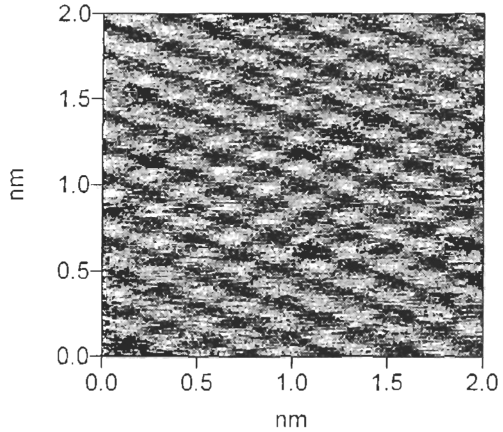

Figure 3.4: Graphite lattice, as seen with our STM.

X and Y displacement by moving the sample, while the Z motion is produced by the piezo actuator. This tube scanner has its outside wall etched into four equally sized segments. Voltage is then applied to opposite sides of the piezo to move the scanner and sample horizontally. The tube scanner can produce a displacement of 4.0 nm/V by bending towards the direction of movement. When the tube scanner bends, it also moves in the Z direction, creating an approximately parabolic profile in the topography images that must be canceled out in the software.

3.1.3 Tip production

The sharpness of tips used in an STM affects the resolution of the images produced. For good imaging, one needs sharp tips, tunneling from a single atom. With our setup, it is also necessary to align the optical equipment with the tip to capture light while imaging. We produced sharp tips by cutting a platinum-iridium wire at a 45° angle while pulling the cutters away from the tip. The cut tips could be used to image the atomic lattice of highly oriented pyrolitic graphite (HOPG) (Fig. 3.4). On the other hand, the actual point from which electrons were tunneling was hard to determine, which made the optical alignment difficult. As an alternative, I used electrochemical etching on tungsten wire to create a more reproducible tip shape for easier optical alignment. I produced tungsten tips with an

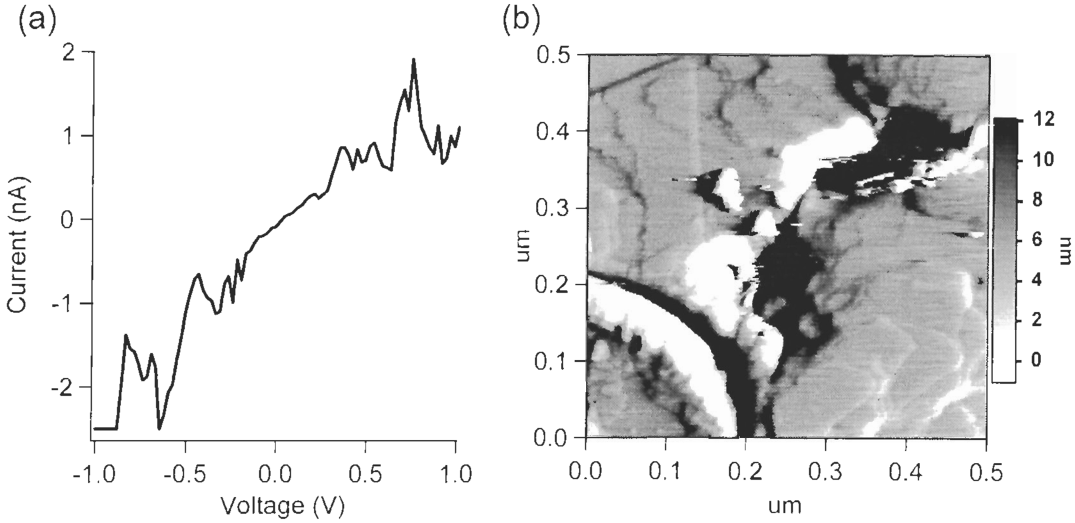

Figure 3.5: IV curve and topographic image of gold for a good tungsten tip. (a) Ohmic response of the IV curve for a tungsten tip cleaned by HCl. (b) Image of gold, taken soon after the IV curve, showing faceting.

etched cone shape that were sharp enough to use in the STM; however, only a few of these tips worked because of a tungsten-oxide contamination layer that was regularly coating the etched part of the tip [81]. I attempted to remove this contamination layer using hydrochloric acid, but the results were not reproducible. To get a better understanding of the cleaning process, I programmed an IV curve setting for the STM to study the changes in conductivity versus my cleaning procedure. From this, I hoped to find the cleaning procedures needed to produce a nearly ohmic response at low bias voltage, which is the response of a clean tungsten tip [82]. After cleaning, the tungsten tips occasionally produced nearly ohmic IV curves and good images under tunneling conditions (Fig. 3.5), but imaging only lasted for a few hours before the tunneling current would cease, causing the tip to make contact with the surface. Since we were scanning in air, this was likely due to further oxidation of the tip during scanning.

Because of the unreliable tunneling of tungsten tips in air, all the work done in this thesis used cut Pt-Ir tips. Though locating the tip apex optically was more challenging with Pt-Ir tips, I could consistently create sharp tips for good imaging, without any worry of oxidation.

3.1.4 Vibration isolation

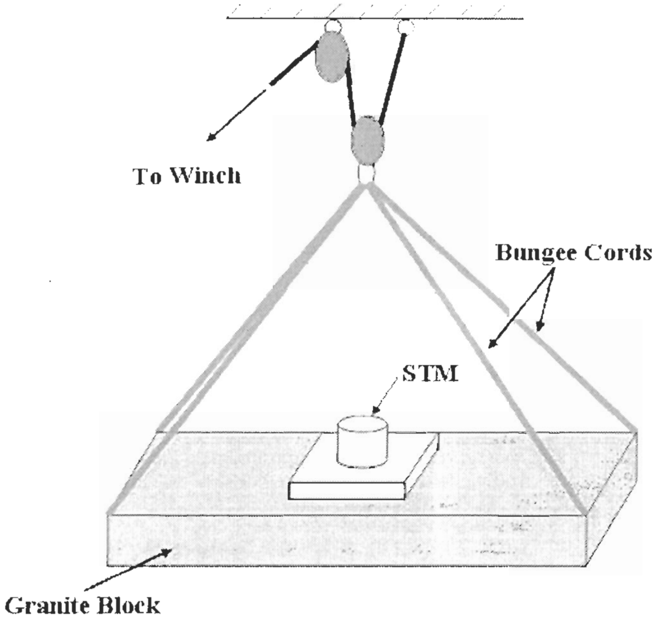

Figure 3.6: Diagram of our STM, with "bungee-cord" isolation.

For good-quality imaging, one needs to reduce any noise as much as possible. One source of noise for the STM is mechanical vibration from its surroundings. To reduce this source of noise, we isolated the STM from the building using a soft elastic suspension [83, 84]. The mechanical parts of the STM are placed on a large granite block (50 cm x 50 cm x 8 cm, $m \approx 75$ Kg) and using bungee cords and a winch (Fig. 3.6), we suspend the block in air. This setup can be modeled as a mass on a damped spring. The equation of motion for the mass (base plus STM) is then

$$m\ddot{x}(t) + \lambda'(\dot{x}(t) - \dot{r}(t)) + k(x(t) - r(t)) = 0. \tag{3.3}$$

where $x(t)$ is the displacement of the mass and $r(t)$ represents the displacement of the mechanical attachment point (the roof). To see the effect of roof movement on the STM,

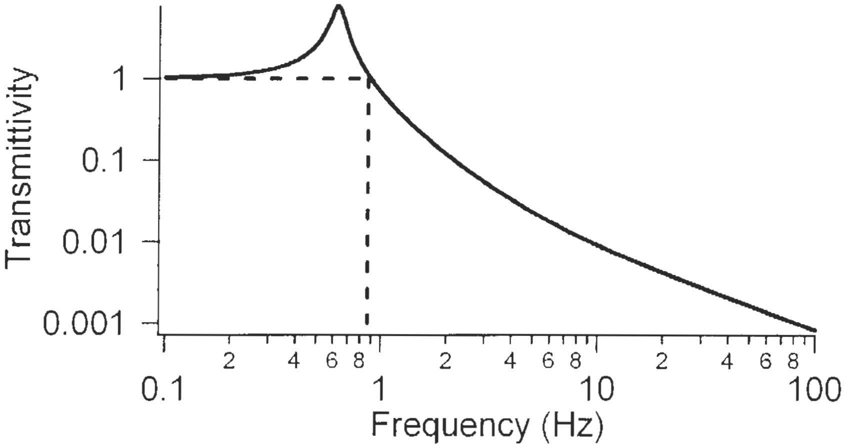

Figure 3.7: Vertical vibration transmission for our STM. The solid line is an estimate of the transmittivity of our system with a resonant frequency of 0.75Hz and $\zeta = 0.1$. Vibrations whose frequency is greater than 0.85 Hz are damped (vertical dashed line).

we can look at the transfer function of the system,

$$T(\omega) = \frac{x(\omega)}{r(\omega)} = \frac{1 + i2\zeta\frac{\omega}{\omega_o}}{1 + i2\zeta\frac{\omega}{\omega_o} - \frac{\omega^2}{\omega_o^2}}, \tag{3.4}$$

where ω is the frequency of the building vibrations, $\omega_o = \sqrt{\frac{k}{m}}$ is the resonance frequency of the undamped system and $\zeta = \frac{\lambda'}{2m\omega_o}$ is a dimensionless damping parameter. I found that the resonant frequency of the system is ≈ 0.75 Hz and the damping coefficient of the bungee cords $\zeta \approx 0.1$. The ratio of the amplitude of the vibrations between the roof and the STM is the absolute value of the the transfer function, or transmittivity,

$$|T(\omega)| = \sqrt{\frac{1 + 4\zeta^2(\frac{\omega}{\omega_o})^2}{(1 - \frac{\omega^2}{\omega_o^2})^2 + 4\zeta^2(\frac{\omega}{\omega_o})^2}}, \tag{3.5}$$

and is shown in Fig. 3.7 for our resonant frequency and damping parameter. Our model shows that the transmittivity is near unity at low frequency. Then, there is a nearly tenfold resonant enhancement near the resonance frequency of the system, followed by damping of vibrations for frequencies ≥ 0.85 Hz, as shown by the dotted line on Fig. 3.7. The resonance

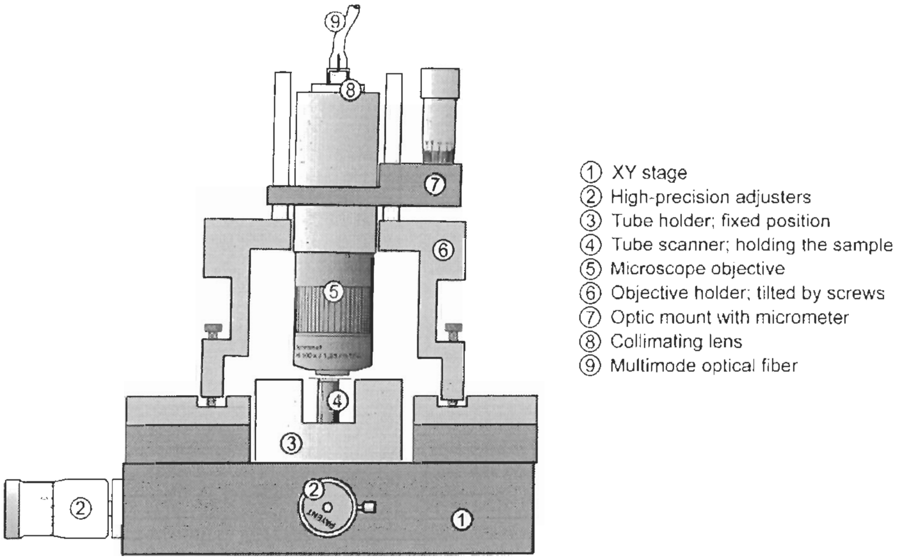

Figure 3.8: Diagram of the STM setup [72].

enhancement and higher frequency behaviour depends on the damping parameter. Our damping parameter is a practical compromise between increased resonance enhancement and increased damping of the high frequency vibrations.

Other sources of mechanical "noise" include sound and other high frequency vibrations, which cover a wide frequency range, from around 100 Hz to several kHz. These vibrations are minimized best by making the STM small and rigid. The resonance frequencies of our STM are on the order of 10 kHz because of its compact design. This ensures that neither vibrations in the surrounding air nor scanning movements made by the STM will excite the resonant frequencies.

3.2 STM optics

To capture light produced from the tip while scanning with the STM, detection optics need to be able to focus on the scanning region. Because of the low light levels in our experiment, it is important to maximize the amount of light captured while shielding against stray light. Overall, the capturing of light produced by an STM can be broken into two problems, the

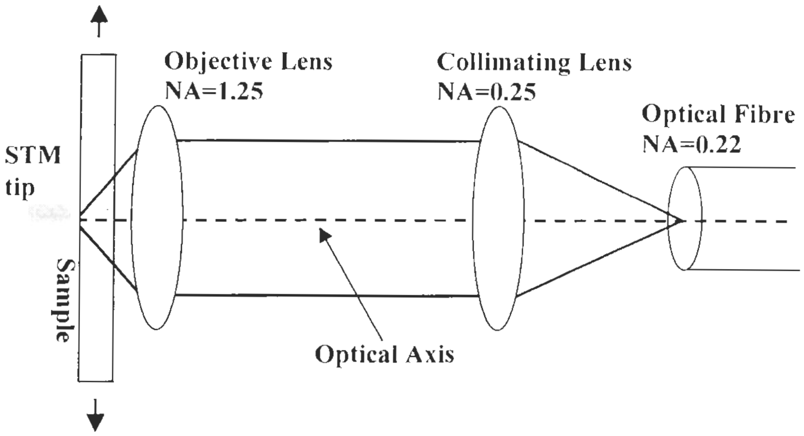

Figure 3.9: Optics inside the objective holder.

mechanics of focusing the optics and the efficiency of the optics and detector.

The light-capturing apparatus consists of a microscope-objective holder designed to prevent stray light from entering the experiment and to hold the light-focusing apparatus, a microscope objective focused on the tip location, and a collimating lens to focus the light captured by the objective onto a fibre-optic cable (Fig. 3.8). We use two different fibre-optic cables, depending on whether the light was analyzed by the avalanche photodiode or by the spectrometer. A simple diagram of the optics is shown in Fig. 3.9.

3.2.1 Focusing mechanics

The mechanical focusing of the optics is of great importance for capturing as much light as possible from the scan area. Our system was designed to move the optics independent of the STM and to keep the tip position horizontally stationary at all times. This allows the optics to be focused once for a new tip and then be kept stationary until that tip is replaced.

Focusing of the optics on the scan region uses two separate mechanisms: a vertical and a horizontal translation mechanism. The vertical focusing is done by the objective holder, which holds all the optical components and translates vertically to put the sample

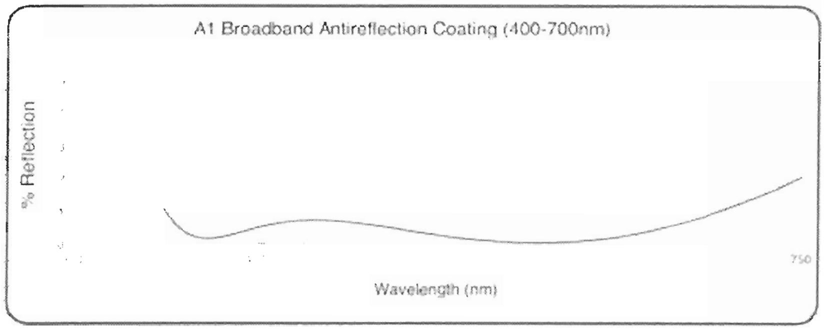

Figure 3.10: Antireflective coating of the collimating lens [85].

in the focal plane of the objective. The objective holder does this by holding in place the distances between the objective, collimator and optical fibre, while allowing all three of these to be translated vertically with respect to the sample. Vertical focusing needs to be precise because collection efficiency for our setup has a sharp decline on either side of the optimal vertical focus [72]. The horizontal positioning uses an xy-stage that the objective holder is mounted on. The xy-stage moves independent of the sample and tip, allowing the objective lens to be positioned over the scan region, aligning the optical axis with the tip apex. Horizontal focusing does not have to be as precise as the vertical focus because the spot size of the objective (≈ 2 μm) is larger than the area of plasmon emission (≈ 10 nm) and scan range ($\approx 1\mu$m), creating a plateau at peak collection efficiency before a sharp decline [72]. Once the optics are properly focused, it is not necessary to move them while scanning because the tip is stationary with respect to the optical axis while the sample is moving (Fig. 3.9).

3.2.2 Light-collection optics

In our setup, we chose the collection optics to maximize the efficiency of photon detection while maintaining the topographical quality of the STM. In our optical experiments, we are only interested in the quantity and wavelength of photons, allowing us to maximize collected light for these two parameters without worrying about forming an image.

Three optical components work together to capture and transfer light to the detectors:

Detector analysis		
Type	APD	Spectrometer
Dark Count	14.5 ± 0.3 counts/s	2.81 ± 0.08 counts/s/channel
Read Noise	2 ± 1 counts	4.9 ± 0.1 counts/channel
Gain	0.82 ± 0.03 e/count	4.3 ± 0.1 e/count

Table 3.1: Analysis of the detector

a microscope objective to capture light, a collimating lens to focus the collected light, and an optical fibre to transfer the collected light to the detectors. The objective used was an infinity-corrected Carl Zeiss HI 100x magnification oil-immersion objective [86] with a numerical aperture of 1.25. This objective was used without oil, which gives it an approximate effective numerical aperture of 0.82. Not using oil prevents vibrational coupling between the sample and the objective holder. Although the lack of immersion oil leads to significant aberrations, the primary purpose of the objective was to collect light, not to form an image. We used two different collimating lenses, which gave us a choice of two different diameters of parallel light that could be coupled from the microscope objective to the optical fibres. Both have a numerical aperture of 0.28 and an antireflective coating (Fig. 3.10), allowing the light we are interested in to be focused on to the optical fibres. The optical fibre has a numerical aperture of 0.25. The detectors used to analyze the light signal are discussed in the next two sections.

3.2.3 Avalanche photodiode

The avalanche photodiode (APD) is the main detector used to image the plasmon emissions from the tunneling current of the STM. It outputs TTL pulses corresponding to photon counts while the STM scans. These photon counts are summed by our program and read off at the beginning and end of each pixel to give the counts per pixel. The APD collects light over the wavelength range of 400 nm to 1100 nm, with a quantum efficiency that approaches 90% in the red and near-IR regions (Fig. 3.11a). The results of APD analysis are found in Table 3.1. The dark count was found using the slope of Fig. 3.11c. The gain and read noise were found using

$$V = S/G + R_N^2/G^2. \tag{3.6}$$

with V the variance, S the mean counts, G the gain, and R_N the read noise, on Fig. 3.11e [87].

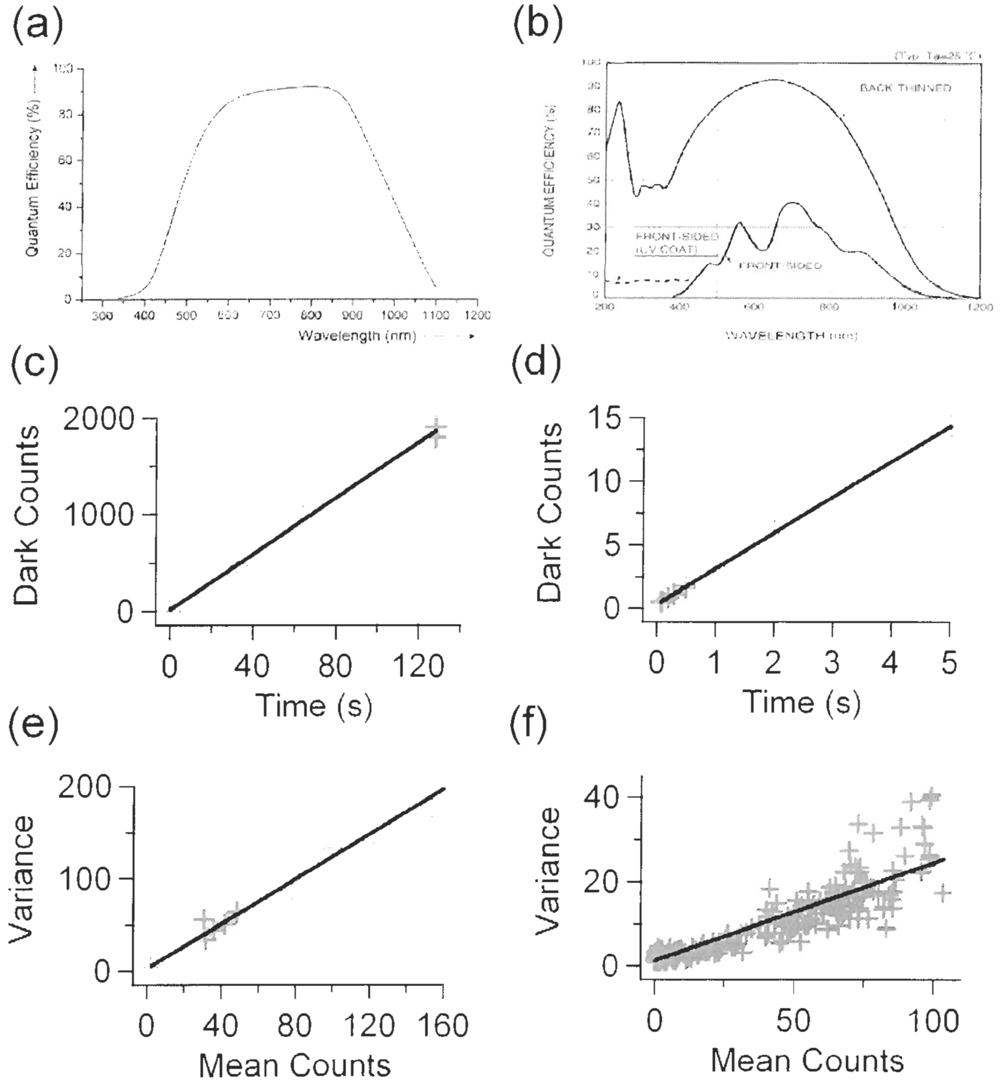

Figure 3.11: Analysis of our optical equipment. (a), (c), and (e) Quantum efficiency, dark noise and measurement made to find the gain and read noise of the APD [90], respectively. (b), (d), (f) Similar plots using the spectrometer with back-thinned CCD [91].

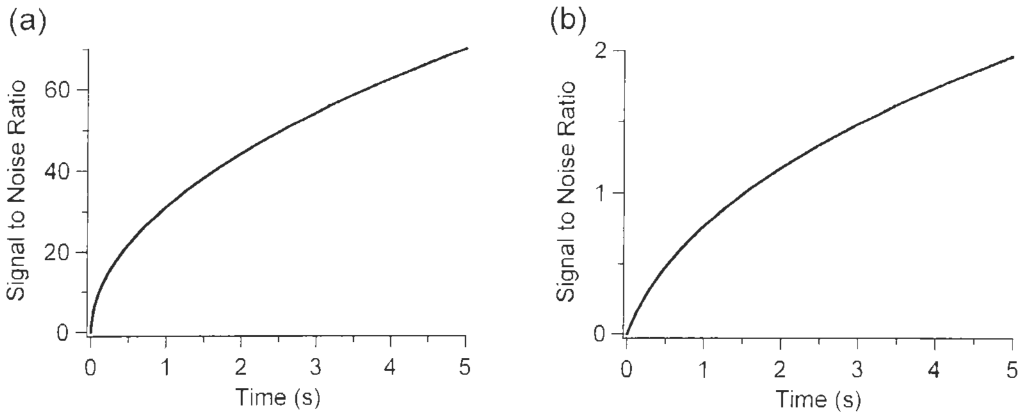

Figure 3.12: Signal-to-noise ratio for the APD and spectrometer. (a) Signal-to-noise ratio for the APD with an average signal of 1000 counts per second while scanning at 2.05 V and 2 nA. (b) Signal-to-noise ratio for the spectrometer with the average signal of ≈ 6 counts per second per channel while scanning at 2.05 V and 20 nA.

To find the APDs minimum integration time for a signal larger than noise, I used the signal-to-noise ratio [88],

$$S/N = \frac{Pt}{\sqrt{Pt + D_c t + {R_n}^2}}. \tag{3.7}$$

with P the signal rate (counts/s), D_c the dark-count rate, R_n the read noise, and t the time of integration. With the noise measurements found in Table 3.1 and a typical signal rate while scanning of 1000 counts/s at 2.05 V bias and 2 nA, I plotted the signal-to-noise ratio in Fig. 3.12a. From this graph, I found a 1:1 signal to noise ratio, with our average signal, at ≈ 3 ms of integration time. This limits us to a maximum scan rate of 500 pixels/s while using the APD.

3.2.4 Spectrometer

We need to observe the spectrum of our optical signal to confirm our results are consistent with previous results; as well as obtaining a better understanding of new results. For spectral measurements, we used a cooled CCD spectrometer, QE65000 [89], able to collect a spectrum over a range from 200 nm to 1015 nm. It uses an array of 1024 x 58 pixels, each pixel $\approx 25\ \mu\text{m}^2$, to collect light. A spectral signal is spread across the 1024 pixels lengthwise using a reflective grating and mirror. Each 58 pixel width is binned to act like a single 58 x 25 μm long pixel, giving a spectrometer readout of only the 1024 channels.

It was necessary to analyze the output of our spectrometer to find the limits in which it could be used. The detector has a quantum efficiency approaching 90% in the red to near IR regions, as shown in Fig. 3.11b. The results of the analysis of the spectrometer are found in Table 3.1. The dark count was found using the slope of Fig. 3.11d. The gain and read noise were found using Eq. 3.6 on Fig. 3.11f. The spread of data points at high counts in Fig. 3.11f arises because different channels of the spectrometer have different gains. Because our signal levels were low, we did not have to calibrate the individual channel gains.

The spectrometer noise creates a problem for our low light signal because the light that we collect is distributed across many channels. My average signal for the spectrometer while scanning with the STM, using 2.05 V and 20 nA, is ≈ 3000 counts per second integrated over the entire wavelength range. There are ≈ 500 channels collecting the signal giving an average of 6 counts per channel. From Eq. 3.7 and using an average signal of 6 counts per channel and the above measured noise, I produced a graph of the signal-to-noise ratio per channel versus integration time, Fig. 3.12b. This graph shows the challenge created by spreading our signal over many pixels. We see that to get a $1:1$ signal-to-noise ratio it is necessary to collect data for ≈ 1.5 s at a 20 nA set point, a large current for DNA imaging. This limits us to a maximum scan rate of 0.67 pixels/s while using the spectrometer. Unfortunately, it is not possible to set up the spectrometer CCD to bin horizontal pixels in order to reduce the noise.

The spectrometer is used in two different modes. First, it can collect a single spectrum over a period of time. Second, the spectrometer can be set to capture many spectra over a period of time to create a spectral movie. Using the second mode, the spectrometer was programmed to do spectroscopic imaging (acquisition of spectra at each point of an STM image). Spectroscopic imaging was quite limited for us because of the low signal-to-noise ratio. To create a spectroscopic image with enough signal to overcome noise, we must use the STM at very low scanning frequencies.

Chapter 4

Sample Preparation

Sample preparation for this experiment crossed many different fields, requiring ideas from chemistry, biology, and physics. Our samples were produced in various steps, as described in this chapter. The first step was to deposit thin gold films using epitaxial gold growth. The second was to label DNA with a fluorescent dye. The third was to deposit the DNA on our gold films. The fourth was to prepare the sample for imaging by attaching a weight to it.

4.1 Gold film substrates

We required three features of the substrates used in our experiments. First, they needed to be conductive to use with the STM. Second, they had to be flat enough to image DNA. Third, they needed to be semi-transparent for light to pass through and be collected by our optical equipment. Gold was used because, in thin-enough films, it could meet all three requirements and was relatively chemically inert.

Gold has a face-centred-cubic (FCC) structure, with a lattice constant of 0.408 nm (Fig. 4.1). The (111) plane of the lattice is a single close-packed hexagonal layer, with each atom 0.288 nm from its nearest neighbours in the plane [58]. The (111) plane forms a triangular structure in the FCC unit cell and leads to triangular facets on Au (111) surfaces (Fig. 4.3).

To produce conductive, flat, transparent gold films, we used epitaxial gold growth [92–95]. We decided to use the thin-film geometry of gold on mica because it can sponta-

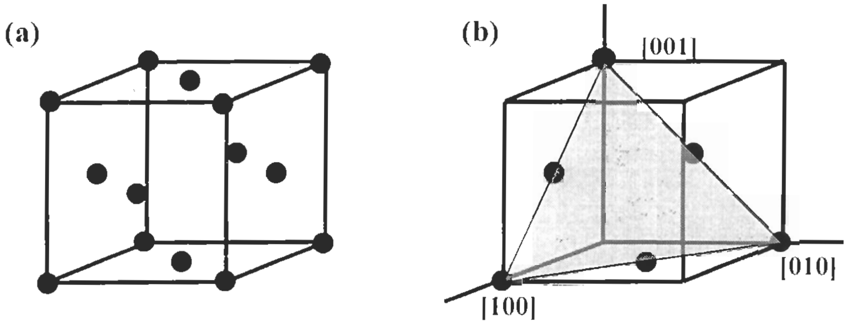

Figure 4.1: Gold crystalline structure. (a) Au crystal face-centred-cubic (FCC) unit cell. (b) Diagram showing the (111) plane of an Au crystal.

neously form (111) facets [92], and we can control the film thickness to produce conductive, transparent films.

4.1.1 Mica preparation

Mica is often used for epitaxial gold growth because its surface is mostly terminated by oxygen atoms with a lattice size (0.255–0.286 nm) close to that of the (111) plane of the gold lattice (0.288 nm) [92]. Other advantages to using mica include its low cost, ease of cutting to desired size, and ability to form a clean flat surface by cleaving before use.

Before evaporation, the mica substrate was freshly cleaved and placed into a rectangular sample holder equipped with a heater [96]. The mica was then heated to help form Au (111) facets [92, 94]. Heating produces two effects: First, it helps remove water and other contaminants that prevent well ordered crystalline growth. Second, gold atoms hitting the heated mica surface have an increased surface-diffusion constant. Their greater mobility helps gold atoms to overcome energy barriers and find their lowest energy configuration, resulting in increased Au (111) crystal growth.

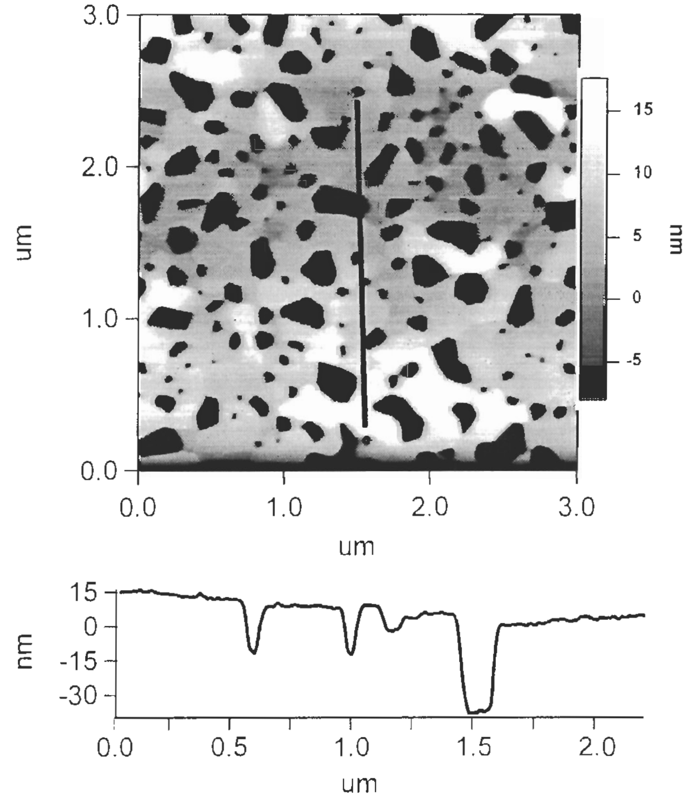

Figure 4.2: Gold film created by thermal evaporation on mica heated to 250°C, after annealing. Assuming that the dark areas are the dewetted bare mica, one can infer the film thickness is inferred to be 42 ± 3 nm.

4.1.2 Gold evaporation

The gold was evaporated in a vacuum ($\approx 10^{-6}$ Torr) on heated, freshly cleaved mica. The mica temperature and gold evaporation rate were found to be the most important parameters for producing conductive, flat, thin films.

We tried several different mica temperatures for the evaporation of gold to produce our films. At room temperature, the evaporated films were grainy and could not be used to image DNA. At high temperature (≥ 350°C), the films were not conductive because flat, separated islands would form but not connect, given the short evaporation times. We found that evaporating gold on mica heated to 250°C produced the flattest results for conductive

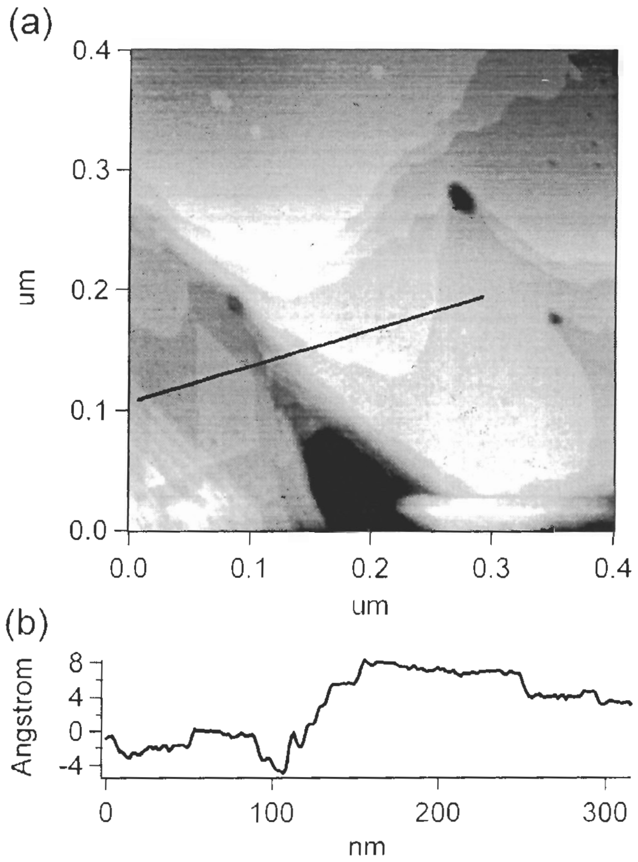

Figure 4.3: Close-up of gold islands showing triangular faceting. This indicates a (111) gold surface.

gold films that were thin enough to be semi-transparent. As seen in Fig. 4.2, flat gold islands are still created on the mica heated to 250°C, but the lower temperature allows for better gold wetting, seeding more islands than with mica heated to 350°C. The increase in islands allows for more connections during the short evaporation times, producing conductive gold films.

To produce a flat surface, we also needed to control the evaporation rate. Slow (≤ 0.4 nm/s) and fast evaporation rates (≥ 1.0 nm/s) produced gold films without the desired faceting, even after further annealing (Sec. 4.1.3). The optimal evaporation rate for our experimental setup was ≈ 0.6 nm/s–0.7 nm/s, producing films that showed faceting and became very flat with further annealing (Fig. 4.3).

During evaporation, the gold film thickness was monitored using a quartz-crystal sensor [97] and the evaporation was stopped when the monitor read $\approx$16 nm. We found a reading of $\approx$ 16 nm from the quartz-crystal sensor was the onset of conductivity for our gold films. Though the quartz-crystal sensor allowed us to monitor film growth it was not an accurate reading of film thickness. For an accurate reading of film thickness, we measured the sample transmission coefficient (Fig. 4.4) and modeled our sample using three layers (air, mica, gold) [98] to find the thickness. The average transmission coefficient of our samples was $\approx 15\%$ at $\lambda = 632$ nm. The model gave us a transmission coefficient,

$$T = \frac{n_0}{n_2}\frac{[(1+g_1)^2+h_1^2][(1+g_2)^2+h_2^2]}{e^{2\alpha_1}+(g_1^2+h_1^2)(g_2^2+h_2^2)e^{-2\alpha_1}+2(g_1g_2-h_1h_2)\cos 2\gamma_1+2(g_1h_2+g_2h_1)\sin 2\alpha_1}. \tag{4.1}$$

with

$$\begin{aligned} \alpha_1 &= 2\pi k_1 d_1/\lambda, & g_1 &= \tfrac{n_1^2-n_0^2+k_1^2}{(n_0+n_1)^2+k_1^2}, & h_1 &= \frac{-2n_0k_1}{(n_0+n_1)^2+k_1^2}, \\ \gamma_1 &= 2\pi n_1 d_1/\lambda, & g_2 &= \tfrac{n_2^2-n_1^2-k_1^2}{(n_2+n_1)^2+k_1^2}, & h_2 &= \frac{2n_2k_1}{(n_2+n_1)^2+k_1^2}, \end{aligned}$$

and λ (632 nm) the wavelength used to measure the transmission coefficient; n_0, n_1 and n_2 are the refractive index of mica (1.561), gold (0.16) at λ, and air respectively; k_1 is the extinction coefficient of gold (3.15) at λ; and d_1 is the thickness of the gold film. We then added a term to take in the effect of the mica-air interface. Since the mica in our samples was $\approx 100\mu$m thick and is a weakly absorbing material, with absorption coefficient of $\approx 10^{-5}$ [99], the term due to the mica-air interface can be approximated as being from the interface on the gold side. Then for the mica-air interface

$$T' = \frac{4n_0n_2}{(n_0+n_2)^2} \approx 0.95. \tag{4.2}$$

From our model, we estimate our gold film thickness to be ≈ 38 nm. This estimate is confirmed by the difference in height between the holes and the gold islands using an AFM, as seen in the height profile of Fig. 4.2.

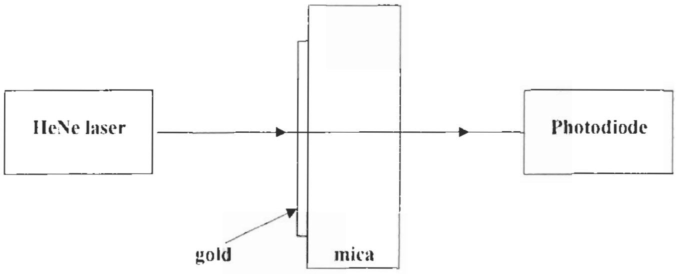

Figure 4.4: Setup for measuring transmission coefficient T.

4.1.3 Film annealing

Annealing was necessary in producing atomically flat gold films. Annealing gives energy to the gold atoms, allowing them to overcome barriers and find their lowest energy configuration, resulting in a better Au (111) surface [30]. It also produces larger facets because it allows the boundaries of islands to diffuse, merging separate islands.

We chose to flame anneal the gold films using a hand torch [100] that we quickly passed over the film. Flame annealing was done in a dark room, where I heated the gold film until it gave off a reddish-orange glow. It was necessary to be cautious when flame annealing to prevent over-heating the gold film. Because liquid gold does not wet mica, actually melting the gold would cause it to bead up, leading to a bumpier surface after refreezing. After proper annealing, the film surface roughness regularly decreased from $\approx$ 20 nm to $\approx$ 10 nm for a 500 μm^2 area.

4.2 Fluorescent-labeled DNA

Fluorescent dye production is an ever growing industry producing new dyes to help in the observation of biological phenomena. Each dye group has specific properties that make them the appropriate choice for different situations. In this section, I discuss dimeric cyanine nucleic acid stains and of these stains specifically TOTO-3 [77], the dye we used to stain the DNA. I also detail the procedures used to stain the DNA for fluorescent spectroscopy.

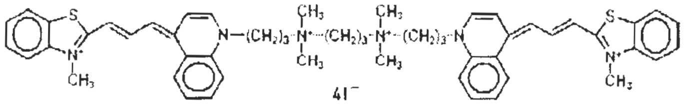

Figure 4.5: Chemical structure of TOTO-3.

4.2.1 Dimeric cyanine nucleic acid stain

Dimeric cyanine nucleic acid stains are a family of bis-intercalating dyes used for the analysis of DNA. In this family, different dyes span the entire visible range of light for emission and excitation. The features that make these stains well suited for DNA analysis are their strong affinity for DNA, fluorescent enhancement upon binding, and high quantum efficiency.

A dimeric cyanine is made up of a linker connecting two chromophores together, as seen in Fig. 4.5. A dymeric cyanine binds to DNA by bis-intercalation; both chromophores are inserted into the DNA between base pairs. The two inserted chromophores are separated by two base pairs, the length of the linker that fits into the minor groove of the DNA, as seen in Fig. 4.6. To allow the chromophores to fit between base pairs, the DNA is forced to unwind by 60 degrees. Once inside the DNA, four positive charges along the side chain help to form a very stable complex with the negatively charged DNA. Because dymeric cyanine dyes are dimers with two intercalating chromophores they have high DNA binding affinity, greater by several order of magnitude than a monomer of the same cyanine. Dymeric cyanine dyes have also been engineered to have a high fluorescent enhancement upon binding to DNA. The dye has a low fluorescence emission before binding to DNA because the molecule can rotate around the cyanine-methine bond to release energy. After insertion into the DNA, the dye can no longer rotate and relaxation is by fluorescent emission. These dyes also have a high quantum yield.

The main reason we chose to use dimeric cyanine nucleic acid stains was that the dye would be inside the DNA, producing a near-1-nm gap between it and the substrate, as well as between it and the tip. The gaps prevent full quenching of the emission, as discussed in Sec. 2.3.4. Out of the different dyes in this family, we needed a dye that was excited by a relatively long wavelength of light, or equivalently by low-energy electrons. As discussed

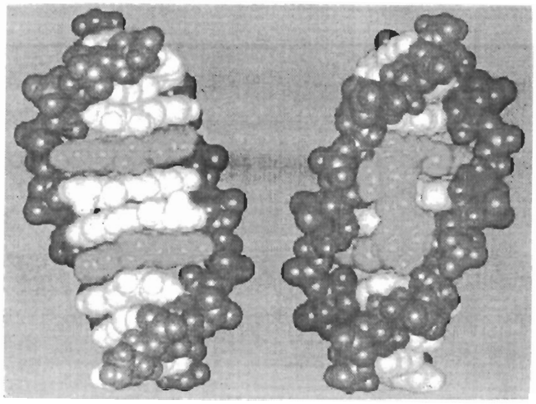

Figure 4.6: TOTO-3 intercalating DNA. The DNA is in blue with the backbone dark blue and the base pairs light blue. TOTO-3 is in red and shows how the chromophores would enter into the DNA. Reprinted with permission from HP Spielmann, D Wemmer,and JP Jacobsen, "Solution structure of a DNA complex with the fluorescent bis-intercalator TOTO determined by NMR spectroscopy", Biochemistry **34** (1995) 8542–8553. Copyright 1995 American Chemical Society.

in Sec. 5.1.3, imaging gold in air with an STM can damage the surface when using a bias greater than ≈ 2.1 V. To prevent this form of damage, we used TOTO-3, a far-red-absorbing fluorophore with an excitation maximum at 642 nm, equivalent to a 1.93 V bias.

4.2.2 Staining procedures

My sample-preparation protocol for attaching TOTO-3 to the λ-DNA was formulated after several cycles of trial and error. The TOTO-3 sample was aliquoted from the stock solution, 200μL of 1 mM sample in dimethyl sulphoxide (DMSO), into 10 samples of 100μM each in DMSO. Since TOTO-3 is unstable in an aqueous solution, I mixed it with the buffer just before labeling the DNA sample with the fluorophore. When we were ready to label the DNA, the TOTO-3 was diluted in buffer and aliquoted into a pipet. The DNA was then added to the same pipet, to produce the desired concentration, and left in the dark, at room temperature, for one hour. The labeled DNA was then ready to use.

We tested the usual light emission (by optical excitation) of the fluorophore attached to the λ-DNA in 4 mM Hepes buffer with 10 mM NaCl and 2 mM $MgCl_2$, by making various solutions with different base-pair-to-dye ratios and DNA concentrations. Each solution was

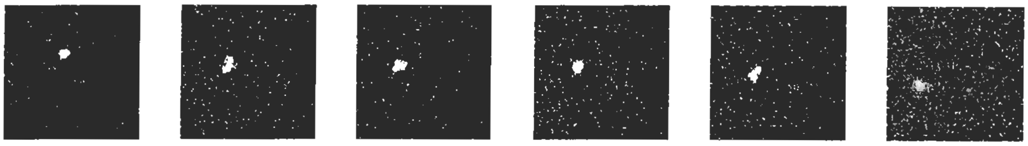

Figure 4.7: λ–DNA tagged with TOTO–3 in solution. Series of images captured showing DNA moving by diffusion. Images are 100 μm x 100 μm with 80 ms between frames.

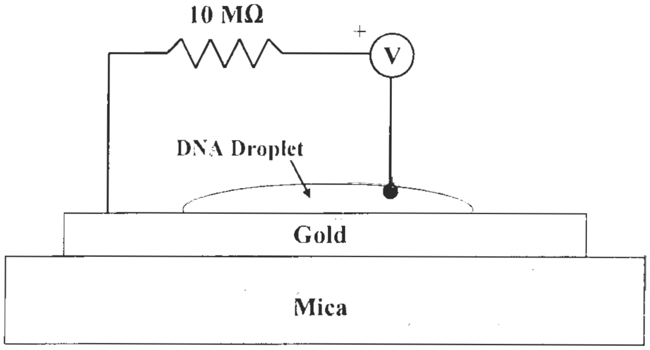

Figure 4.8: Diagram of the circuit used for DNA deposition.

then placed into a chamber to view. We found that using a 10 : 1 ratio with 4 ng/μL DNA concentration worked best for viewing the labeled DNA in solution using a fluorescent microscope with a Texas Red filter set. We used this ratio and concentration for our attempts to image the dye in DNA by STM. With this optimal ratio and concentration, we took a series of images showing the DNA moving by diffusion in solution (Fig. 4.7).

4.3 DNA deposition on gold

DNA needs to be strongly attached for imaging with an STM. There are many different methods of attaching DNA to gold, as discussed in Sec. 2.3.1. We chose to use electrostatic deposition because the process is simple and has produced good results [51, 52].

To begin the process of DNA deposition, we first cleaned the gold films using a UV-

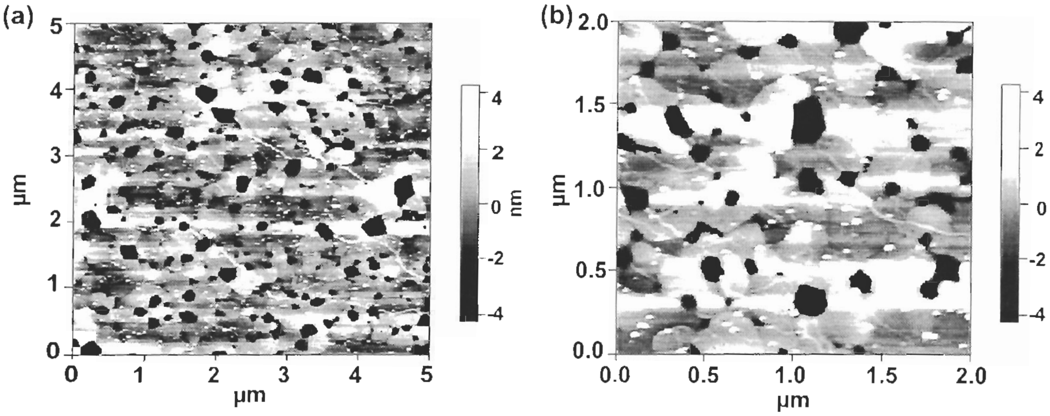

Figure 4.9: DNA deposited on gold, as imaged by a tapping-mode AFM.

ozone cleaner [102] for 10 minutes to remove any contaminants. After the cleaning, 10μL of labeled DNA in a 4 mM Hepes buffer with 10 mM NaCl and 2 mM $MgCl_2$ was deposited on the gold and left for 10 minutes. The gold was then held at a potential of 50 mV relative to the solution using the setup shown in Fig. 4.8 and left for 10 minutes. After the 20 min deposition, the gold was rinsed by dipping it in distilled, deionized water [103] three times to remove salts from the surface. The concentration of the DNA attached was evaluated using a tapping mode AFM (Fig. 4.9). If there was enough DNA on the gold, it was put on the STM and studied with the positive bias connected to the gold to help stabilize the sample.

We found that it was important to have the $MgCl_2$ in the buffer because without it there was less DNA attachment to both gold for our experiment and to mica for checking DNA concentrations [104]. The UV-ozone cleaning also helped in attaching the DNA to gold. Less DNA was deposited onto samples that were freshly flame annealed but not UV-ozone treated than onto treated samples. This may be due to a layer of gold oxide formed on the surface by the UV-ozone cleaning [105] which can also change the gold surface from hydrophobic to hydrophilic [106].

4.4 Sample assembly

During the stick-slip fine approach, vibrations are transfered to the sample. For our samples, the vibrations made it hard to obtain feedback without crashing the tip into the surface. Because of this, all thin-film samples needed to be attached to a small weight in order to make a successful approach.

To solve this problem, I placed a weight on top of the sample to stabilize it, except when the optics were set for collecting light. With the objective above the sample and only about 100μm from the surface, it was not practical to place a weight between the objective and the substrate. My solution was to glue, using super glue [107], a washer (inside diameter of 10mm and an outside diameter of 14mm) to the downward facing side of the sample (Fig. 3.3). This stabilized the gold during the stick-slip approach and allowed the weight to hang down outside of the tube scanner and out of the way of the optics.

Chapter 5

Results

In this project, we set out to study the effectiveness of an STM for imaging fluorescent-labeled biological specimens. To accomplish this, we first set up our STM for light emission recording and tested its capabilities by characterizing plasmon emissions from gold. Second, we studied the topography and light emission from DNA attached to gold. Third, we extended the capabilities of our atmospheric STM using an argon atmosphere instead of air. We then tested whether the results observed in air were affected by the presence of oxygen or water vapour. I discuss the results of these steps in this chapter.

5.1 Gold plasmon characterization

Our STM can record light intensity and spectral data produced by tunneling current. To test this, we characterized gold plasmon emissions excited by tunneling current. The results of these tests confirm that our STM is collecting light produced by tunneling current exciting localized plasmon resonances and allow us to estimate the light collection efficiency. The results in this section were obtained while working with an undergraduate summer student, Otto Verhage [72].

5.1.1 Tunneling current

Gold plasmon emission from an STM is a result of inelastic tunneling events exciting a localized surface plasmon. By increasing the tunneling current, one expects an increase in

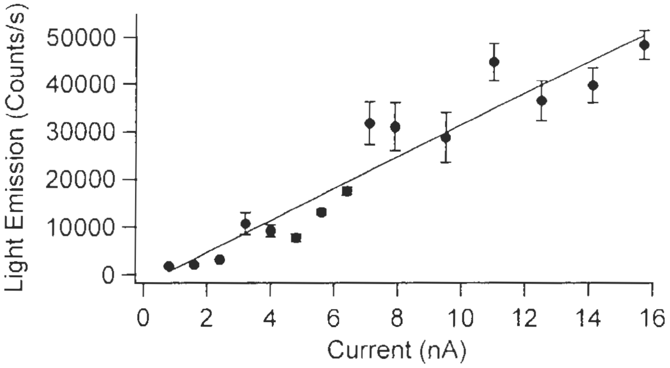

Figure 5.1: Plasmon light emission versus tunneling current at 1.6 V bias. Solid line is the linear fit to our data.

plasmon emission intensity. We recorded the light intensity while varying tunneling current to verify the light detected is a result of tunneling current. This result confirmed that the light emission was directly related to the tunneling current and allowed us to estimate our light-collection efficiency.

We first wanted to confirm that the light coming from the sample was caused by tunneling electrons. Using a Pt-Ir tip and a gold substrate, we recorded the intensity of the photon counts as a function of current (Fig. 5.1) with a stationary tip, using our avalanche photodiode (APD). We found that the light intensity increased linearly with respect to the current set point of the STM, which confirms that the light being produced was from electron tunneling. The variations from a linear relationship seen in Fig. 5.1 are likely caused by fluctuations in the inelastic tunneling contribution to the overall tunneling current [108] and variations in the tunneling barrier due to contaminants such as water [109].

With our setup, we detect only a fraction of the photons emitted by excited plasmons. It is useful to study the efficiency of the setup to see where the losses in signal are and to confirm that our emission rate is consistent with previous results. We considered the following points summarized in Table 5.1:

1. Our STM design, discussed in Chapter 3, has the tunneling tip below the sample and the capturing optics above. Because of the poor transmittivity of conducting gold (Sec. 4.1.2), the fraction of light transmitted is ≈ 0.15.

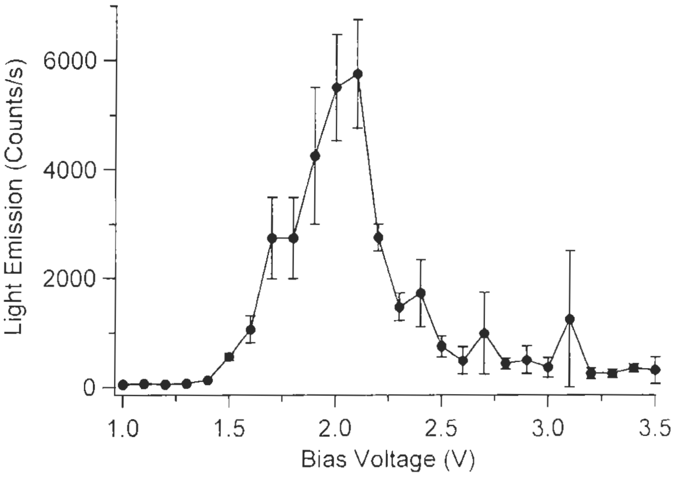

Figure 5.2: Plasmon light emission versus STM bias.

2. The microscope objective captures only a cone of the emitted light from the surface plasmons excitation. The NA of our objective is 0.82 when used in air, which corresponds to a fraction of light collected by the objective of ≈ 0.22.

3. Our collimator has a numerical aperture (NA = 0.25) that is slightly larger than our optical fibre numerical aperture (NA = 0.22). This causes the light being focused on to the fibre to have a larger cone angle than the optical fibre can receive. I estimate the loss from mismatched NAs using the square of the ratio of the NAs [110]. The fraction of light that couples into the optical fibre is then ≈ 0.77.

4. There is also a loss created by poor focusing alignment. The focusing loss is caused by the inexact lateral location of tunneling apex from the Pt-Ir cut tips which are large ($\sim 80\mu$m) and irregular, as well as finding the vertical plane of the substrate is difficult because we cannot see through the substrate to view the tip when a tunneling substrate is in place. The lateral alignment can be improved by translating the optics laterally while observing the light emission intensity, though movement often causes tip crashes. The vertical alignment can be improved in the same way but the STM is even more sensitive to this movement, causing the tip to contact the surface. The

Effect	**Efficiency**	
	APD	Spectrometer
gold transmittivity	0.25	
microscope objective	0.22	
NA mismatch	0.77	
fibre optic transmission	0.8	
focusing efficiency	0.23	
detector efficiency	0.9	0.23
Total efficiency	0.007	0.002

Table 5.1: Efficiency of the optics used to detect light emission

STM is likely more sensitive to vertical movement because the objective can easily contact the substrate if it is brought much closer than the optimal distance for light collection. These focusing challenges made us look for a focus that allows us to collect light for imaging but prevent us from making many changes which could lead to a bad tip. To get a rough estimate of the focusing loss, we use a ratio of the maximum light emission measured versus the typical light emission measured to get an estimated efficiency of ≈ 0.23.

5. Each detector has an efficiency of detecting the light. The APD efficiency is directly from the quantum efficiency of the detector at the wavelength of interest and is ≈ 0.9. The spectrometer's efficiency includes both its quantum efficiency and that of its spectrometer grating. Its overall efficiency is ≈ 0.23.

The estimates of the various losses are collected in Table 5.1. They give an overall optical efficiency of 0.007 when using the APD and 0.002 when using the QE65000 spectrometer [91]. This means that using the APD, we detect approximately 1 of every 170 photons emitted and, using the spectrometer, approximately 1 of every 500.

Using our estimated efficiency and our measurement of light intensity versus tunneling current, we can compare our results to previously published theoretical and experimental estimates of the efficiency of the plasmon emission process. From the linear fit of Fig. 5.1, we find that our experimental efficiency for plasmon-induced light emission is ≈ 5.0 x

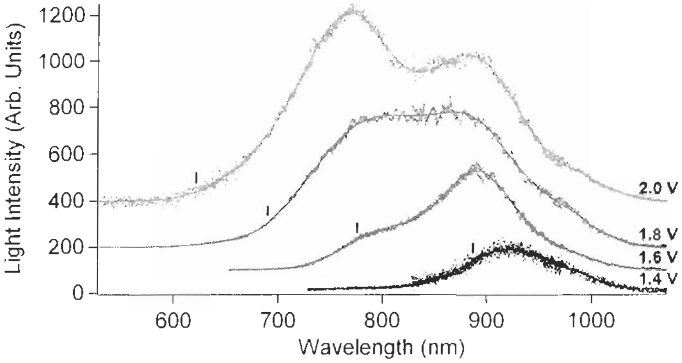

Figure 5.3: Spectra for the light emission using different bias voltages. The vertical lines represent the cut-off wavelength (energy) for the bias voltage used.

10^{-7} photons per electron. Using an optical efficiency of 0.007 (APD case), I calculate our efficiency of plasmon-induced light emission to be 0.7 x 10^{-4} photons per electron. This is close to the value of 1 x 10^{-4} photons per electron published previously [66, 67].

5.1.2 Bias voltage

The STM bias voltage setting has an effect on the plasmon emission excited by tunneling electrons. The bias voltage affects the intensity of the plasmon efficiency and the spectral emission by controlling the energy of the electrons used to excite localized surface plasmon.

We measured the effect of the bias voltage settings on light emission intensity in air. With a stationary tunneling tip, we took many measurements of plasmon emission intensity while varying the bias voltage. Our experiment shows that, in air, the peak emission rate is $\approx 2.1V$ with a stationary tip, as shown in Fig. 5.2, which is similar to previous results reported [111]. Below in Sec. 5.3 , we show that this peak value arises because of damage by our in-air STM on the gold substrate at high bias voltages. We also studied plasmon emission at negative bias voltage and found that there was little emission at these bias voltages, an observation already made by previous experiments [112]. The loss of light emission for negative sample bias voltage is not understood.

Using a 1/4 m spectrograph [113] equipped with a 300 lines/mm blazed grating, we studied the spectra of the light emission for different STM bias voltages while scanning,

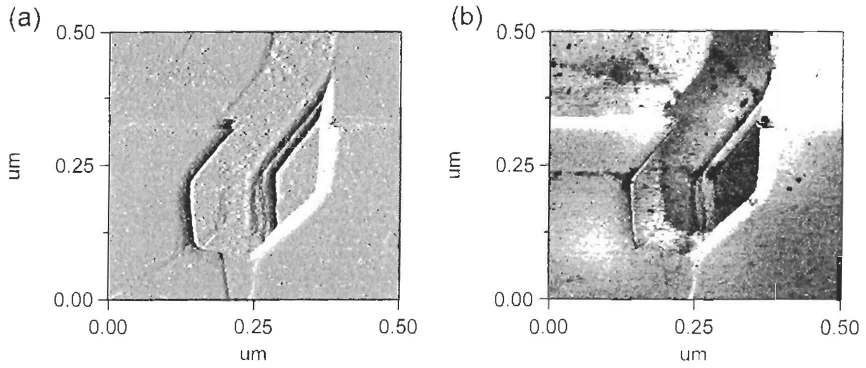

Figure 5.4: Simultaneous topographic and light-emission image of gold at 2.0 V and 50 nA. (a) Topographic image. (b) Light-emission image.

(Fig. 5.3). Particularly at low bias voltages (1.4–1.6 V), we notice a surprising feature: photons of higher energy (shorter wavelength) than that of the tunneling electrons are produced. This apparent violation of energy conservation was first discovered by Pechou *et al.* [114] and later concluded to be due to spreading of the fermi level caused by substrate heating [115]. In other words, the energy of the emitted photons derives, in part, from contributions by "background" tunneling electrons. The reason that this effect has not been seen at high bias voltages is not well understood. We fit the spectra for each bias voltage to a gaussian profile to study the peak structure of the emission. The 1.4 V spectrum was fit with two peaks, the 1.6 V and 1.8 V spectra with three peaks and the 2.0 V spectrum with four peaks. These multiple peaks are caused by the radiative enhancement from the resonant excitation of localized surface plasmons [116] discussed in Sec. 2.3.3. The position of the longest wavelength peak ($\approx$ 970–980 nm) is constant with each bias voltage, but the shorter wavelength peaks are not present at low bias voltages resulting in weaker, red-shifted peaks or missing peaks for low-bias spectra. The conclusion is that the peaks in the emission spectra are caused by the tip geometry and not the bias voltage, although a high-enough bias voltage is needed to observe each peak.

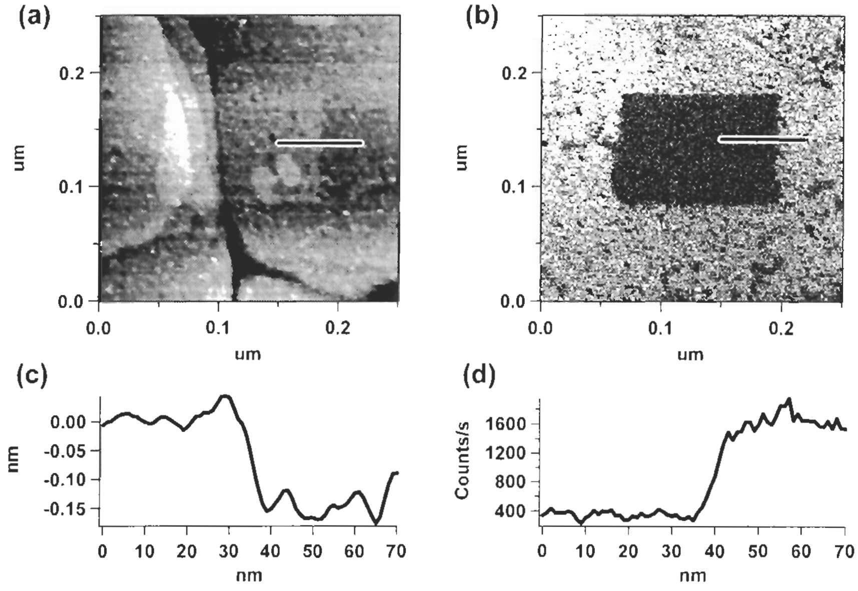

Figure 5.5: A 0.25 x 0.25 μm^2 image enclosing a 0.10 x 0.10 μm^2 area previously scanned at 2.1 V and 4.5 nA. (a) Topographic image shows a square area raised by 0.15 nm that is caused by damage to gold using an STM in air with a high bias voltage (2.1 V). (b) Simultaneously acquired light-emission image has a square dark region, where damaged gold prevents light emission.

5.1.3 Plasmon emission and topography

One can record the simultaneous topographic and photon intensity image while scanning in constant-current mode. The two images reveal information about the surface because photon emission depends on local surface properties, as discussed in Sec. 2.3.3. This method could be used to probe materials in new ways, but, as of yet, changes in photon emission caused by surface features are not fully understood [117]. One obvious mechanism is that the finite bandwidth of the STM feedback loop leads to imperfect tracking. The height variation in the STM tip would then lead to variation in photon-emission rates. Another mechanism is a mismatch in tunneling and localized surface plasmon direction at defects, discussed in Sec. 2.3.3.

We created images of light emission and topography simultaneously while scanning with the STM (Fig. 5.4). The images show that the light emission corresponds to surface

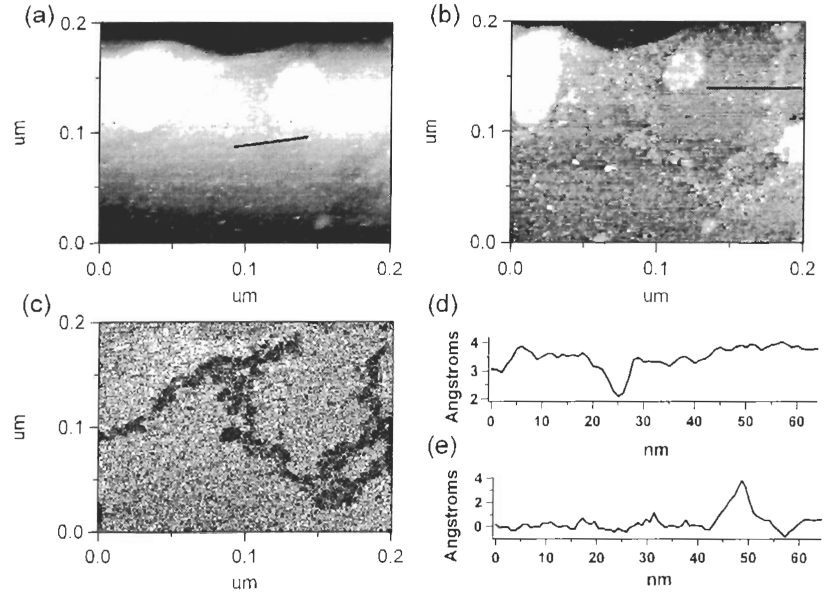

Figure 5.6: Images of DNA showing the change in topography with different tunneling conditions and plasmon emission quenching by DNA. (a) Topographical image with a bias voltage of 0.75 V and 1 nA. (b) Topographical image of DNA with a bias voltage of 2.05 V and 2.5 nA. (c) Light emission taken simultaneously with (b). (d) Height profile for DNA in (a). (e) Height profile for DNA in (b).

features found on the topography.

While using an STM to image gold in air, one can damage the gold surface by using bias voltages greater than ≈ 2.1 V [55, 111, 114]. The large electric fields move around gold atoms, usually leading to a raised section and to areas where plasmon light emission is no longer possible. I observed this by scanning a square area on our gold sample using a bias voltage of 2.1 V and 4.5 nA. After the 2.1 V scan, I expanded the range to observe the change caused by the previous scan. Our results show a 0.1 nm raised area in the topography image and a corresponding loss in plasmon emission from the 2.1 V scan (Fig. 5.5). The loss of emission on a gold surface is theorized to be caused by the molecules absorbed on to the surface that create the bump. These absorbed molecules have not been well studied and are hypothesized to be carbon contaminants or gold particles redistributed. To explain the

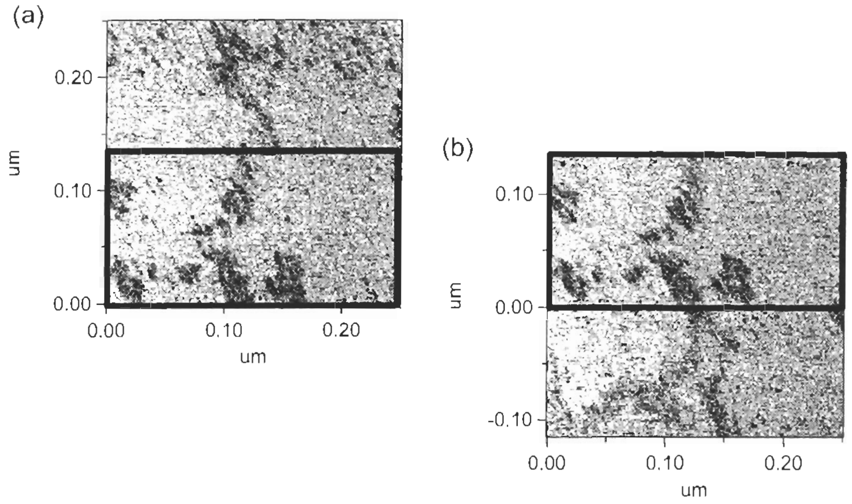

Figure 5.7: Light-emission images of DNA become darker in successive scans. (a) Light-emission image of DNA on gold after the second scan. (b) Light-emission image taken after translating in the negative y direction. The DNA that has been scanned more than once is much darker than the DNA that has been scanned the first time.

loss in emission that would be caused by contaminants, Sivel *et al.* note that the transition probability depends on the local density of states (LDOS) of the tip and the substrate [111], discussed in more detail below (Sec. 6.1.1). Loss in emission can also be caused by the increase in tunneling distance when the contaminants are imaged as a protrusion on the surface [118], discussed in more detail below (Sec. 6.1.2). Another theory for the loss in light-emission involves gold rearrangement, Pechou *et al.* suggest that the disorganized atoms of gold will produce a highly perturbed electrostatic surface potential that would prevent localized surface plasmons from forming [120], discussed in more detail below (Sec. 6.1.3).

5.2 Imaging DNA

Our main interest in this project was to find new ways of imaging biological samples. We decided to use DNA as our biological molecule because it is a well-studied molecule with many choices of fluorescent dyes that attach to DNA in different ways.

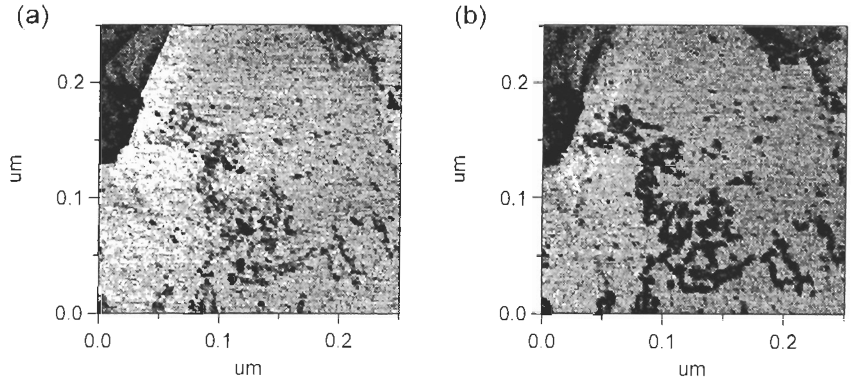

Figure 5.8: Light emission images of DNA without fluorophores attached become darker in successive scans. (a) First scan. (b) Second scan over the same area.

5.2.1 Topography

Imaging DNA topography using an STM has produced varying results in the past, as discussed in Sec. 2.3.2. I also found results that varied depending on the sample conditions and STM settings. I was able to produce contrast inversion between images with settings optimized for topography and settings optimized for light emission. The topographical images of DNA produced using a 0.25 to 1.0 V bias and current set points between 25 pA to 5 nA at a line scan rate of 1 Hz were always seen as inverted-contrast images of DNA. The DNA in these images have an apparent height between -0.05 to -0.15 nm (Fig. 5.6(a) and (d)). When imaging DNA topography using 1.8 V to 2.2 V bias and current set points between 1 nA to 10 nA at a line scan rate of 0.125 to 0.5 Hz, settings necessary to produce a light-emission image, I found that the DNA had positive contrast. The DNA in these images have a height between 0.1 to 0.4 nm (Fig. 5.6(b) and (e)). Contrast inversion when changing the settings of the STM is expected. The contrast inversion that we saw is likely caused by the change in bias voltage as the set point current had an overlapping range for both contrast. There are three theories that could explain this phenomena: LDOS changes, tunneling-gap changes, or resonant tunneling through the DNA. These are discussed in Sec. 6.2.

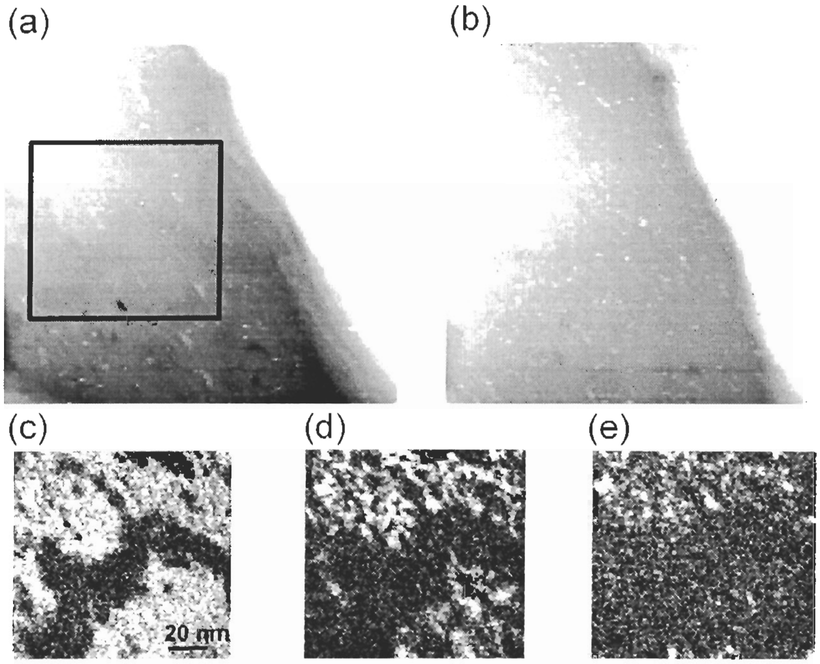

Figure 5.9: Damage to DNA done by tunneling current. (a) 250 x 250 nm^2 topographic image of DNA on gold before light emission imaging. Square box shows where the light emission images were taken. (b) 250 x 250 nm^2 topographic image of the same area after the light emission scans. It is no longer possible to see the DNA on a topographic image. (c-e) Successive 125 x 125 nm^2 light emission images of the DNA in image a) using 2 V bias and 4 nA tunneling current. The image loses emission over time.

5.2.2 Light emission

In an attempt to see fluorophores attached to DNA, we studied the light emission created by tunneling electrons from the STM on labeled DNA. To excite the fluorophores in the DNA, recall that the TOTO-3 absorption maximum is at 642 nm (1.93 eV). We thus needed to use a high bias voltage (≈ 2.0 V) for an air STM. In this section, I discuss the results of scanning DNA with and without fluorophores attached, using high bias voltages.

When we scanned DNA using a bias ≥ 1.4 V and current setpoints between 1–4 nA, allowing us to record the light emission, we saw the DNA as a dark area surrounded by

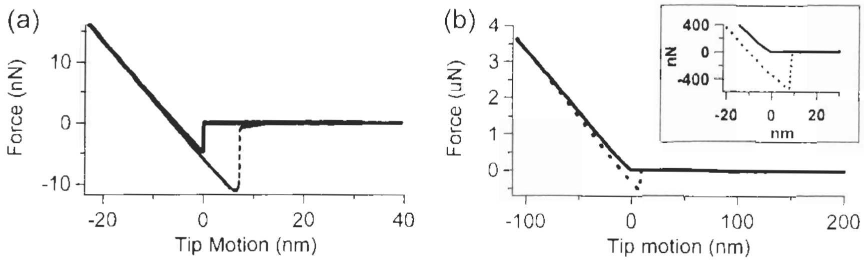

Figure 5.10: AFM cantilever force-distance curves. The solid line represent the approach to the substrate and the dotted line is the retraction. (a) Regular force-distance curve for an AFM using a 0.8 N/m cantilever. (b) Force-distance curve with a 40 N/m cantilever that was used in our experiment. Inset shows that there is not a visible "jump-to-contact".

plasmon emissions from the gold surface (Fig. 5.6(c)). It is important to note that DNA shows up as a dark area in plasmon emission well below the emission cut-off voltage for a stationary tip and a scanning tip in air. We also found this to be the case for DNA with and without attached fluorescent markers. There are many theories that could be used to explain this result and I discuss them in more detail in Section 6.2.

In an attempt to see the effects of attached fluorescent markers, I looked for a change in the amount of light coming from the dark DNA area, expecting bleaching of the fluorophore with subsequent scans. I did see a general darkening of the DNA from the first to second scan, as seen in Fig. 5.7. After seeing this, I wanted to confirm that the change was because of the fluorophores and not the DNA by imaging DNA without fluorophores attached. The results for multiple scans of DNA without attached fluorophores are very similar (Fig. 5.8). Thus, light emission from areas covered by DNA decreases whether the DNA is labeled with fluorophores or not, and the dark area spreads from the first scan to the second scan.

I then studied the spreading phenomena over multiple scans and observed that the plasmon emission quenching area created by the DNA always spreads from the first image to the second image but usually changes little after this. On occasion, the quenched area keeps spreading with subsequent scans. This further spreading appeared when there were multiple strands of DNA clumped together in an image. Figure 5.9 shows an example of the plasmon emission quenching continuing to spread with multiple scans with "before" and "after" topography images. These images suggest that the DNA itself spreads out across the

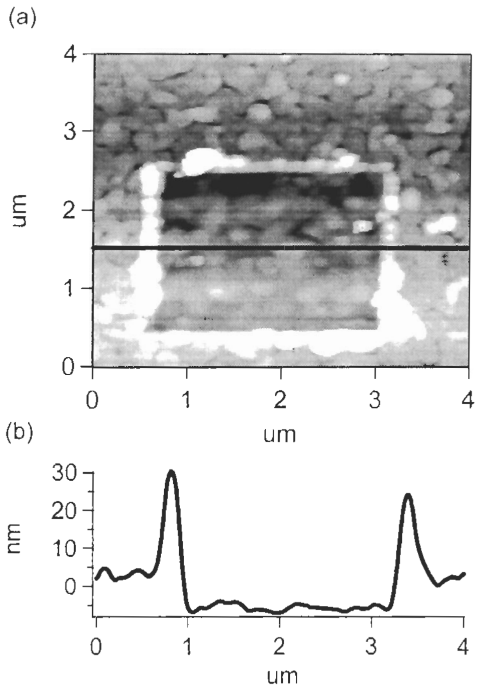

Figure 5.11: (a) Tapping-mode AFM image of a DNA film on gold after scanning a 2 x 2 um^2 region in contact mode. The lower central area shows the change to the DNA when an AFM tip sweeps the DNA to the side of the imaging area. (b) The height trace is set to the width of the feature so it averages the height across the entire feature.

surface. The before and after topography images reveal that after the spreading, the DNA is no longer visible on a topography image. Also, there is no raised area on the "after" topography image, indicating that the scans have not damaged the gold surface. We propose that the spreading is caused by damage to the DNA. I discuss a few possible mechanisms to explain the damage in Section 6.3.

5.2.3 AFM of STM scanned DNA

To better understand what happens to the DNA when scanned with an STM, we tried to look at the region scanned by an STM using an AFM. At first, we tried to do this using separate STM and AFM instruments. It proved to be very hard to locate the region scanned

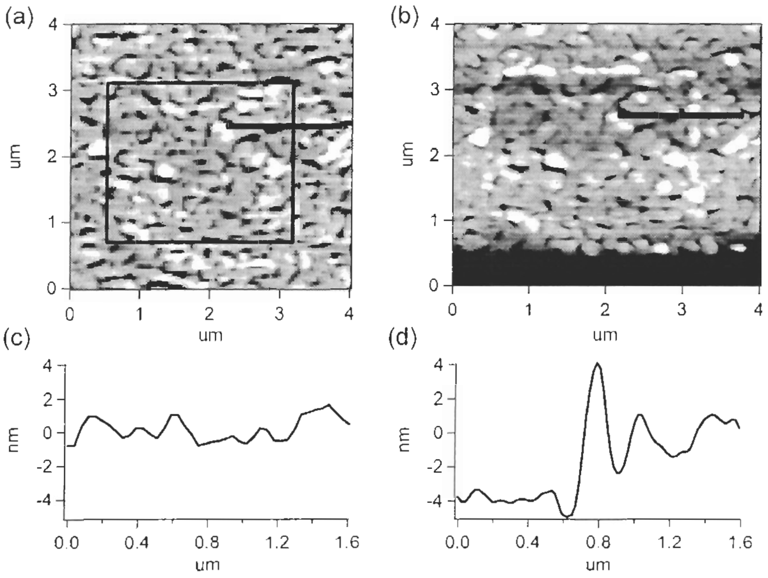

Figure 5.12: Images showing the changes made to a DNA film using an STM. (a) Tapping-mode AFM image of a DNA film before scanning with an STM. The square box is approximately where the STM scanned. (b) Tapping-mode AFM image of a DNA film after scanning with an STM. (c) Line profile showing the height features of the film before an STM scan. The white line on image (a) represents the location of the line profile. (d) Line profile showing the height features of the film after an STM scan. The white line on image (b) represents the location of the line profile.

with an STM after transferring the sample to an AFM. We then succeeded in creating this image by using the same instrument for both the STM and AFM scans[1]. As Fig. 5.10(a) shows, a floppy cantilever is subject to a "jump-to-contact" instability that prevents holding the tip at the proper height needed for STM tunneling [122]. A stiffer tip (Fig. 5.10(b)) does not show this instability. We then used the same cantilevers for a regular AFM scan in tapping-mode to image the area scanned while tunneling.

Regular conductive AFM tips are not commonly used for STM measurements because they are too flexible and bend until they contact the surface, or "jump to contact", when

---

[1] Because of the irregular shape of the Pt-Ir tips and the need to look through the semi-transparent gold to see the tip location, I could estimate the actual position where tunneling occurred to an accuracy of only $\pm 40 \mu m$. It was then necessary to find a 1 x 1 μm^2 target within a 80 x 80 μm^2 area. I made many STM scans close together for each attempt, but could not see any effect caused by the scans in our larger AFM scan.

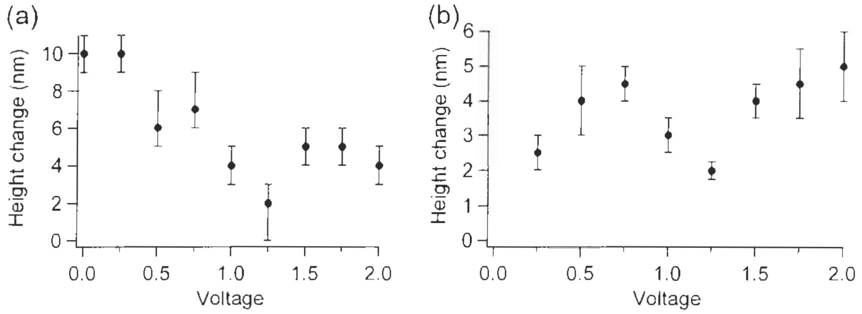

Figure 5.13: Height change vs. tip-sample bias voltage created by STM scans of a DNA film. (a) These scans were done with a constant-current set point, which causes the tip-sample height to decrease with decreasing bias voltage. The depression height at 0 V represents the depression created by a contact-mode AFM scan. (b) These scans were done with a constant tip-sample height, achieved by changing the current set point and scan speed for each bias voltage.

they are brought to within tunneling distance (Fig. 5.10(a)). When an AFM tip is brought toward a sample, the tip is attracted first by long-range van der Waals adhesion causing the cantilever to bend. Van der Waals interaction energy give a $1/r^2$ dependence on distance which causes the strength of the force to increase quickly as the tip is brought closer to the substrate [121]. This attraction is opposed by the elastic restoring force of the cantilever.

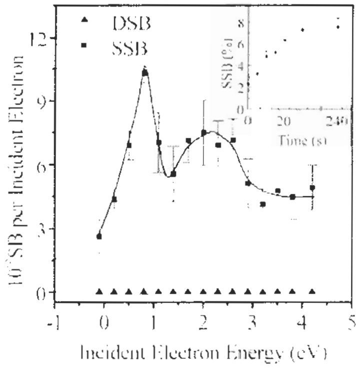

Figure 5.14: Quantum yield of DNA singe-strand breaks and double-strand breaks vs. incident electron energy. Reprinted figure with the permission of F Martin, P Burrow, Z Cai, P Cloutier, D Hunting, and L Sanche, Phys. Rev. Lett. **93**, 068101 (2004). Copyright 2004 by the American Physical Society.

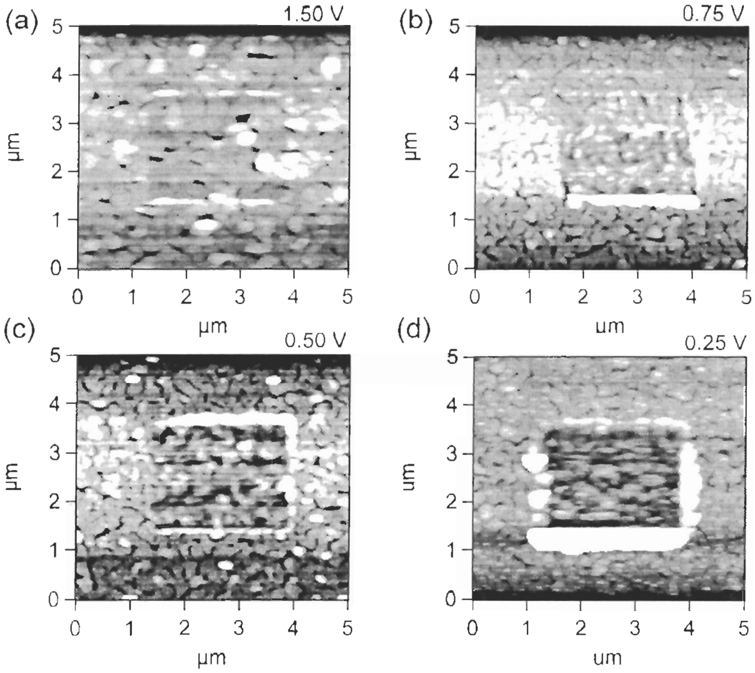

Figure 5.15: Tapping-mode AFM images showing how the decreased height at low tip-sample bias voltages leads to more DNA swept to the side by our STM scan. Only the bias voltage is changed for each of the four scans (a) STM scan using a 1.5 V tip-sample bias. (b) STM scan using a 0.75 V tip-sample bias. (c) STM scan using a 0.5 V tip-sample bias. (d) STM scan using a 0.25 V tip-sample bias.

As the tip approaches the surface, there is a distance where the force gradient of the van der Waals adhesion equals the elastic constant of the cantilever. When the tip is brought closer than the equilibrium distance, the cantilever becomes unstable and jumps to contact. Once the tip is in contact with the surface, the bending is reduced as the cantilever is lowered further until the it reaches tip-contact zero force point (no bend). As the cantilever is brought closer to the substrate than the tip-contact zero force point, it bends with a positive force. When the cantilever is raised from the surface, the tip detaches when (again) the attractive-forces gradient equals the spring constant of the cantilever [122]. The hysteresis in force seen in Fig. 5.10(a) is caused by water layers on both the tip and the surface that create capillary adhesion. To remove the "jump-to-contact" instability, we chose cantilevers with 40 N/m spring constants, which is stronger than the maximum attractive force gradient on

Scan	Voltage	current (nA)	scan speed (Hz)
1	0.25	0.4	0.25
2	0.50	0.8	0.50
3	0.75	1.2	0.75
4	1.00	1.6	1.00
5	1.25	2.0	1.25
6	1.50	2.4	1.50
7	1.75	2.8	1.75
8	2.00	3.2	2.00

Table 5.2: Settings for our constant-height STM DNA damage scans. Electron dosage is 4 x 10^8 e^-/nm.

approach. This spring constant has been used by other groups trying to use an AFM tip to tunnel [123, 124]. We also tested the tips by doing force distance curves on our substrate. The curves show that there is no "jump-to-contact" by these tips (Fig. 5.10(b)).

We produced a DNA film on gold to study the effects of tunneling current on DNA, using techniques described in Ch. 4. The DNA film was roughly 5 layers thick, as shown by sweeping the DNA away via a contact-mode AFM scan and then imaging the removed DNA using a tapping-mode AFM scan (Fig. 5.11). After scanning an area with the AFM acting as an STM and then imaging that area with the AFM, we saw a change in the height of the area previously scanned in an STM mode. This result shows the DNA is affected by the STM and appears to be removed from the substrate (Fig. 5.12). This removal could be caused either by the AFM tip sweeping aside the DNA or by the tunneling current breaking up the DNA. We hypothesize that the breaking up of DNA due to tunneling current is the main cause of the depression seen in this image. A small amount of DNA does seem to be pushed to the side of the STM scan region in Fig. 5.12(b), but not as much as we see using the AFM in contact mode. On the majority of scans, very little DNA is pushed to the side, and the depression is still present (Fig. 5.15(a)). To quantify the amount of DNA build up at the edges of a scan, I measured the height change across the contact-mode AFM image (Fig. 5.11(b)) and integrated the area of the depression and the peaks in height. I then made the same measurement on depressions created by the STM (Fig. 5.12). The ratio of contact-mode AFM peaks to depression is approximately 1 : 2 and the ratio of STM

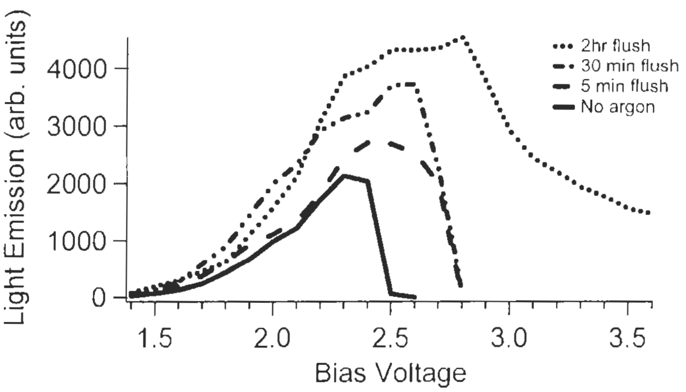

Figure 5.16: Plasmon light emission versus bias voltage for different argon gas flush times.

damage peaks to depression is approximately 1 : 6.

To further test our hypothesis, we measured the depression height for different tip-sample bias voltages using constant scan speed and current set points (Fig. 5.13(a)). With these measurement, we discovered that it was important to have more than a monolayer of DNA because the depressions were nearly all deeper than 2 nm. We also hypothesized that, if we were sweeping the DNA away during the STM scan, the depression height should get larger with a decrease in bias voltage, because decreasing bias voltage causes the tip-sample distance to decrease. Instead, we see that the depression height follows previously published results of quantum yield of DNA single-strand breaks (Fig. 5.14) [125] down to a bias voltage of 0.25 V, where the DNA appears to be swept aside. We hypothesize that near 0.25 V, the tip is close enough to the surface to sweep the DNA aside. This is confirmed by the increase of DNA at the edge of the depressions from 0.75 to 0.25 V (Fig. 5.15). In Fig. 5.15, one can see that at a high tip-sample bias voltage, there is little build up at the edge of a scan. But when the bias is below 0.75 V, there is an increasing amount of build up at the edge of a scan. This should skew our data, leading to an increase in depression at low bias voltages because both the sweeping motion and electron damage is contributing to the depression.

To test this hypothesis, we repeated the STM-AFM DNA damage experiment, this time keeping the tip at a constant height. To do this experiment, we change the bias voltage as before and keep the height constant by varying the current. In order to keep the electron

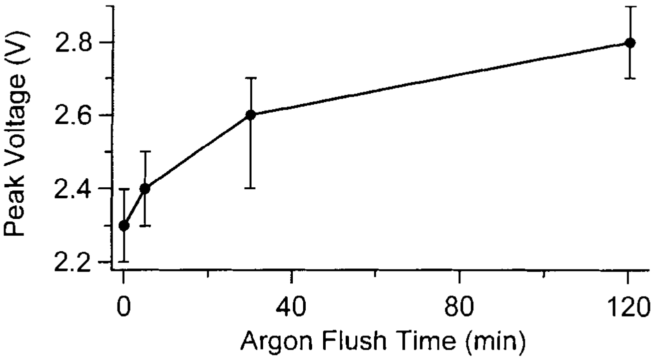

Figure 5.17: Plasmon light emission peak versus argon gas flush time.

intensity constant for each scan, we also varied the scan speed. In other words we kept $\frac{I_{set}}{V_{bias}}$ = constant and changed the scan speed to keep a dosage of 4 x 10^8 e^-/nm while scanning (Table 5.2). With a constant tip-sample distance, our results better follow the quantum yield of DNA single-strand breaks at low bias voltages (Fig. 5.13(b)). Still, these are preliminary results that require more investigation.

5.3 Argon atmosphere

The damage done to a gold surface to destroy the plasmon emission in air at voltages $\geq$ 2.1 V, might be caused by electrical breakdown of the air resulting in an arc of current into the gold [68]. We hypothesized that it was likely the water in the air that caused the electrical breakdown. To test this hypothesis, we tried using our STM in an argon atmosphere, which would reduce the amount of evaporated water in the system.

We proceeded by enclosing our STM and flushing our system with argon for increasing lengths of time. We then recorded the emission intensity of the gold plasmons while scanning a region and averaged the intensity for the entire region. This gave us a higher cutoff for surface damage in air because this process requires more than a single damage event to quench emission. Our results show that the peak emission, and hence the emission cut-off due to gold surface damage, shifts to higher bias voltages depending on how long we flushed the system with argon (Fig. 5.16). It is also interesting to note that after

2 hours of flushing, the emission was not cutoff at the maximum bias voltage we tested. We conclude that something in ordinary air, probably water droplets or oxygen, leads to the observed breakdown of the gold surface at high electric fields. From a practical point of view, this technique also allowed us to collect spectra using bias voltages greater than 2.1 V (Fig. 5.17) without a vacuum system.

When looking at DNA with fluorophores, we did not observe significant differences when using argon or air atmospheres. The DNA still appeared as a dark region in the plasmon background, and there was still no sign of fluorophore emission at the higher voltages able to be used. For this reason, I did not spend a lot of time working with the argon atmosphere but spent more time trying to characterize the damage to gold and DNA.

Chapter 6

Discussion

In this chapter, I discuss the results of our experiments and review theories that have been used to explain similar findings. First, I discuss high-bias-voltage STM damage to gold and review three theories that have been used to explain this phenomenon in light of our finding that damage is limited by an argon atmosphere. Second, I discuss the contrast inversion and dark DNA images seen while imaging DNA under different conditions. I then review the different theories that have been used to explain contrast inversion in light of the dark DNA images. Third, I discuss the DNA spreading seen in the dark DNA images and try to explain the spreading using recent results in DNA-damage experiments.

6.1 High-bias-voltage STM damages gold

We observed that imaging a gold substrate using bias voltages greater than 2.1 V in air damaged the gold surface, causing a loss of plasmon emission from that area (Fig. 5.9). This result has been seen by other groups using an STM in air [111,120]. Here, I summarize previous arguments that attribute the loss of plasmon emission to local modifications of the gold surface. I also relate our findings to these arguments.

6.1.1 Local density of states change

The first explanation of the lowering of emission focuses on the role played by contaminants, Sivel *et al.* first showed that a gold film covered with a 0.5 nm thick carbon film decreases plasmon emission [111]. They then showed that scanning the area with a negative surface bias voltage partially sweeps the carbon away and restores plasmon emission. They hypothesized that this process mimics how an STM creates a non-emissive area. Both processes are reversible using a -1.80 V surface bias voltage scan of the area. Sivel *et al.* explain the reduction in plasmon light emission by noting that the transition probability for tunneling depends on the local density of states (LDOS) of the tip and the substrate. When contaminants are absorbed onto the gold substrate, the LDOS locally decrease for a given energy, decreasing the transition probability at that energy. They hypothesize that the LDOS for the energy that inelastic tunneling electrons would use to excite plasmons is reduced, thus decreasing the photon emission [68].

6.1.2 Tip-height change

Another effect produced by contaminants is that photon emission rates are decreased by an increase in tunneling distance when contaminants are imaged as protrusions on a surface [118]. Smolyanov *et al.* showed that light emission in air drops exponentially as the tunneling gap increases and fit his data using [126]

$$L \sim \left(1 - \frac{\hbar\nu}{eV}\right) e^{-kd}, \tag{6.1}$$

with L the intensity of light, ω the frequency of light emitted, V the STM bias voltage, d the tip separation distance, and k the decay constant. The factor $(1 - \hbar\nu/eV)$ models the effect of energy conservation, as only electrons with energy greater than $\hbar\nu$ can lead to light emission. For a gold surface and platinum tip they observed $k = 2.3$ nm^{-1} [126]. In our case, the observed emission from high-bias-voltage gold damage is greater than predicted using Eq. 6.1. That equation predicts that a 0.15 nm tip-sample separation increase should decrease the light emission by a factor of 0.71, but the actual decrease is a factor of ≈ 0.25 (Fig. 5.5). Whether a more precise calculation of the light reduction could explain the discrepancy is not clear.

6.1.3 Gold rearrangement

Another theory for the loss in light-emission involves perturbed areas on the gold surface. Pechou *et al.* studied the creation of non-emissive areas under hydrophobic mineral oil on newly created gold films [127]. Although the oil does not remove all water and other contaminants from the surface, it does reduce the amount. In a later experiment, Pechou *et al.* showed that a non-emissive area has an apparent height ≈ 0.1 nm and hypothesized that the surface changes at the atomic scale [120]. Based on these two findings, they suggest that large electric fields produced by using a high bias voltage form disorganized atoms on the gold surface. These disorganized atoms produce a highly perturbed electrostatic surface potential that prevent localized surface plasmons from forming.

6.1.4 Our results

In our experiment, we find that the dark area produced by scanning with bias ≥ 2.1 V is 0.15 nm in height and changes light emission by a factor of ≈ 0.25, as seen above (Fig. 5.5). When we tried to create dark areas in an argon atmosphere, the bias voltage necessary to prevent plasmon emission increased with the flush time for argon into the system. This suggests that the mechanism creating this change depends on a constituent of air, for example oxygen. Perhaps, molecules from air collect on the surface to prevent emission, or they help initiate a change in the gold structure itself to create the non-emissive area. It is possible to isolate which component of air creates the damage via further experiments using gases made of the different constituents of air. To study the possibility that the dark area is created by a change in height, we could measure the change in light emission versus change in height for our system to get a better quantitative model of this effect and compare with our results. To study the possibility that the dark area is created by a change in the LDOS, we could use scanning tunneling spectroscopy to measure the change in local density of states or use ultraviolet photoelectron spectroscopy and inverse photoemission spectroscopy on a DNA film to measure the occupied and unoccupied states before and after DNA absorption.

6.2 Contrast inversion and dark images of DNA

Over the course of this project, we have seen that DNA can appear as both positive and negative heights in a topographical image. We have also seen that the DNA appears, in light-emission images, to be a dark area in the plasmon light-emission background. I discuss a few explanations of these phenomena.

6.2.1 DNA-assisted breakdown

One possibility is that the presence of DNA leads to a change in the gold structure, causing the dark areas to form via the same mechanism as with high voltages in air (Sec. 6.1.3). In this scenario, the DNA, which is infused with water, catalyzes the breakdown, creating an arc of current from the tip to the substrate. Two results cause me to doubt this scenario: The dark images of DNA, compared to the background plasmon emission, appear at voltages (≥ 1.8 V) that are lower than those where damage to gold has been seen. Second, the dark DNA image is seen using a 2.0 V bias in an argon-flushed atmosphere (10 minutes flush), which should prevent damage to the gold substrate. Still, it is possible that the localized concentration of water inside the DNA could bypass the usual pathway for this damage and allow it to happen under different parameters. One could test this further by drying the DNA before imaging. Even so, it is hard to see how the water in the DNA can change the contrast of the imaged DNA.

6.2.2 Tunneling gap changes

Another possible explanation for the dark images of DNA is a change to the tunneling gap by the DNA molecule and counterions. DNA and counterions may alter the potential landscape between the tip and the substrate as seen by the STM [128]. This change can explain the contrast inversion seen by the STM, but it relies on the increase in tip-height distance for the darkness. The change to the potential landscape involves the concentrations of counterions changing the tunneling barrier at different voltages. The charge distribution on DNA also strongly modifies the vacuum potential, causing the DNA to appear as a protrusion with low current settings or high voltage settings and as a depression at high current settings or low voltage settings. The exact tip-sample bias for this change from a depression to a protrusion depends on the counterions present on the DNA and is thus different for each sample. To explain why DNA appears as a dark area in the plasmon background, note that in an air STM, an increase in the tunneling gap produces an exponential decrease in plasmon light emission [126]. Still, this explanation for the reduced emission does not account for the measured decrease in emission (Sec 6.1.2, above). Using Eq. 6.1, a 0.4 nm height change is predicted to change emission by a factor of ≈ 0.4 to be compared to the observed factor of ≈ 0.1. Again, Eq. 6.1 is given without coefficients which does not allow us to rule its use out.

6.2.3 Local density of states changes

It is possible that the DNA absorbed onto the surface changes the local density of states. An STM probes the unoccupied states of the surface that are eV above the Fermi level [129]. As stated above in Sec. 6.1.1, the transition probability for tunneling depends on the local density of states (LDOS) of the tip and the substrate. When contaminants are absorbed onto the gold substrate, the LDOS locally decrease at a given energy, and this decreases the transition probability at that energy. The elastic tunneling channel is then determined by the unoccupied density of states at energies $E = E_f + eV$. For DNA to appear as a depression at low eV and a protrusion at high eV, it must decrease the unoccupied density of states for low energies and increase the unoccupied density of states for high energies [68]. This would give the effect of a depression at low energies and a dark region when the inelastic tunneling at high bias attempts to tunnel into the low-energy states and at the same time produce a topographic protrusion as the elastic tunneling portion goes into the less occupied high energy states.

6.2.4 Resonant tunneling

Resonant tunneling can also be used to explain some of the features we see [130]. In this scenario, electrons tunnel from the tip into the LUMO of the DNA and then tunnel into the gold surface. This pathway exists at bias voltages high enough for the electron to enter into the LUMO of the DNA, V_{cutoff}. When $V_b \geq V_{cutoff}$ the electrons would be able to use the resonant tunneling path to tunnel into the DNA, which is above the gold surface, to create a protrusion. The resonant tunneling pathway changes how the electrons tunnel into the gold which effects the plasmon emission. It is not clear if the electrons tunnel inelastically to compete with the plasmon emission pathway or if they would change the orientation of electrons passing through the plasmon but if resonant tunneling is to be used to explain a change in plasmon emission it would suggest that one of these is true. This would lower the probability of plasmon excitation by tunneling electrons and lead to a lowering of plasmon emission.

6.2.5 Our results

In our experiment, we find that the dark area created by DNA is present whenever the STM bias voltage is high enough to allow a light emission image to be created in a reasonable time (1.8 V requires 40 min to produce an image). While collecting the light emission image the DNA appears as a protrusion, ranging from 0.1 to 0.4 nm. The light emission intensity is reduced at the location of the DNA molecule by a factor of ≈ 0.1.

It is not clear which of the above explanations is correct from our experiment. Still, amongst the various possibilities described above, I believe the most plausible explanation is a change to the LDOS. This theory can explain all the features we see when scanning DNA and is integral to the tunneling process. It has also been successful in explaining similar results seen while imaging oxidized metals using plasmon emission in an STM. To further investigate the possibility changes in the LDOS are the strongest contributor to the imaging effects, we could use scanning tunneling spectroscopy to the study changes in local density of states or use ultraviolet photoelectron spectroscopy and inverse photoemission spectroscopy on a DNA film to measure the occupied and unoccupied states before and after DNA absorption. As for the other explanations, resonant tunneling surely occurs when DNA is scanned using a bias voltage large enough to allow electrons to go into the LUMO of DNA. DNA spreading, discussed below also is consistent with this effect. I believe resonant tunneling is a contributing factor to our observed results but not the greatest contributing factor. It also cannot be used to explain the depression seen at low bias voltages. To further investigate how resonant tunneling affects DNA imaging, we could use scanning tunneling spectroscopy and compare DNA vibrational modes in our plasmon excitation energy range to investigate whether electrons tunnel inelastically through DNA to reduce plasmon excitation. The DNA-assisted breakdown, described above, is not likely the reason for the darkness because this would require the DNA to be a catalysis for the gold damage, as the dark area appears at voltages well below regular gold damage. The changes to the potential barrier created by counterions can explain the contrast inversion seen when scanning DNA. To explain the dark area in a plasmon emission background that corresponds with DNA, however, requires another theory. I combine a tip-height change with the counterion argument to explain the light emission change in terms of this theory (Sec. 6.2.2). As stated in Sec. 6.1.4, to study whether the dark area is created by tunneling gap changes, we could measure the change in light emission versus change in tip-height on a bare gold sample to get a quantitative model of this effect and compare with our results. It is also possible that a layer of organic material or carbon may alter the plasmon wavelength. For example, if damaged DNA leaves behind a carbon film, then Eq. 2.32 should use the dielectric constant of carbon (≈ 2.5), instead of air. Doing so would red shift the surface plasmon wavelength by a factor of 1.36, moving the plasmon peak from 750 nm (Fig. 5.3) to 1020 nm. Using our light detection equipment in this wavelength region, we would have a reduced signal because the quantum efficiency is low (Fig. 3.11). I believe that more than one of these explanations may be contributing to our results, but determining the most important factor is difficult.

6.3 DNA spreading and DNA film depressions caused by STM scans

Our results show a change in the light-emission images of DNA over the course of repeated imaging (Sec. 5.2.2). The DNA appears to spread and darken from the first light-emission image to the second. After the second image, the DNA changes little if there is small amount of DNA. But if there is a large amount of DNA coiled on the surface, the dark area continues to spread. Our results also show that an STM scan on a DNA film can create a depression (Sec. 5.2.3). The depression height follows the results of electron bombardment on DNA films by an electron gun. It was shown that the probability of SSB versus electron energies follows a curve similar to base-pair cross sections. We find that STM tunneling electrons create a depression height versus bias voltage that also follows closely to probability of SSB versus electron energies. We hypothesize that the changes in the light-emission images and the depressions seen on DNA films are caused by tunneling of the electrons that damages the DNA. This is surprising because the energy of the tunneling electrons (≈ 2 eV) is well below the bond energies of DNA (≈ 8 eV). In addition, other polymers have been successfully imaged using an STM [131, 132]. In this section, I discuss two different mechanisms for DNA damage by tunneling electrons. First, I discuss the possibility that the STM current locally heats the DNA to temperatures that destroy it. Second, I review recent experiments that show that DNA can be directly damaged by low-energy electrons.

6.3.1 Temperature considerations

Electrons tunneling from the STM tip to the substrate dissipate some of their energy by heating the substrate. A hot substrate can denature and even break down DNA.

To estimate the energy that is transfered into the gold substrate, let us consider the electrons as a heat source. The tunneling electrons supply a power

$$P = IV, \tag{6.2}$$

with P the power, I the current, and V the bias voltage. We observe DNA damage at about 2 V bias and 2 nA of current, which gives a power of 2.5 x 10^{10} eV/s. To estimate the substrate heating, we use Fourier's law of conduction

$$P/A = -\lambda \nabla T \tag{6.3}$$

with A the area perpendicular to the heat flow, λ the thermal conductivity, and T the temperature. Using cylindrical coordinates and assuming a steady state, we solve Laplace's equation to find the temperature rise, $\delta T = \frac{C}{r}$. The area perpendicular to the heat flow in this case is modeled as a half sphere, which allows us to solve for C to find [133],

$$\delta T = \frac{P}{2\pi r \lambda}, \tag{6.4}$$

with r equal to the radius of the electron beam. Using $r = 1$ x 10^{-9} m and $\lambda = 1.98$ x 10^{21} eV/mC, we estimate a local temperature increase of $\approx 0.01°C$, well below the increase ($\approx$ 100°C) needed to damage DNA.

6.3.2 Low-energy electron damage

An unexpected recent discovery is that low-energy electrons can damage double-stranded DNA [134]. The observation is important because it raises the possibility that low-energy electrons from a small dose of radiation can harm human DNA. Electrons with an energy as low as 0.1 eV can cause single-stranded breaks (SSB) in DNA. These new findings have caused scientists to rethink the safe dosage of radiation used in different imaging processes [135].

Bombarding DNA with low-energy electrons from an electron gun in a vacuum (5 x 10^{-9} Torr) gives a probability $\mathcal{O}(10^{-3}/\mathrm{e}^-)$ for electrons to cause a SSB in DNA [125, 136].

The yield of breaks as a function of electron energy has a sharp peak at ≈ 0.8 eV and a broader peak at ≈ 2.2 eV, which Martin *et al.* point out is close to the modeled electron capture cross section of DNA [125]. The SSB probability is significant since STM tunneling currents of picoamperes are equivalent to $\approx 10^9$ electrons per second. Such currents could result in $\geq 10^6$ breaks per second while scanning DNA, implying total destruction of the DNA. To estimate the number of SSB per base-pair (bp) when imaging DNA with an STM, I calculate the number of breaks per second using the set current and probability of SSB, and then convert this to an estimate for SSB per bp with the speed of my scan in bp per second,

$$\frac{SSB}{bp} = \frac{SSB/s}{bp/s} = \frac{IK\varepsilon}{fL/\ell}, \tag{6.5}$$

$$= \frac{\left(\frac{C}{s}\right)\left(\frac{e^-}{C}\right)\left(\frac{SSB}{e^-}\right)}{\left(\frac{1}{s}\right)(nm)\left(\frac{bp}{nm}\right)} = \frac{(1\,\mathrm{x}\,10^{-12})\ (6.24\,\mathrm{x}\,10^{18})\ (10^{-3})}{(1)\ (200)\ (0.34)}, \tag{6.6}$$

with I the set point current, K a constant conversion factor, ε the probability of a SSB per electron [125], f the scanning frequency, L the length of the scan line (forward and reverse), and ℓ the length of a bp along a ds-DNA molecule. Using Eq. 6.5, I estimate that scanning a 100 nm^2 square area (L =200 nm) at 1 Hz using 1 pA, would produce ≈ 10 breaks/bp. It is virtually certain that a bp will be damaged as we scan over it at regular STM currents. Low-energy electrons seem to create only single strand breaks but two single-strand breaks in close proximity (≤ 7 bp) can create a double-strand break [137, 138]. The high current density in an STM could thus easily lead to multiple double-strand breaks.

The cross section for single-strand breaks in DNA was studied in the same way using an electron gun in a vacuum with energies ranging from 0.1 eV to 4.7 eV [139]. The effective cross section for the production of SSB in DNA was $\mathcal{O}(10^{-14})$ cm^2. Interestingly, a similar study was done on DNA using electrons of 10 eV to 50 eV; at this energy range, the cross section is also $\mathcal{O}(10^{-14})$ cm^2 [140]. From this result, low-energy electrons have about the same efficiency in producing SSB as higher-energy electrons, likely because the slower speed of low-energy electrons allows more time to be captured by the DNA.

There are two theories that purport to explain how low-energy electrons (0–3 eV) can initiate bond breakage. In the first, the electron is captured by the phosphate group in the backbone to form a transient negative ion that causes the break [125, 141, 142]. In the second, a break is caused by low-energy electrons that are captured by nucleotides in the

DNA and migrate to the phosphate group to form a transient negative ion that creates a strand break (Fig. 6.1) [143–146]. Results showing that the SSB probability depends on the attached nucleotide imply that the second theory is correct [147]. But the mechanism is still under investigation. In either case, after electron attachment, there is a C-O bond break between the sugar and phosphodiester that produces the SSB [147, 148].

With our results in mind, it is an interesting question to ask whether one can image DNA without damaging it. With the calculation above, one would need to scan at 20 Hz using 1 pA of current to have a 50% probability of bp damage. This would allow one to image a single bp region with about 500 electrons. Still, with these settings it is likely that you would produce enough damage across 7 bp that a double-strand break would occur. This brings into question the use of an STM for imaging DNA at all and also suggests another reason why STM imaging of DNA has historically been subject to artifacts and difficulties in interpretation [40]. It is possible that imaging DNA under certain conditions, such as in a buffer solution or at low temperature, would minimize SSB. The DNA damage mechanism discussed here may well be alleviated under such conditions. This is confirmed by the greater reproducibility of results for STM imaging of DNA at low temperatures, which would likely both supress the reaction and cause damaged bits of DNA to be less mobile. [43, 44, 46–49, 51, 52].

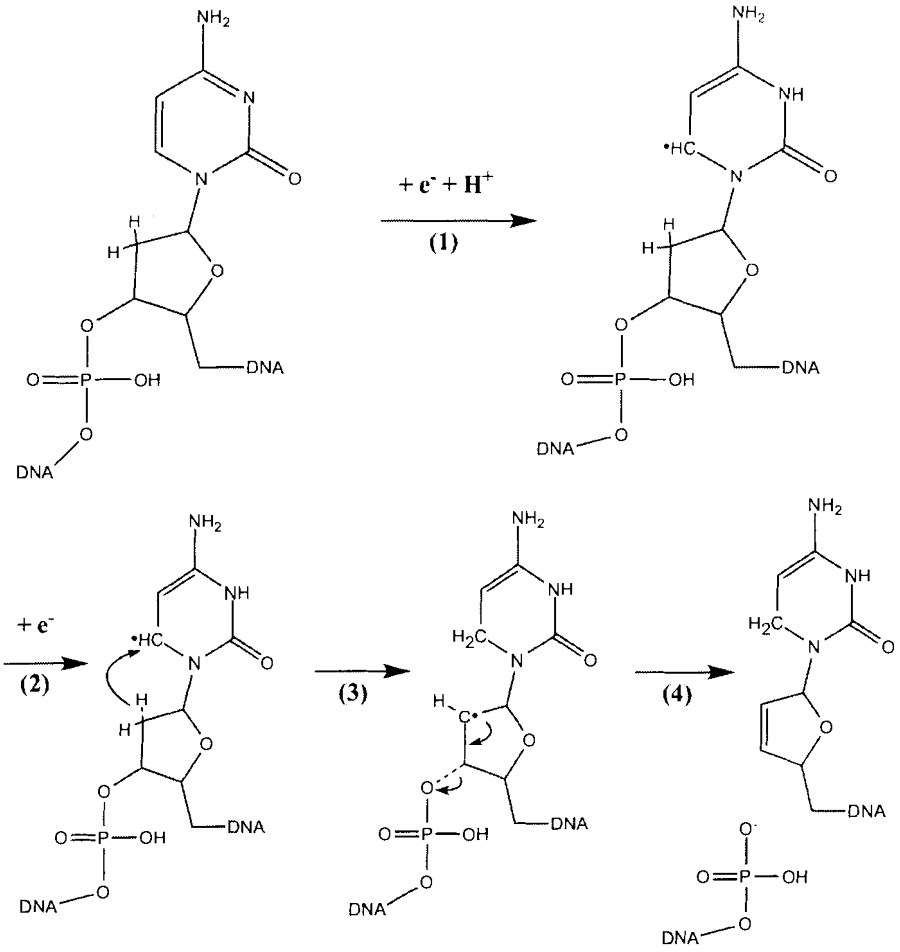

Figure 6.1: Proposed mechanism for a single-strand DNA break from low-energy electron attachment to a nucleotide, second theory discussed in the text [146]. This diagram shows how two low-energy electrons captured by nucleotides in the DNA could migrate to the phosphate group (1-3). Once the electron reaches the phosphate group, it creates a strand break (3-4).

Chapter 7

Conclusion

In this thesis, we have studied DNA using an STM in an attempt to further fluorescence spectroscopy. We began by preparing and testing the STM for studying light emission while scanning and then looked for fluorophores attached to DNA using the STM. During the experiments, we learned more about DNA and how the STM affects it.

We began by setting up the STM and characterized its ability to collect light from gold plasmons. We measured the light collection efficiency of our APD and our spectrometer. Using our measured efficiency, we then accounted for the light lost in our collection optics. We looked at the spectrum of plasmon emission and saw the fermi level spreading seen in room temperature measurements of this spectrum. Then, we imaged the plasmon emission on flat gold and showed that it corresponded with the topographical images. Lastly, we investigated the damage done to gold by tunneling electrons that create a non-emissive region on the gold surface.

We then created samples to study fluorophores attached to DNA. We began by developing a protocol for preparing flat, transparent, conductive gold on mica. We found the optimal values for mica temperature and evaporation rate. After evaporation, we also used flame annealing to create an optimally flat substrate. It was important to create a flat substrate because of the DNA we hoped to absorb and view on it. To prepare the DNA for attachment to the gold, we used a specific buffer for better adhesion and attached fluorophores to our DNA. We checked the protocol for dye attachment by viewing the DNA with attached dye in a fluorescence microscope. Once we saw that the dye was attaching to the DNA, we used an electrostatic deposition method for attaching the DNA to a gold substrate. This method succeeded in depositing controlled amounts of DNA on our gold substrate with minimal contamination. After deposition, we used an AFM to estimate the surface coverage of DNA. We created samples ranging from low densities of DNA — a couple of strands per micron — to high densities — a DNA film on gold, which was very useful in the measurements made.

Next, we studied DNA using an STM. We began by looking at topographic images of DNA on gold and found that the image of DNA corresponds typically to a 0.1 nm depression in the gold surface at low bias. At higher bias, the DNA corresponds typically to a 0.4 nm protrusion and appears as a dark area on the gold plasmon background. The dark area grew and became darker with subsequent scans. We found that it was not the fluorophores that created the described change by looking at DNA that was not dyed and concluded that the DNA itself was changing. We then concluded that electrons might be damaging the DNA. A further review of the literature suggested that electrons bombarded onto DNA at the energies we were using could damage DNA.

We next set out to study the damage done to DNA by tunneling electrons using an AFM to image a DNA film on gold previously scanned with an STM. We found that the DNA film thickness in the area scanned using an STM was significantly reduced without much build-up of DNA at the sides of the scan region. We also measured the depression height versus bias voltage during a set of STM scans and discovered that it followed previous work describing SSB probability versus electron energies for electron bombardment from an electron gun. These two results, with the change in DNA light-emission images, led us to conclude that the DNA was being broken down by the tunneling electrons.

Finally, in an attempt to extend the abilities of our STM, we tested the hypothesis that gold damage is due to a breakdown in the air. We placed our STM in an enclosure and flushed the enclosure with argon gas. We discovered that we could then use higher voltages when imaging a gold substrate without damaging plasmon emission. For our experiment on DNA, the change in atmosphere had little effect because the DNA still appears as a dark region in the plasmon background and spreads with subsequent scans. With a molecule that does not break down when bombarded by tunneling electrons, the ability to use higher tip biases may be useful for extending the possible excitation energy range.

In the future, it may be useful to begin by studying fluorophores on graphite, following Uehara *et al.* [27] using recent work on graphene by WA de Heer *et al.* [149]. For our setup, we could use a thin film of graphite, allowing the fluorophore emission to pass through the graphite and be captured by our optics. After demonstrating that we can see a fluorophore, we could try using a more robust molecule, such as a polymer already reproducibly imaged by an STM [131, 132], to attach fluorophores to and image with an STM. Using an argon atmosphere also allows us to use fluorophores with a lower wavelength, and in the case of TOTO-derived dyes, higher quantum efficiency. This may help in the collection of photons from a fluorophore.

For further study into DNA damage, we need to do more measurements of DNA film damage versus STM bias voltage to confirm our result. For new experiments, we could use the AFM as an STM to create a damaged section large enough that the area could be investigated using Auger or produce enough damaged DNA that it would show up in a gel electrophoresis measurement. We could also image the DNA on a dilute layer with the AFM and then study the changes to the dilute layer caused by tunneling electrons. From the difference seen in DNA conductance measurements and DNA damage measurements, it may be interesting to investigate whether tethering one or two ends of the DNA to gold may help the DNA to not capture the electron but transport it to the gold surface. With the AFM/STM setup, it may also be interesting to study the effects of STM scanning on other surfaces, including the damage done to gold at high biases in air.

Bibliography

[1] J Zlatanova, and SH Leuba, "Stretching and imaging single DNA molecules and chromatin", J. Muscle Res. Cell Motil. **23** (2002) 377–395.

[2] ML Bennink, SH Leuba, GH Leno, J Zlatanova, BG de Grooth, and J Greve, "Unfolding individual nucleosomes by stretching single chromatin fibers with optical tweezers", Nat. Struct. Biol. **8** (2001) 606–610.

[3] M Rief, M Gautel, F Oesterhelt, JM Fernandez, and RE Gaub, "Reversible unfolding of individual titin immunoglobulin domains by AFM", Science **276** (1997) 1109–1112.

[4] J Zlatanova, JM McAllister, S Borukhov, and SH Leuba, "Single-molecule approaches reveal the idiosyncrasies of RNA polymerases", Structure **14** (2006) 953–966.

[5] A Yildiz, and PR Selvin, "Kinesin: walking, crawling or sliding along?", Trends Cell Biol. **15** (2005) 112–120.

[6] Y Sako, and T Yanagida, "Single-molecule visualization in cell biology", Nat. Rev. Mol. Cell Biol. **Suppl** (2003) SS1–SS5.

[7] L Cai, N Friedman, XS and Xie, "Stochastic protein expression in individual cells at the single molecule level", Nature **440** (2006) 358–362.

[8] V Westphal and SW Hell, "Nanoscale resolution in the focal plane of an optical microscope", Phys. Rev. Lett. **94** (2005) 143903.

[9] H Frey, S Witt, K Felderer, and R Guckenberger, "High-resolution imaging of single fluorescent molecules with the optical near-field of a metal tip", Phys. Rev. Lett. **93** (2004) 200801.

[10] J. Lakowicz, *Principles of Fluorescence Spectroscopy*,Second Edition, Plenum Publishing (1999).

[11] S Inoue, "Foundations of confocal scanned imaging in light microscopy", *Handbook of biological confocal microscopy*, Third edition, edited by J Pawley (Springer Science+Business Media, New York, 2006), pp. 1–19.

[12] R Heintzmann, TM Jovin, C Cremer, "Saturated patterned excitation microscopy (SPEM) — a novel concept for optical resolution improvement", J Opt Soc Am A **19** (2002) 1599–1604.

[13] R Heintzmann and Gabriella Ficz, "Breaking the resolution limit in light microscopy", Briefing in fundamental genomics and proteomics **5** (2006) 289–301.

[14] D Axelrod, "Total Internal Reflection Fluorescence Microscopy in Cell Biology", Traffic **2** (2001) 764–774.

[15] J Brewesdorf, A Egner, and S Hell, "4Pi microscopy", *Handbook of biological confocal microscopy*, Third edition, edited by J Pawley (Springer Science+Business Media, New York, 2006), pp. 561–570.

[16] K Bahlmann, S Jacobs, and S Hell, "4Pi-confocal microscopy of living cells", Proc. SPIE **4620** (2002) 137–142.

[17] S Hell, K Willig, M Dyba, S Jakobs, L Kastrup, and V Westphal, "Nanoscale resolution with focused light: Stimulated emission depletion and other reversible saturable optical fluorescence transitions microscopy concepts", *Handbook of biological confocal microscopy*, Third edition, edited by J Pawley (Springer Science+Business Media, New York, 2006), pp. 571–579.

[18] R Thompson, D Larson, and W Webb, "Precise nanometer localization analysis for individual fluorescent probes", Biophys. J. **82** (2002) 2775–2783.

[19] A Yildiz, JN Forkey, SA McKinney, T Ha, YE Goldman, and PR Selvin, "Myosin V walks hand-over-hand: single fluorophore imaging with 1.5-nm localization", Science **300** (2003) 2061–2065.

[20] MP Gordon, T Ha and PR Selvin "Single-molecule high-resolution imaging with photobleaching", Proc. Natl. Acad. Sci. USA **101** (2004) 6462–6465.

[21] S Ram, ES Ward and RJ Ober, "Beyond Rayleigh's criterion: A resolution measure with application to single-molecule microscopy", Proc. Natl. Acad. Sci. USA **103** (2006) 4457–4462.

[22] M Rust, M Bates, and X Zhuang, "Sub-diffraction-limit imaging by stochastic optical reconstruction microscopy (STORM)", Nature Methods **3** (2006) 793–795.

[23] A Sharonov and R Hochstrasser, "Wide-field subdiffraction imaging by accumulated binding of diffusing probes", PNAS **103** (2006) 18911–18916.

[24] Z Ma, J Gerton, L Wade, and S Quake, "Fluorescence near-field microscopy of DNA at sub-10 nm resolution", Phys. Rev. Lett. **97** (2006) 260801.

[25] C Quate,"Vacuum tunneling: A new technique for microscopy", Physics Today **39** (1986) 26–34.

[26] V Fourmond, "Can one Excite Fluorescence of Dye molecules with a scanning tunneling microscope", Report to Ecole Normale Superieure, (2002).

[27] Y. Uehara and S. Ushioda, "Single molecular spectrum of rhodamine 6G on highly oriented pyrolytic graphite", Appl. Phys. Lett. **86** (2005) 181905.

[28] R Akiyama, T Matsumoto, and T Kawai, "A scanning tunneling microscopy study of electrostatic and proximity effects in tip-assisted migration of a DNA Base molecule on $SrTiO_3$", J. Phys. Chem. B **103** (1999) 6103–6110.

[29] DP Allison, LA Bottomley, T Thundat, GM Brown, RP Woychik, JJ Schrick, KB Jacobson, and RJ Warack, "Immobilization of DNA for scanning probe microscopy", Proc. Natl. Acad. Sci. **89** (1992) 10129–10133.

[30] MH Dishner, M Ivey, S Gorer, JC Hemminger, and FJ Feger, "Preparation of gold films by epitaxial growth on mica and the effects of flame annealing", J. Vac. Sci. Technol. A **16** (1998) 3295–3300.

[31] ZH Liu and N Brown, "Studies using AFM and STM of the correlated effects of the deposition parameters on the topography of gold on mica", Thin Solid Films **300** (1997) 84–94.

[32] Y Lyubechenko, SM Lindsay, JA Rose, and T Thundat, "A technique for stable adhesion of DNA to a modified graphite surface for imaging by scanning tunneling microscopy", J. Vac. Sci. Technol. B **9** (1991) 1288–1290.

[33] W.M. Heckl and G. Binnig, "Domain walls on graphite mimic DNA", Ultramicroscopy, **42-44** (1992) 1073–1078.

[34] C Clemmer and T Beebe, "Graphite — A mimic for DNA and other biomolecules in scanning tunneling microscope studies", Science **251** (1991) 640–642.

[35] SM Lindsay and B Barris, "Imaging deoxyribose nucleic acid molecules on a metal surface under water by scanning tunneling microscopy", J. Vac. Sci. Technol. A **6** (1988) 544–547.

[36] T Thundat, LA Nagahara, and SM Lindsay, "Direct observation of bioelectrochemical processes by scanning tunneling microscopy", J. Vac. Sci. Technol. A **8** (1990) 645–647.

[37] TW Jing, AM Jeffrey, JA DeRose, YL Lyubchenko, LS Shlyakhtenko, RE Harrington, et al., "Structure of hydrated oligonucleotides studied by *in situ* scanning tunneling microscopy", Proc. Natl. Acad. Sci. USA **90** (1993) 8934–8938.

[38] A Cricenti, S Selica, AC Felici, R Generosi, E Gori, W Djaczenko, G Chiarotti, "Molecular structure of DNA by scanning tunneling microscopy", Science **245** (1989) 1226–1227.

[39] LA Bottomley, JN Haseltine, DP Allison, RJ Warwmack, T Thundat, RA Sachleben, GM Brown, RP Woychik, KB Jacobson, and TL Ferell, "Scanning tunneling mi-

croscopy of DNA: The chemical modification of gold surfaces for immobilization of DNA", J. Vac. Sci. Technol. A **10** (1992) 591–595.

[40] DP Allison, T Thundat, KB Bruce, LA Bottomley, and RJ Warmack, "Imaging entire genetically functional DNA molecules with the scanning tunneling microscope", J. Vac. Sci. Technol. **11** (1993) 816–819.

[41] DD Dunlap, R Garcia, E Schabtachi, and C Bustamante, "Masking generates continuous segments of metal-coated and bare DNA for scanning tunneling microscope imaging", Proc. Natl. Acad. Sci. USA **90** (1993) 7652–7655.

[42] DCG Klein, L Gurevich, JW Janssen, and LP Kouwenhoven, JD Carbeck, and LL Sohn, "Ordered stretching of single molecules of deoxyribose nucleic acid between microfabricated polystyrene lines", Appl. Phys. Lett. **78** (2001) 2396–2398.

[43] T Kanno, H Tanaka, T Nakamura, H Tabata, and T Kawai, "Real space observation of double-helix DNA structure using a low temperature scanning tunneling microscopy", Jap. J. Appl. Phys. **38** (1999) L606–L607.

[44] T Kanno, H Tanaka, T Nakamura, H Tabata, and T Kawai, "Does the Macrostructure of Deoxyribonucleic Acid Molecules Absorbed on Substrates by the Pulse Injection Method Reflect That in Solution", Jap. J. Appl. Phys. **39** (2000) 581–582.

[45] T Kanno, H Tanaka, N Miyoshi, M Fukuda, and T Kawai, "Base sequence dependence of DNA studied by scanning tunneling microscopy", Jap. J. Appl. Phys. **39** (2000) 1892–1893.

[46] C Hamai, H Tanaka, and T Kawai, "Extended structure of DNA oligomer and nucleotide imaging studied by scanning tunneling microscopy", J. Phys. Chem. B **104** (2000) 9894–9897.

[47] M Nishimura, H Tanaka, and T Kawai, "Structure of linear double-stranded deoxyribonucleic acid adsorbed on Cu(111) Surfaces: a low-temperature scanning tunneling microscopy study", Jap. J. Appl. Phys. **41** (2002) 7510–7511.

[48] M Nishimura, H Tanaka, and T Kawai, "High-resolution scanning tunneling microscopy imaging of Escherishia coli lysine transfer ribonucleic acid", J. Vac. Sci. Technol. B **21** (2003) 1265–1267.

[49] H Tanaka, T Kawai, "Visualization of detailed structures within DNA", Surf. Sci. **539** (2003) L531–L536.

[50] Y Nojima, H Tanaka, Y Yoshida, and T Kawai, "High-resolution scanning tunneling microscopy and spectroscopy studies of deoxyribonucleic acid and fluorescein isothiocyanate", Jap. J. Appl. Phys. **43** (2004) 5526–5527.

[51] E Shapir, J Yi, H Cohen, A Kotlyar, G Cuniberti, and D Porath, "The puzzle of contrast inversion in DNA STM imaging", Phys. Chem. B **109** (2005) 14270–14274.

[52] E Shapir, H Cohen, N Borovok, A Kotlyar, and D Porath, "High-resolution STM imaging of novel Poly(G)-Poly(C) DNA molecules", J. Phys. Chem. B **110** (2006) 4430–4433.

[53] SM Lindsay, OF Sankey, Y Li, C Herbst, and A Rupprecht, "Pressure and Resonance effects in scanning tunneling microscopy of molecular absorbates", J. Phys. Chem. **94** (1990) 4655–4660.

[54] R Guckenberger, B Hacker, T Hartmann, T Scheybani, Z Wang, W Wiegrabe, W Baumeister, "Imaging of uncoated purple membrane by scanning tunneling microscopy", J. Vac. Sci. Technol. B. **9** (1991) 1227–1230.

[55] V Sivel, R Cotager, F Ajustron, and J Beauvillain, "Control of photon emission by scanning tunneling microscopy in air", Phys. Rev. B **50** (1994) 5628–5634.

[56] P Johannson, "Theory of Inelastic Tunneling: Applications to Double-Barrier Structures and Scanning Tunneling Microscopes.", Phd thesis, Chalmers University, Goteborg, Sweden, 1991.

[57] W Knoll, "Interface and thin films as seen by bound electromagnetic waves", Annu. Rev. Phys. Chem. **49** (1998) 569–638.

[58] C Kittel, *Introduction to Solid State Physics*, 6^{th} ed., Wiley, New York, (1986).

[59] EA Stern, RA Ferrel, "Surface oscillations of the electron plasma in a metal", Bull. Am. Phys. Soc. **3** (1958) 191.

[60] EA Stern, RA Ferrel, "Surface Plasma Oscillations of a Degenerate Electron Gas", Phys. Rev. A **120** (1960) 130–136.

[61] P Johansson, R Monreal, and P Apell, "Theory for light emission from a scanning tunneling microscope", Phys. Rev. B **42** (1990) 9210–9213.

[62] T Takemori, M Inoue, and K Ohtaka, "Optical Response of a sphere coupled to a metal substrate", J. Phys. Soc. Jpn. **56** (1987) 1587–1602.

[63] RW Rendell, DJ Scalapino, "Surface plasmons confined to microstructures on tunneling junctions", Phys. Rev. B **24** (1981) 3276–3294.

[64] R Berndt, JK Gimzewski, and P Johansson, "Inelastic tunneling of tip-induced plasmon modes on noble metal surfaces", Phys. Rev. Lett. **67** (1991) 3796–3799.

[65] BNJ Persson and A Baratoff, "Theory of photon emission in electron tunneling to metallic particles", Phys. Rev. Lett. **68** (1992) 3224–3227.

[66] P Johannson, and R Monreal, "Theory for photon emission from a scanning tunneling microscope", Z. Phys. B **84** (1991) 269–275.

[67] P Johansson, "Light emission from a scanning tunneling microscope: Fully retarded calculation", Phys. Rev. B **58** (1998) 10823–10834.

[68] R Berndt, and J Gimzewski, "Photon emission in scanning tunneling microscopy: Interpretation of photon maps of metallic systems", Phys. Rev. B **48** (1993) 4746–4754.

[69] R Nishitani, T Umeno, A Kasuya, and Y Nishina, "Correlation between scanning tunneling microscopy (STM)-induced photon map and the STM topography of nanometer-size metal particles", Scanning Microscopy **12** (1998) 113–118.

[70] R Chance, A Prock, R Sibley, "Molecular fluorescence and energy transfer near interfaces", Adv. Chem. Phys. **34** (1978) 1–65.

[71] J Enderlein, "A theoretical investigation of single-molecule fluorescence detection on thin metallic layers", Biophys. J. **78** (2000) 2151–2158.

[72] O Verhage, "Investigations of light emission from the tunneling junction of a scanning tunneling microscope", Dept. of Physics, Report to Utrecht University, (2005).

[73] J Zhang and R Lakowicz, "Metal-enhanced fluorescence of an organic fluorophore using gold particles", Optics Express **15** (2007) 2598–2506.

[74] S Wennmalm and R RIgler, "On death numbers and survival times of single dye molecules", J. Phys. Chem. B **103** (1999) 2516–2519

[75] L Deschenes and D Vanden Bout, "Single molecule photobleaching: increasing photon yield and survival time through suppression of two-step photolysis", Chem. Phys. Lett. **365** (2002) 387–395.

[76] A Diaspro, G Chirico, C Usai, P Ramoino, and J Dobrucki, "Photobleaching", *Handbook of biological confocal microscopy*, Third edition, edited by J Pawley (Springer Science+Business Media, New York, 2006), pp. 690–702.

[77] Invitrogen, TOTO-3, www.probes.com, Ontario, Canada.

[78] Dr. Volker Klocke Nanotechnik, www.nanomotor.de, Aachen, Germany.

[79] Electronics123.com, C-Cam2AX CMOS Camera Module, www.electronics123.net, Ohio, USA.

[80] M Honda, "Unipolar charge induction on moving parts in static field", IEEE, (2001), 422–425.

[81] J Garnaes, F Kragh, KA Morch, and AR Tholen, "Transmission electron microscopy of scanning tunneling tips", J. Vac. Sci. Technol. A **8** (1990) 441–444.

[82] L Hockett and E Creager, "A convenient method for removing surface oxides from tungsten STM tips", Rev. Sci. Instrum. **64** (1993) 263–264.

[83] DW Pohl, "Some Design Criteria in Scanning Tunneling Microscopy", IBM J. Res. Develop. **30** (1986) 417–427.

[84] SI Park, CF Quate, "Theories of the feedback and vibration isolation systems for the scanning tunneling microscope", Rev. Sci. Instrum. **58** (1987) 2004–2009.

[85] Thor Labs, A1 broadband antireflective coating, www.thorlabs.com.

[86] Carl Zeiss, CP-Achromat 100x, Oberkochen, Germany.

[87] L Mortara, and A Fowler, "Evaluations of Charge-coupled devices (CCD) performance for astronomical use", Proc. Soc. Photo-optical Inst. Eng. **290** (1981) 28–31.

[88] S Inoue, and K Spring, *Video Microscopy: The Fundamentals*, 2^{nd} ed., Plenum Press, New York, (1997).

[89] Ocean Optics, QE65000 spectrometer, Florida, United States of America.

[90] PerkinElmer, SPCM-AQR-14-FC, Quebec, Canada.

[91] Ocean Optics, QE65000 spectrometer, www.oceanoptics.com, Florida, USA.

[92] U Hopfner, H Hehl, and L Brehmer, "Preparation of ordered thin gold films", Appl. Surf. Sci. **152** (1999) 259–265.

[93] C Nogues, and M Wanunu, "A rapid approach to reproducible, atomically flat gold films on mica", Surf. Sci. **152** (2004) 383–389.

[94] M Levlin, A Laakso, HE Niemi, and P Hautojarvi, "Evaporation of gold thin films on mica: effect of evaporation parameters", Appl. Surf. Sci. **115** (1997) 115–120.

[95] JA Derose, T Thundat, LA Nagahara, and SM Lindsay, "Gold grown epitaxially on mica: conditions for large area flat faces", Surf. Sci **256** (1991) 102–104.

[96] S Lu, "Conductivity measurements of single DNA molecules using conductive-atomic force microscopy", MSc Thesis, Simon Fraser University, British Columbia, Canada, 2006

[97] Kurt J. Lesker Company, Quartz-crystal sensor LI00810G10, Pennsylvania, USA.

[98] OS Heavens, "Optical Properties of Thin Films" Rep. Prog. Phys. **23** (1960) 1–65.

[99] B Gauthier-Manuel, “Simultaneous determination of the thickness and optical constants of weakly absorbing thin films”, Meas. Sci. Technol. **9** (1998) 485–487.

[100] Blazer, GB2001 piezo electronic micro torch, New York, USA.

[101] HP Spielmann, D Wemmer,and JP Jacobsen, “Solution structure of a DNA complex with the fluorescent bis-intercalator TOTO determined by NMR spectroscopy”, Biochemistry **34** (1995) 8542–8553.

[102] Novascan Technologies Inc., PSD-UV, www.novascan.com, Indianapolis, USA.

[103] Millipore, Ultrapure water system, Massachusetts, USA.

[104] C Bustamante, J Vesenka, C Tang, W Rees, M Guthod and R Keller, “Circular DNA molecules imaged in air by scanning force microscopy”, Biochemistry **31** (1992) 22–26.

[105] D King, “Oxidation of gold by ultraviolet light and ozone at 25 C” J. Vac. Sci. Tech. A **13** (1995) 1247–1253.

[106] A Krozer and M Rodhal, “X-ray photoemission spectroscopy study of UV/ozone oxidation of Au under ultrahigh vacuum conditions”, J. Vac. Sci. Tech. A **15** (1997) 1704–1709.

[107] Loctite, Loctite 495, Connecticut, USA.

[108] R Berndt, R Gaisch, JK Gimzewski, B Reihl, RR Schlitter, WD Schneider, and M Tschudy, ”Photon emission at molecular resolution induced by a scanning tunneling microscope”, Science **262** (1993) 1425–1427.

[109] SC Meepagala, and F Real, “Detailed experimental investigation of the barrier-height lowering and the tip-sample force gradient during STM operation in air”, Phys. Rev. B. **49** (1994) 15–18.

[110] Melles Griot Catalogue, “Practical Application of Light”, Vol. X, 2005.

[111] V Sivel, R Coratger, F Austron, and J Beauvillain, “Interpretation of the control of the photon emission stimulated by STM”, Phys. Rev. B **51** (1995) 14598–14603.

[112] ZH Wu, T Nakayama, M Sakurai, and M Aono, "Edge enhancement of light emission from Au particles induced by an STM", Phys. lett. A **234** 396–400.

[113] ThermoOriel MS260i Imaging 1/4 m Spectrograph, model 74050/5.

[114] R Pechou, R Coratger, C Girardin, F Ajustron, and J Beauvillain, "Cutoff anomalies in light emitted from the tunneling junction of a scanning tunneling microscope in air", Appl. Phys. lett. **72** (1998) 671–673.

[115] E Cavar, "Electronic and optical properties of supported C60 molecules studied by scanning tunneling microscopy", PhD Thesis, Ecole Polytechnique Federale de Lausanne, 2005.

[116] K Meguro, K Sakamoto, R Arafune, M Satoh, and U Ushioda, "Origin of multiple peaks in the light emission spectra of a Au(111) surface induced by scanning tunneling microscopy", Phys. Rev. B **65** (2002) 165405.

[117] G Hoffmann, T Maroutian, and R Berndt, "Color view of atomic highs and lows in tunneling induced light emission", Phys. Rev. Lett. **93**, (2004) 7–12.

[118] II Smolyanov, "On the difference between light-emission versus voltage characteristics in air and in UHV" Phys. Lett. A **181** (1993) 175–178.

[119] N Ashcroft and N Mermin, *Solid State Physics*, College Edition,Harcourt Brace College Publishers (1976).

[120] R Pechou, R Coratger, F Ajustron, and J Beauvillian, "Control of light emission from an STM and surface modifications", Surface Science **418** (1998) 1–7.

[121] J Israelachvili, *Intermolecular & surface forces*, 2nd ed., Academic Press (1991).

[122] B Cappella and G Dietler, "Force-distance curves by atomic force microscopy", Surf. Sci. Rep. **34** (1999) 1–104.

[123] S Kitamura, M Iwatsuki, "Observations of 7 X 7 reconstructed structure on the silicon (111) surface using ultrahigh vacuum noncontact atomic force microscopy", Jpn. J. Appl. Phys. **34** (1995) p. L145–148.

[124] FM Battiston, M Bammerlin, C Loppacher, R Luthi, E Meyer, and HJ Guntherodt, "Fuzzy controlled feedback applied to a combined scanning tunneling and force microscope", Appl. Phys. Lett. **72** (1998) 25–27.

[125] F Martin, P Burrow, Z Cai, P Cloutier, D Hunting, and L Sanche, "DNA strand breaks induced by 0-4 eV electrons: The role of shape resonances", Phys. Rev. Lett. **93** (2004) 068101.

[126] II Smolyanov and O Keller, "Cherenkov effect in the context of scanning-tunneling-microscopy", Phys. Stat. Sol. (b) **185** (1994) 275–288.

[127] R Pechou, R Coratger, C Girardin, F Ajustron, and J Beauvillain, "Control of the photon emission in a DTM in air on oil-covered gold surfaces", Eur. Phys. J. AP **2** (1998) 135–138.

[128] DH Kim, E Shapir, H Jeong, D Porath, and J Yi, "Complex ion-distribution induced contrast reversal in STM imaging of DNA", Phys. Rev. B **73** 235416.

[129] RJ Hamers, "Atomic-resolution surface spectroscopy with the scanning tunneling microscope", Ann. Rev. Phys. Chem. **40** (1989) 531–559.

[130] Personal communications with Dr. George Kirczenow.

[131] H Sakaguchi, H Matsumura, H Gong, A Abouelwafa, "Direct visualization of the formation if single-molecule conjugated copolymers", Science **310** (2005) 1002-1006.

[132] H Kasai, H Tanaka, S Okada, H Oikawa, T Kawai, and H Nakanishi, "STM observation of single molecular chains of π-conjugated polymers", Chem. lett. **31** (2002) 696–697.

[133] F Flores, PM Echenique, RH Ritchie, "Energy dissipation processes in scanning tunneling microscopy", Phys. Rev. B **34** (1986) 2899–2902.

[134] J Simons, "How do low-energy $(0.1 - 2$ eV) electrons cause DNA-strand breaks?" Acc. Chem. Res. **39** (2006) 772–779.

[135] L Sanche, "Low energy electron damage in biomolecules", Eur. Phys. J. D **35** (2005) 367–390.

[136] T Solomun, C Hultschig, and E Illenberger, "Microarray technology for the study of DNA damage by low-energy electrons", Eur. Phys. J. D, **35** (2005) 437–441.

[137] DI D'Souza, and L Harrison, "Repair of clustered Uracil DNA damage in *Escherchia Coli*", Nucleic Acid Research **31** (2002) 4573–4581.

[138] R Hanai, M Yazu, K Hieda, "On the experimental distinction between SSBs and DSBs in circular DNA". Int. J. Rad. Bio. **73** (1998) 475–479.

[139] R Panajotovic, F Martin, P Cloutier, D Hunting, and L Sanche, "Effective cross section for production of single-strand breaks in plasmid DNA by 0.1 eV to 4.7 eV electrons", Radiat. Res. **165** (2006) 452–459.

[140] B Boudaiffa, P Cloutier, D Hunting, and L Sanche, "Cross section for low-energy (10-50 eV) electron damage to DNA", Radiat. Res. **157** (2002) 227–234.

[141] X Li, MD Sevilla, and L Sanche, "Density functional theory studies of electron interaction with DNA: can zero eV electrons induce strand breaks" J. Am. Chem. Soc. **125** (2003) 13668–13669.

[142] P Swiderek, "Fundamental processes in radiation damage of DNA", Angew. Chem. Ont. Ed. **45** (2006) 4056–4059.

[143] S Patasinski, S Denifl, P Scheier, E Illenberger, and TD Mark, "Decomposition of Thymidine by Low-Energy Electrons: Implications for the Molecular Mechanisms of Single-Strand Breaks in DNA", Angew. Chem. Int. Ed. **45** (2006) 1893–1896.

[144] S Ptasinska, S Denifl, P Scheier, E Illenberger, and T Mark, "Bond- and Site-selective loss of H atoms from nucleobase by very-low-energy electrons", Angew. Chem. Int. Ed. **44** (2005) 6941–6943.

[145] J Gu, Y Xie, and H Schaefer, "Near 0 eV electrons attach to nucleotides", J. Am. Chem. Soc. **128** (2006) 1250–1252

[146] I Dabkowska, J Rak, and M Gutowski, "DNA strand breaks induced by concerted interaction of H radicals and low-energy electrons" Eur. Phys. J. D **35** (2005) 429–435.

[147] Y Zheng, P Cloutier, D Hunting, L Sanche, and JR Wagner, "Chemical basis of DNA Sugar-Phosphate cleavage by low-energy electrons", J. Am. Chem. Soc. **127** (2005) 16592–16598.

[148] D Becker, A Bryant-Friedrich, C Trzasko, and MD Sevilla, "Electron spin resonance study of DNA irradiated with an argon-ion beam: Evidence for formation of sugar phosphate backbone radicals", Rad. Res. **160** (2003) 174–185.

[149] WA de Heer, C Berger, X Wu, PN First, EH Conrad, X Li, T Li, M Sprinkle, J Hass, ML Sadowski, M Potemski, G Martinez, "Epitaxial graphene", Preprint, Solid State Communications, submitted 2007.